Synthesis of Onion-like Carbon Using 3-Phase Plasma Reactor

by

Arash Davari Zanjani

B.Sc Mechanical Engineering, 2009, Takestan Islamic Azad University

A Thesis Submitted in Partial Fulfillment of

the Requirements for the Degree of

Master of Science

In the Graduate Academic Unit of Mechanical Engineering

Supervisor: L. P. Felipe Chibante, PhD, Chemical Engineering

Amirkianoosh Kiani, PhD, Mechanical Engineering

Examining Board: Andy Simoneau, PhD, Mechanical Engineering, Chair

Andrew Gerber, PhD, Mechanical Engineering

Muhammad Afzal, PhD, Mechanical Engineering

Guida Bendrich, PhD, Chemical Engineering

This thesis is accepted by the

Dean of Graduate Studies

The University of New Brunswick

August, 2017

Abstract

Since the discovery of fullerenes in 1985, synthesizing nano-materials such as fullerene, onion like carbon (OLC), nanotube etc. has been widely researched. One of the most used techniques in synthesizing nanocarbons is the high temperature plasma method. The plasma method, in this case a 3-phase arc plasma, provides efficiency, low environmental impact, scalability, and greater purity. While the 3-phase plasma method has been studied in fullerene and nanotube production, utilizing the 3-phase plasma in the synthesis of OLC has yet to be investigated.

The OLCs can be defined as giant molecules synthesized from carbon into the form of multilayered graphite. The OLC can be considered a hybrid nano-carbon with a structure between that of fullerene and graphene. The traditional methods of OLC production are batch based, expensive, and non-uniform, thereby limiting market use.

This research studies 3-phase plasma synthesis of OLC. A 3-phase plasma reactor was modelled, designed, constructed, and operated at conditions required for OLC formation. A previously developed quasi-2D model using convection-diffusion in finite volume was utilized to monitor the key parameters: gas flow rate, residence time, and power. After heat treating an amorphous carbon feedstock by the plasma, the products were characterized by 3 different characterization methods: thermal gravimetric analysis (TGA), transmission electron microscopy (TEM), and Raman spectroscopy. The results were then compared to the data gathered from the original feedstock and a reference OLC to determine conversion ratios. In addition, the energy efficiency of the plasma method was compared to conventional furnace annealing.

Table of contents

List of Figures

List of Tables

Nomenclature

Γ	Diffusion coefficient
$\dot{U}$	Gas flow rate (lit/min)
ρ	Density (kg/m^3)
ρ_p	Density of particles(kg/m^3)
ρ_f	Density of fluid (kg/m^3)
Φ	Common property (J/kg)
B	Magnetic field (Tesla)
C_p	Specific heat (J/kg K)
E	Electric field (N/C)
F_g	Gravitational force (N)
F_d	Drag force (N)
G	Gravitational constant (m/s^2)
h	Enthalpy (J/kg)
H	Convective heat transfer coefficient (W/m^2 K)
K	Thermal conductivity (W/m K)
M	Mass (kg)
P	Pressure (Pa)
P_e	Peclet number
Q	Electrical charge(C)
S_ϕ	Source term (W)
T	Temperature (K)
t	Residence time(s)
U	Velocity (m/s)
V	Volume (m^3)

List of Acronyms

AC	Alternating Current
DC	Direct Current
CVD	Chemical Vapor Deposition
MWCNT	Multi-Walled Carbon Nanotubes
MaCor	Machinable Ceramic
OLC	Onion-like Carbon
RPM	Revolution per Minute
RF	Radio Frequency
SS	Stainless Steel
SLM	Standard Liters per Minute
TEM	Transmission Electron Microscopy
TGA	Thermal Gravimetric Analysis

Chapter 1: Introduction

1.1 Onion Like carbon

Onion-like carbon is a nano material which falls into the family of fullerenes (C_{60}). Fullerenes were discovered by Curl, Kroto and Smalley in 1985 [1] by laser vaporization of graphite in low pressure [2, 3]; they are characterized as molecules synthesized entirely of carbon, in the form of a hollow sphere, ellipsoid, or tube. Spherical fullerenes are sometimes called Bucky balls; the C60 variant is often compared to a typical white and black soccer ball [4]. In 1992, onion-like carbon (OLC) was discovered by Ugarte. OLC consists of concentric multi-layered graphitic spheres as shown in Figure 1 [5, 6]. Ugarte first discovered OLCs by using intense electron beam irradiation [7]. In the formation of the OLCs van der Waals force plays a significant role. Consequently, the natural spacing between the circular layers in the OLCs is approximately 0.34nm similar as in graphite (see Figure 2) [8].

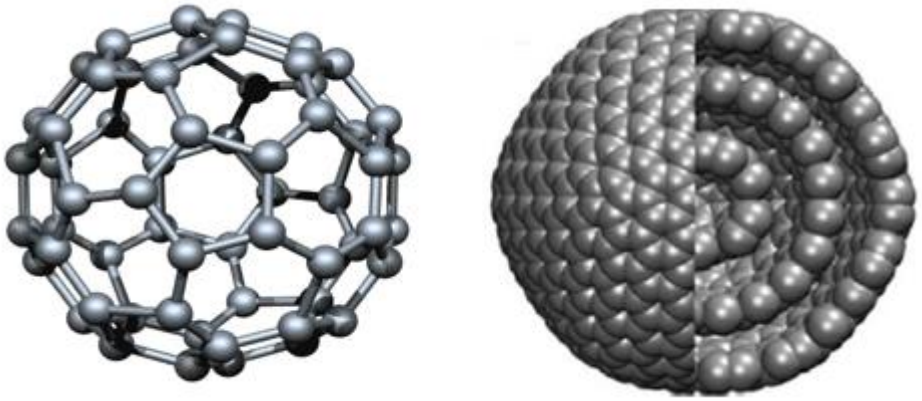

Figure 1.Fullerene (C60) structure (Left), Simplified multi shell fullerene model of a carbon onion used in MD simulation (right)[1] [2, 3, 6, 9]

Due to OLCs' unique structure, they are expected to have remarkable properties [5]. For example, OLC is known for its friction reducing and wear resistance characteristics which as a result one of OLCs' main applications is increasing the

[1] Figure Courtesy of Dr.Yury gogotsi, Drexel Nanomaterial Institute.

quality of lubricants. Hence, sometimes they are referred to as nano ball bearings. Furthermore, OLCs are chemically inert and made entirely of carbon which makes them friendly to the environment [10].OLCs' specific surface area is the reason for its application in making super capacitors [11]. Also, OLCs are employed in biology [7], fabrication of lithium batteries [10], and fuel cells [12].

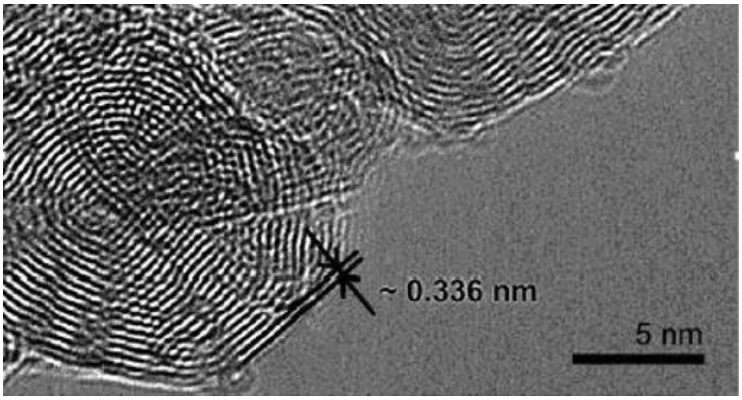

Figure 2. HRTEM images of ND 1800℃[2] [13]

There are several methods to synthesize OLCs, such as annealing, arc discharge in water, chemical vapor deposition (CVD) and radio-frequency microwave plasma [7, 14, 15]. All these methods are based on the transformation of the specific carbon structure, Carbon soot or nano diamonds, into onion like structure by means of heat treatment [7, 10]. The diameter of the fabricated OLCs is dependent on the method of the synthesis and it varies from 6nm to 50nm [16].

Ugarte first discovered OLCs by using intense electron beam irradiation. The diameter of the OLCs formed by this process was approximately 45nm [10, 14, 16]. Ugrate irradiated carbon soot with high energy beam under high resolution microscope. Since then, formation of OLCs by beam irradiation has been studied by utilizing different catalysts such as aluminum and platinum [17-19].

[2] Figure Courtesy of Dr.Yury gogotsi, Drexel Nanomaterial Institute.

One of the common methods of OLC formation is annealing of nano diamonds. In this method, bonds in nano diamonds are rearranged by extreme temperature into the OLCs. The diameter of the final product obtained by this process is 6 to 8nm. The annealing temperature varies from 1300 to 2400˚C. Higher annealing temperature will lead to OLCs without diamond core which is preferable considering OLCs' applications [7, 10, 16]. Figure 3 illustrates the OLCs synthesized by annealing of the nano diamonds with and without diamond core [10, 20].

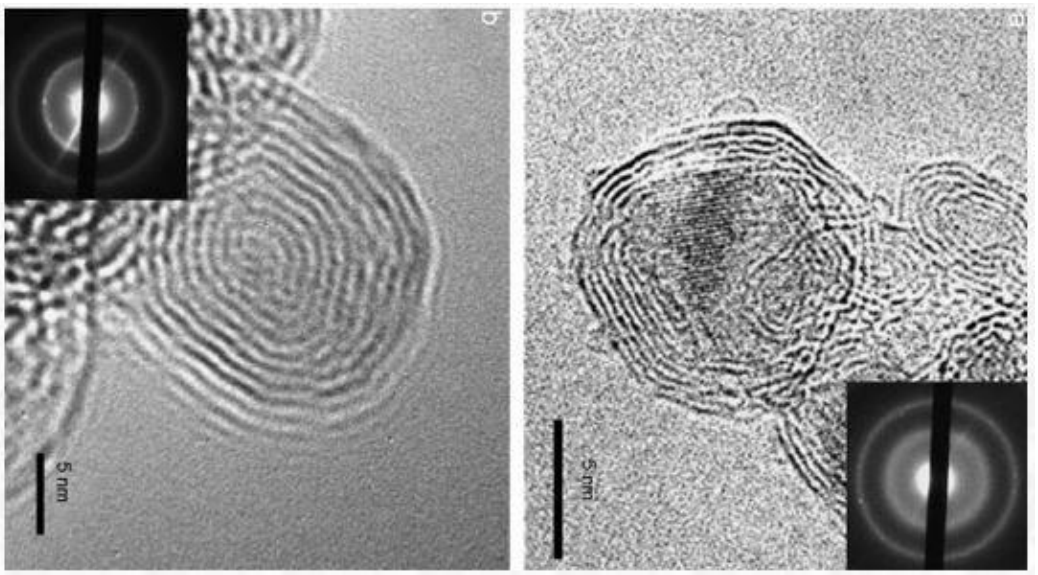

Figure 3.TEM image of the OLC formed by annealing of the nano diamond (Left) carbon onion completely graphitized (>2000°C). (Right) Carbon onion containing diamond core (1400-2000°C) [10]

Another method for preparation of OLCs is arc discharge in the water. Sano (2001) developed the arc discharge method by submerging the graphite electrodes in special media. In this apparatus OLCs were deposited on graphite cathodes. This process uses low current (30A) and fabricates OLCs in larger quantities. Diameters of the OLC created by arc discharge method varies from 5 to 36 nm [8, 21, 22].

1.2 Methods of OLC production

Since the main goal of this research is to provide a method to convert carbon black into the OLCs, conducting a review on the different methods of OLC production can be beneficial. Four major methods of OLC formation are CVD, intense beam

irradiation, high temperature annealing of nano diamonds, and arc discharge in water [23]. All these methods are based on addition of energy to a carbon source in order to decompose and rearrange the bonds which will lead to the formation of OLCs.

1.2.1 Electron beam irradiation

After Ugarte discovered OLCs by the electron beam irradiation this method has been reported as a successful in-situ technique. In 2004, Oku provided details of OLC synthesis by implementing electron beam irradiation on amorphous carbon obtained from polyvinyl alcohol. With Oku's technique, amorphous carbon is fabricated by annealing polyvinyl alcohol at 400℃ in Ar. Then, the amorphous carbon is irradiated by an electron beam for 30 min under a beam current of 100 A/cm^2 at 1250 kV [7, 24]. In this method, the spherical particles of graphitized carbon are in the range of 3-7 nm.

1.2.2 Chemical vapor deposition (CVD)

In the CVD method, OLCs are produced by using a catalyst (Ni/Al) at 600℃ and the OLCs diameter ranges from 5 to 50 nm including concentric carbon layers encompassing a hollow core or nickel particles. The catalyst is reduced to 600℃ in a hydrogen atmosphere for 2.5 hour which results in converting the nickel oxides to elementary nickel. Then, OLCs are grown at 600℃ for an hour while a mixture of CH_4/N_2 is introduced into the reactor at a specific flow rate. Although the final product have great quality in terms of conversion to OLC and eliminating defects, the CVD method requires purification and also does not yield OLC on a large scale [7, 25].

1.2.3 Arc discharge in water

The arc discharge method is a practical technique in synthesis of OLC in larger quantities. This economic and environmentally friendly method includes two submerged graphite electrode rods, one as anode and one as cathode. By producing a

discharge voltage (16-17 V) and current (30 A) between the electrodes a plasma is created. The power required for the plasma ranges between 825 and 1325 W and yields an average temperature of 4000-6500 K [7, 15, 26]. OLCs fabricated by this method have a diameter of 20 to 40 nm with interlayer spacing of approximately 0.34 nm. Also, there carbon nanotube and graphitic particles side products. This method can yield the OLCs in more scalable quantities than previous methods. However, the final product requires purification. Furthermore, in some setups using a catalyst, usually Ni, is necessary [23].

1.2.4 High temperature annealing of nano diamonds

In this method nano diamonds are used as the source material. Nano diamonds were first produced by Soviet military scientists by detonating explosives such RDX and TNT at high pressure and temperature [15, 27]. Annealing nano diamonds in high temperature (1600-2400 ℃) rearranges the bond and leads to the fabrication of the OLCs. The annealing temperature can be achieved by using a vacuum chamber. Joly-Pottuz (2006) dispersed the nano diamonds on an electrically heated graphite crucible under high vacuum (10^{-4} Pa) [26]. This technique could provide an annealing temperature of 1600 ℃. The purity of the OLC synthesized by this method is considerably high. The diameter of the final product obtained by this process is between 6 and 8nm. However, since the source material, in this case nano diamonds, is substantially expensive the production cost of the OLCs obtained by the annealing method is significantly high. Furthermore, this method procures the OLCs in small quantities. Table 1 illustrates the four major methods applied in OLC production, their operating conditions, and their disadvantages.

Table 1. Four major methods in OLCs production.

Methods	Operating Conditions	Source material	Disadvantages
CVD	600℃ 1h Catalyst 600℃ 2.5h	Amorphous carbon	Requires purification Low yield
Electron beam irradiation	100 A, 1250 kV	Amorphous carbon	Only for analysis
Arc discharge in water	17V, 30A 4000-6500 ℃	Amorphous carbon	Requires purification Medium yield catalyst(Ni)
Annealing nano diamonds	Vacuum chamber 1300-2400℃ for 15-30min	nano diamonds	Small quantities Expensive source material

To overcome the limitations of these methods, the 3-phase plasma method was proposed and researched in this study. Since OLCs are deemed to be giant fullerenes, and 3-phase plasma technique is already used in fullerene synthesis, it is conceivable of synthesizing OLC by the same plasma technique.

1.2 Statement of the problem

The referenced methods yield OLCs in small quantities. Also, the source material for the some of these methods can be considerably expensive. For example, 1 gram of nano diamond is around 250$. Additionally, utilizing catalyst and purification of the final product is another issue with some of these methods, such as arc discharge in water and CVD. However, a common requirement in synthesizing OLC is to expose a source carbon to a high temperature energy source.

Recently UNB Nano group has developed a 3-phase plasma reactor as high temperature source to synthesize fullerene. Since high temperature is the main requirement in OLC fabrication and considering the similarities between the structure of OLC and fullerene, this study proposes the method of 3-phase plasma as an

alternative method for OLCs production. While using the 3-phase plasma reactor is a common method in synthesizing fullerene, it has never been utilized in OLC production [28, 29].

This research intends to modify the 3-phase plasma method for OLC synthesis. Use of an amorphous carbon powder as source material in conjunction with the 3-phase plasma can turn the OLC synthesis into a continuous and commercially scalable process. Furthermore, carbon black powder is a cheap feedstock which considerably reduces the production cost. The next section concentrates on the literature in the field of 3-phase plasma and its application in fullerene and nano carbons production.

Chapter 2. Literature review on 3-phase plasma

2.1 Plasma technology

Plasma can be defined as gas ionization in the presence of an electromagnetic field [30]. In plasma, gas atoms, in most cases a neutral gas, are decomposed into negatively charged electrons and positively charged ions as a result of the high temperature. In the thermal plasma, these electrons and ions have the same temperature. Hence, the plasma is in thermal equilibrium [31]. Therefore, the high temperature provided by ionization process can be useful for heat treatment of different feedstocks.

In a plasma, the motion of the electrons and the ions is guided by the electric and the magnetic fields. The motion of the charged particles is calculated by using Lorentz equation [32]. Equation 1, illustrates the Lorentz equation of the motion:

$$\underbrace{m\frac{dv}{dt}}_{\text{Rate of change of momentum}} = \underbrace{q\,(E + V \wedge B)}_{\text{Lorentz Force}} \qquad (1)$$

In this equation q is the charge, E is the electric field, V is velocity, and B is the magnetic field. Plasma technology is being favored over traditional methods for the heat treatment of the feedstock such as combustion and partial oxidation. Some advantages of the plasma over traditional methods are as follows: the plasma can deliver a higher temperature by the means of an external energy source than combustion methods, it is friendly to the environment, and it is flexible and can operate in different atmospheres [33-35].

Plasma arc technology can be divided into DC and AC plasmas [33-35]. The DC plasma torches usually consist of a cylindrical tip (cathode) which is placed at the top of a nozzle (anode). A plasma plume is produced by injecting gas through the

chamber which is under electric power and the generated heat from the arc is dissipated through convection, diffusion, and radiation [31]. Temperature obtained by a DC plasma torch ranges from 10000-20000 K. One of the main issues of the DC plasma torch is the cost of constructing a power supply. In the most cases 30% of the cost of building a torch, especially for waste disposal, is allocated to construction of the power supply [36, 37]. Furthermore, erosion of the electrodes is another difficulty in DC plasma technology which can generate impurities in the final product and also increase the production cost.

The AC plasma torches were developed and researched to deal with these problems. In a multiphase AC plasma, several arcs can be produced simultaneously resulting in a considerably larger volume than with DC plasma [31, 34].

In a 3-phase plasma reactor electromagnetic force is generated by a power supply, usually a transformer. The arc is ignited by means of a high voltage ignitor. The arc moves between the 3 electrodes due to the phase difference. The motion of the arc is under the influence of the Lorentz force and each electrode plays the role of anode and cathode simultaneously [30, 38].

2.2 3-Phase plasma arc technology for nano-carbon production

In the 1960s and 1970s the arc discharge methods were first used for manufacturing carbon fibers. The main applications of carbon fibers were in space and aircraft industry due to their lightweight characteristic [34, 39]. Krätschmer (1990) reported synthesis of fullerene in a macroscopic scale by using electric arc discharge between two graphite electrodes under helium. In 1991 Iijima produced multi-walled carbon nano-tube by implementing the same technique in air [39-41].

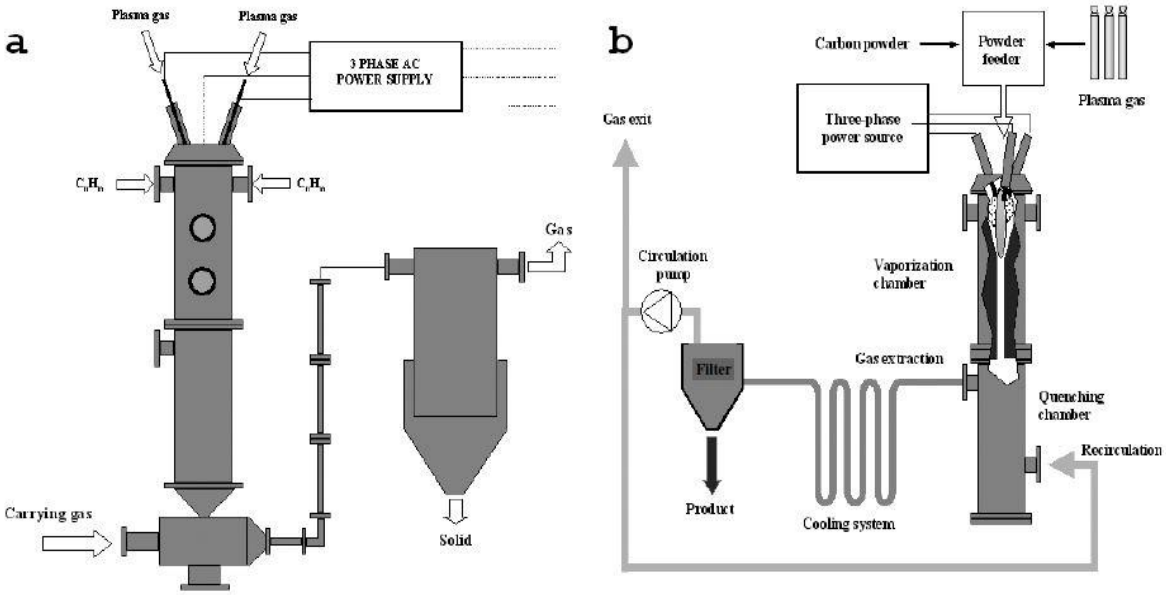

Figure 4. Flow sheet of the 3-phase ac plasma process for CB production (a) and for fullerene and nanotubes production (b)[3] [2]

Application of 3-phase plasma in nano carbon synthesis was primarily proposed by Schwob (1994) [42], and it was Schwob who also used 3-phase arc plasma in carbon black (CB) production [42, 43]. In 1998, Ravary and his team utilized a 3-phase plasma reactor for hydrocarbon cracking in order to manufacture carbon black and hydrogen [32].Fulcheri (1999) used a 100 kW 3-phase AC source with consumable graphite to produce fullerenes [2]. The electrodes were located at the top of the reactor and the process allowed the production of soot with a high yield in the high temperature zone of the reactor [28, 44]. Figure 4 shows the flow sheet of the 3-phase plasma reactor for carbon black, fullerene, and nanotubes production.

Fulcheri (1999) performed all the tests at atmospheric pressure; in his experiments the gas flow rate varied between 30 and 80 N l/min[4] and he used ten different carbon powders as source material [44]. Fincke (2002) applied a DC plasma torch for the thermal plasma pyrolysis of methane into CB and hydrogen by introducing

[3] Figure Courtesy of Dr. Jose Gonzalez-Aguilar, IMDEA Energy Institute.
[4] Normal Liter per min

a specially designed reactor [45, 46]. Wang (2001) fixed the input power of the 3-phase plasma to 30 kW and used the mixture of argon, helium, CO_2 with carbon powder of 20 µm in 10 kPa pressure. According to his work, 20 µm particles yielded better results in fullerene production than 1 µm particles. Wang (2003) enhanced fullerene purity by adding silicon as an additive to the feedstock in order to prevent formation of CO and CO_2. However, Wang did not report any improvement in fullerene yield [2, 47, 48].

Gruenberger (2006) implemented 3-phase plasma to produce fullerene and other nano material utilizing a 260 kW power supply [44]. Rutberg (2007) introduced a 3-phase plasma torch with a power range between 6 kW and 600 kW. This plasma was optimized to work on oxidizing media (gas flow rate from 0.5 up to 70 g/s) [30, 38]. The main applications of the Rutberg plasma torch were waste disposal and renewable energy. Fulcheri (2012) did a study on fullerene production via phase plasma using a 40 kW power supply. He used three distinct carbon powders as the precursor, and mainly concentrated on gas flow, and carbon feed rate. Fulcheri (2012) stated that carbon concentration in the reactor has a significant effect on carbon graphitization

Chapter 3

3.1 Research scope and objectives

While graphite is a crystalline allotrope of carbon and fullerene is hollow spherical allotrope of carbon, OLCs can be characterized as a carbon nano material with a structure between that of graphite and the fullerene [4, 44, 50]. Since different studies on the characterization methods of OLCs, such as thermogravimetric analysis, Raman spectroscopy, and transmission electron microscopy, show specific data allocated to the OLCs structure, as shown in Figure 2, this amazing nano material can be considered as round graphite.

Because of OLCs' unique shape, it presents remarkable physical and electron accepting properties. Furthermore, OLCs have a wide range of applications in supercapacitors, lubricants, fuel cells, lithium batteries, and biology. As a result, the market for OLCs is growing remarkably. The current methods for OLC production require significant amounts of energy and they are batch process in nature. A continuous production method that can fabricate OLCs in larger scale seems desirable. As Table 1 depicts most of the current methods of production yield OLCs in low scale. Also, some of these techniques require purification of the final product. Hence, in this study method of 3-phase plasma was proposed as an alternative technique for OLC fabrication.

3-Phase plasma has been extensively used as a method to produce fullerene. The basic concept in the fullerene synthesis is to vaporize carbon by adding energy, quench the vaporized carbon, and extract the fullerene by means of a solution [44, 51]. The energy for carbon evaporation can be provided by combustion [52], laser [53], solar [45], and plasma. Since the plasma method, especially AC plasma, is a local

environmentally friendly and continuous method that may provide good production rate and efficiency

While a required step in fullerene production is the evaporation of the feedstock, OLC synthesis only requires heat treatment of the source material [7, 15, 52]. Therefore, the needed power for the plasma process in OLC production is substantially lower than that required for fullerene requirement. Furthermore, due to its thermal conductivity and atomic weight the ideal plasma gas used in the fullerene production is helium which provides higher plasma temperature. However, with the lower OLC power requirement argon can be used as plasma gas. Utilizing argon as the plasma gas is beneficial since it is cheaper than helium and also allows less electrode erosion. All these factors contribute to a lower the production cost. The main objective of the project is to provide a proof of concept using 3-phase plasma to synthesize OLCs.

The goal of the study is to use the heat provided by the 3-phase plasma for the conversion of the amorphous carbon to OLC. The parameters of interest in this process are plasma temperature and residence time of feedstock in the reactor. Therefore, considering the variables of interest, the following questions will arise:

How much energy (heat) and time are required for the conversion of the feedstock to OLCs?

It is expected that providing enough heat with a sufficient residence time can render an ideal condition for the conversion of the amorphous carbon to OLC based on other methods. Typically, these other methods operate at lower temperatures and require minutes to hours of heat exposure. However, with much higher temperatures of the current plasma reactor it is predicted that the exposure time would be drastically lower (less than a second).

How can residence time be controlled in the reactor?

The main parameter affecting the residence time is the gas flow rate. Also, it is presumed that the geometry of the reactor may play significant role on controlling the exposure time as well as uniformity of product.

How does the carbon feed rate impact the conversion of the feedstock to OLC?

It is predicted that the lower carbon concentration could improve the conversion of the carbon powder to OLC to some extent. Since the feedstock is carried by the plasma gas, increasing the carbon concentration may require higher gas flow in order to carry the source material through the system which in return will have a negative impact on the residence time.

3.1.2 Significance of study

Methods of OLC production are batch processes and yield OLC on small scale. A study on the 3-phase plasma to fabricate the onion like carbon structure can provide viable information to find a continuous and scalable method which can satisfy the market for OLC. The current methods of OLC production require either expensive equipment or costly feedstock. However, the plasma method can provide an inexpensive technique for the conversion of the feedstock to the desired nano carbon. Also, this study tends to realize the required time and energy for the conversion of a cheap source material into OLC. The main goals of the project are as follows: shorten the process time compared to the common OLC synthesis methods, introduce a continuous, scalable, and efficient technique for the formation of OLC, and reduce the production costs.

Building multiple reactors to study the sensitive parameters in the carbon conversion requires a significant amount of resources and time. Furthermore,

calculating the variables of the interest in a plasma is a complicated process. Therefore, to monitor the variables of interest, a quasi-2D model is also presented. The quasi-2D model can be used as a tool in identifying the trends when a variable is modified. Since a specific energy and exposure time is required for the conversion of the carbon to OLC, the quasi-2D model can grant better observation on the required range of the key variable.

3.1.3 Delimitations

This study focuses on the parameters affecting OLC synthesis by described plasma method. The research mostly concentrates on identifying the effect of the variables of interest on the conversion of the carbon into the desired nano structure. The study will not attempt to find the optimal production rate and optimize the variables of interest. Furthermore, the research was limited to a narrow range of exposure times. Another limitation was variation of the geometry of the reactor since the assembly and possibility of constructing parts had to be taken into consideration. The study only focused on one type of carbon black (N234), which has a low degree of graphitization [43, 46]. Other carbon feedstocks were not explored in this study. Though variations in the conversion and the quality of the nano structure was characterized by different methods, the energy of the plasma was limited to a specific range.

3.1.4 Assumptions

1. It is assumed that the plasma torch works in a steady state and the temperature profile does not change with time or by introducing any feedstock.

2. Heat convection does not have any effect on injecting material through the plasma discharge.

3. The only materials passing through the plasma zone are argon gas and the feedstock.

4. Minimum temperature required for the conversion of the OLC is 4000℃.

5. All the feedstock is equally exposed to plasma and the exposure only occurs once and exits to the collection chamber.

3.2. Background of the 3-phase plasma reactor developed by Applied Nano Lab

3.2.1 3-phase plasma reactor 1st generation (GenI)

A 3-phase plasma reactor was designed, inspired by Fulcher's reactor [6, 32] (Figure 4b), in order to produce fullerene and other nano materials. The main difference between the GenI reactor and the Fulcher's reactor was the ability to control the carbon powder injection without being limited by electrode's erosion. The GenI design was tested with two electrode setups, divergent and convergent. The different torch setups are shown in Figure 5.

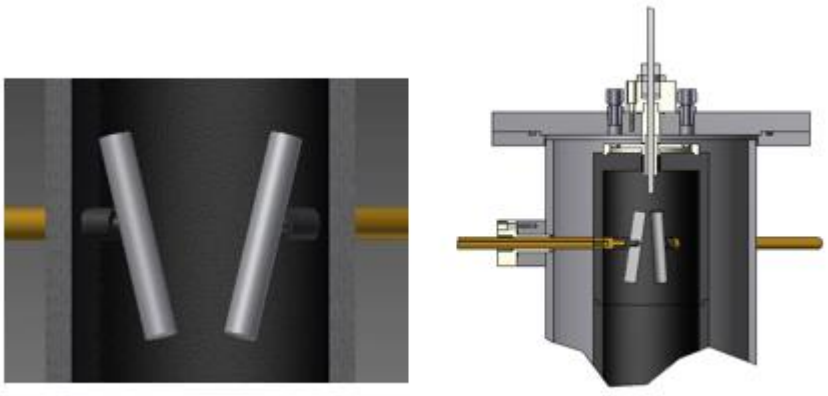

Figure 5. Convergent set up of the electrodes (left), Divergent set up of the electrodes (right).

In the GenI reactor, 3 water cooled brass electrodes were installed in a graphite chamber. These electrodes were positioned 120 degrees away from each other. Also, they either diverged or converged 15 degrees towards the central axis of the reactor

chamber [29]. The GenI reactor column could be separated into 4 zones: Plasma hot zone, reaction zone, neck or quenching zone, and collector. The four separate zones of the reactor are illustrated in Figure 6.

In a GenI reactor, carbon powder is injected from the top into the plasma hot zone via carrier gas and nano powder feeder. Meanwhile, a sheath gas is responsible for stabilizing the plasma. Carbon powder is pushed into the plasma hot zone (A) by a carrier gas. Carbon powder falls into the reactor chamber under the influence of gravity and gas flow which highly affect the exposure of the powder to the plasma. The heat treatment zone (B) objective is to maintain the required energy (enthalpy) for conversion of the powder into the desired product.

The quenching zone (C) creates a cold zone for the purpose of quenching the powder. Finally, the powder is collected from the collector (D).

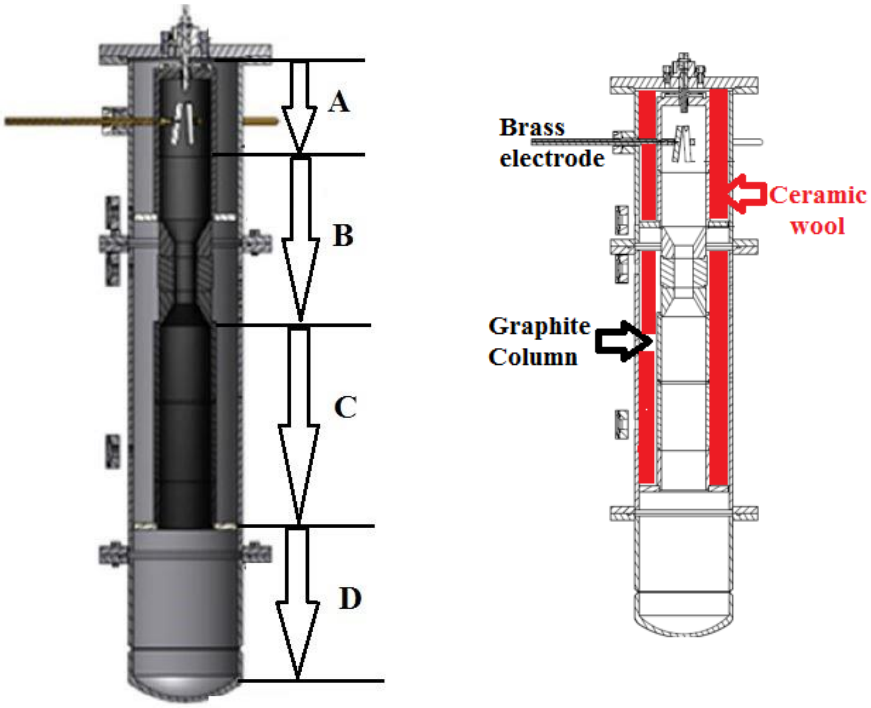

Figure 6. GenI reactor zone separation, A. plasma hot zone B. heat treatment zone, C. Quench zone or neck, D. Collection zone.

The GenI design is advantageous in several respects:

-continuous process
-self-stabilizing plasma
-carbon feed is not limited by electrode erosion
-minimum waste
-low maintenance
-scalable

To achieve better comprehension over the design approach taken by the Nano Team, an initial process flow diagram of the GenI reactor is depicted in Figure 7. As Figure 7 illustrates, the carbon powder is carried by an inert gas from the powder feeder to the reactor and consequently through the plasma (lines 1, 3, and 5 in figure 7). A sheath gas stabilizes the plasma via line 5. The carrier gas and the sheath gas are controlled by gas flowmeters. The collection of the heat treated feedstock takes place at the bottom of the reactor chamber. Also, the condition of the plasma is visually monitored through the viewports which were installed in the top chamber of the reactor.

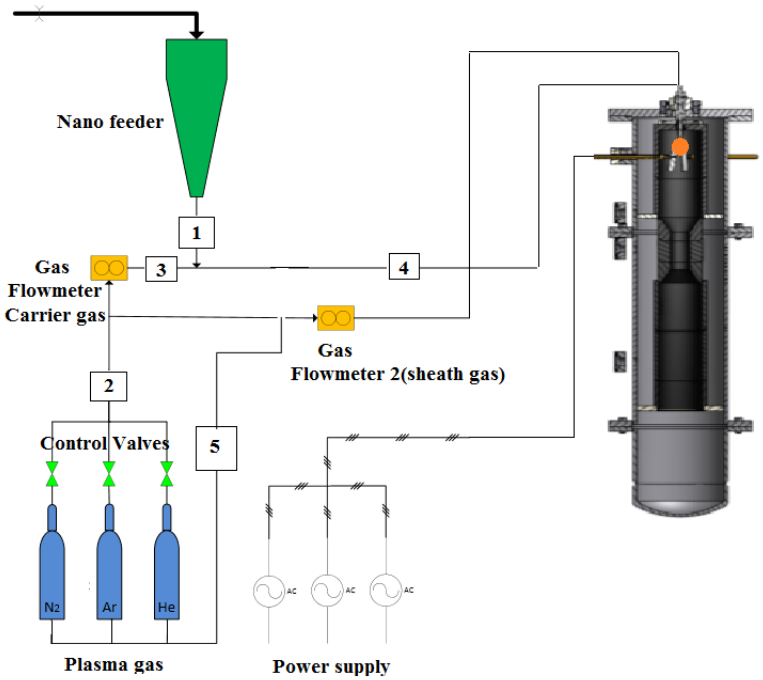

Figure 7. The initial flow diagram of the 3-phase plasma reactor.

However, a fullerene yield <0.25% in the final product was produced. Furthermore, a small portion of the samples exhibited the conversion of carbon powder into onion-like carbon. Table 2 shows the range of the parameters used in the GenI reactor. Figure 8 shows the TEM image of the end product fabricated by the GenI reactor. Comparing Figures 8 (a) and (b) reveals the presence of the multilayered graphite.

Since the result indicated minimal conversion of the feedstock to OLCs' structure, it was concluded that the exposure time to the heat provided needed to be increased. The parameters that could affect the exposure time were considered to be gas flow rate, feedstock concentration, and reactor design.

Table 2.Characteristics of the GenI plasma.

Carbon feedstock	Gas flow rate	Gas type	Plasma power	Pressure
Carbon Black N234	5-20 SLM	Helium	3 kW	1 atm

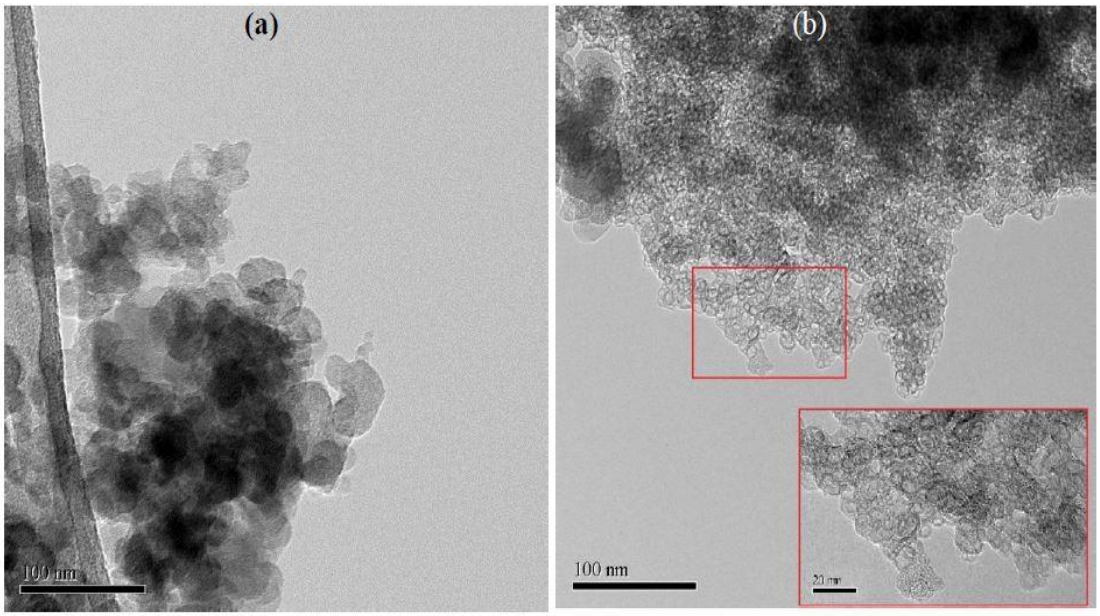

Figure 8. TEM image of Carbon before (a) and after (b) exposure to the plasma [54].

The duration of the exposure of the carbon powder to the plasma (heat source) when the volume is constant can be defined as residence time. Primarily, the residence time plays a significant role in the conversion of the carbon powder into nano materials. The general formula for residence time is shown in equation 2.

$$t = \frac{V}{\mathrm{U}} \quad (min) \tag{2}$$

In equation 1, U is the gas flow rate (lit/min) and V is the volume of the system. Also, in the GenI reactor, the volume of the chamber was relatively larger than the plasma volume which had negative influence on the plasma enthalpy. To overcome the issues regarding the residence time and the plasma volume a new approach was proposed by the group. The new design had to be flexible so it could be utilized for fullerene synthesis and also by applying some adjustments could be used for OLC production.

Due to the limited resources, an on-going quasi-2D model [55] using convection diffusion for finite volume method was used as a tool to monitor the important parameters of the plasma. This quasi-2D model revealed viable information pertinent to the behavior of the important parameters such as the gas flow rate, temperature, and the effect of the reactor's geometry on plasma volume. Furthermore, in the design of the experiment the required range of the key variables was determined by the data acquired by the quasi-2D model. In the next section the design approach for the GenII reactor and quasi-2D model are explained. Also, related data obtained from the model is presented.

3.3 2nd Generation Plasma Reactor (GenII)

The GenII 3-phase plasma reactor was a combination of the Fulcheri reactor and a 1981 patent [56] for a DC plasma reactor. In 1981, Markel proposed a DC plasma reactor for heat treatment of carbonaceous material with aid of fluidized bed. Figure 9 displays the proposed patent in 1981. In Markel's patent the carbon injection took place at the top of the reactor. Furthermore, the design was based on utilizing buoyant force to improve the exposure time.

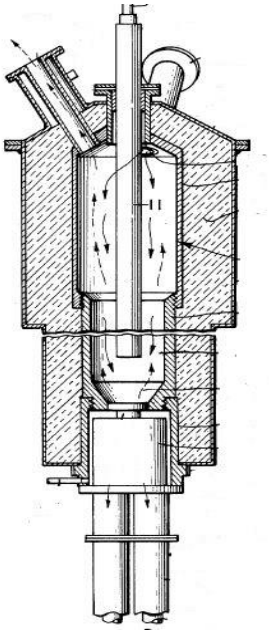

Figure 9. Schematic of DC reactor in combination with fluidized bed (US patent)[56].

Although in a GenII reactor the same concept was taken into consideration, the injection of carbon takes place at the bottom of the reactor. Also, the carbon feedstock is injected in the form of aerosol with aid of carbon powder feeder and carrier gas flow.

Figure 10, illustrates the GenII design. As Figure 10 displays, the electrodes are located at the bottom of the reactor. Furthermore, since buoyant force drove the aerosol through the reactor, the column of the reactor experienced gradual increase in diameter to generate a pressure difference.

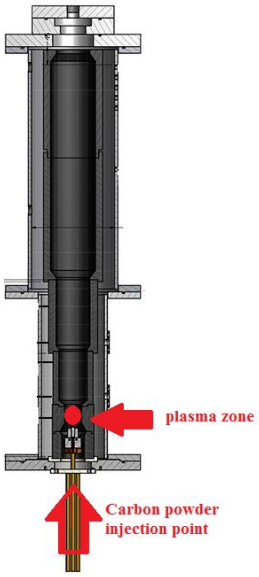

Figure 10. The 3-phase plasma reactor second generation (GenII).

Positioning the injection of the feedstock at the bottom of the reactor and the gradual increase in the chamber diameter provide the reactor with a fluidized bed. The fluidized bed is a technique which is known as assistive in the scaling of the nanoparticles synthesis [57]. As van Ommen (2012) states, the fluidized bed has been widely used in nanotechnology as a method to scale up the production of nanoparticles [57,58]. Van Ommen (2012) defines fluidization as, the suspension of the particles in an upward gas stream with such a velocity that drag and gravity are in equilibrium. The related formulae for calculation of the buoyant force are as follows [59]:

$$F_g = (\rho_{p-} \rho_f) g V_p \quad (3)[60]$$

$$F_d = \nabla p A H \quad (4)[60]$$

In equation (3), F_g is the gravitational force in a fluidized bed, ρ_p is the density of the particles, ρ_f is the density of the fluid, and Vp is the total volume of particles. Equation 4 illustrates the drag force. In equation 31, ∇p is the pressure drop, A is the cross-sectional area, and H is the height of the bed.

3.4. Quasi-2D model 3-phase plasma reactor Gen-II

To investigate the key parameters in the 3-phase plasma and monitor the range of these variables a quasi-2D model was used. The quasi-2D model was built according to the convection-diffusion method for finite volume via MATLAB by Dr. Kevin Wilcox at UNB Fluid Dynamics group [55]. Moreover, the quasi-2D model was used as a tool to provide meaningful relation between critical parameters of the plasma and their effect on temperature of the plasma and residence time of the gas.

This section elaborates on the construction of the model, illustrates the finite volume method for convection-diffusion, and presents the data obtained by alternating the key variables in the model, such as geometry, power, and gas flow rate.

3.4.1 Finite volume method for convection-diffusion

In the 3-phase plasma reactor, fluid flow, in this case argon gas flow, plays a significant role in temperature distribution. Therefore, the effect of convection should be accounted for. Furthermore, in nature diffusion takes place in company with convection [61], so in order to anticipate the combination of convection-diffusion the transport equation should be taken into account. Additionally, in order to calculate the velocity and temperature fields two sets of equations are needed [62]:

$$\frac{\partial(\rho\phi)}{\partial t} + div(\rho\phi u) = div(\Gamma\ grad\ \phi) + S_\phi \tag{5}$$

Storage convection diffusion source

$$\frac{\partial\rho}{\partial t} + div(\rho u) = 0 \tag{6}$$

Equation 5 is known as the transport equation, the rate of the change and the convective terms are on the left side and the diffusive (Γ= diffusion coefficient) and the source terms are on the right side. The rule of the transport equation states: enthalpy leaving a control volume and entering the adjacent control volume should be equal. Furthermore, equation 6 is the conventional form of continuity law in fluid dynamics.

In Equations 5 and 6 the parameters are as follows:

ρ: Fluid density

u: Velocity field

Γ: Diffusion coefficient

S_ϕ: Source term

By integrating over the control volume the following equation is obtained [61]:

$$\int_V n.(\rho\phi u)dA = \int_V n.(\Gamma\ grad\ \phi)dA + \int_{CV} S_\phi dV \tag{7}$$

Equation 7 shows the balance in control volume. The left hand side represents the net convective flux across *dA* and the right hand side includes the net diffusive flux [61, 63] across the same *dA*. In each control volume, the common property is developed and eliminated. The diffusion process affects the distribution of a transported quantity along its gradients in all directions, whereas flow direction is guided by convection

dispersion. Equation 8 governs the one-dimensional fluid field of the common convection diffusion property ϕ when there is no source term.

$$\frac{\partial(\rho\phi)}{\partial t}+\frac{d}{\partial x}(\rho\phi u)=\frac{d}{\partial x}\left(\Gamma\frac{d\phi}{\partial x}\right) \tag{8}$$

The flow must satisfy continuity so:

$$\frac{d(\rho u)}{\partial x}=0 \tag{9}$$

One dimensional control volume is shown in Figure 11. In Figure 11, node P is the main node. There are also adjacent nodes on the right and the left side of the node P. The node on the left is represented by W (west) and the node on the right by E (east). For each control volume the boundaries are positioned halfway through the adjacent nodes, w and e [61, 64].

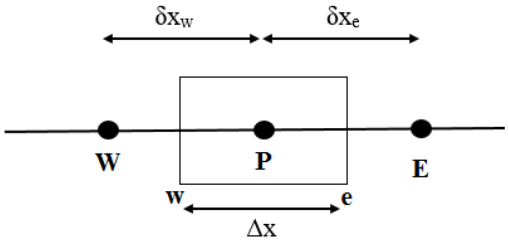

Figure 11. Node p and neighboring nodes in one-dimensional steady convection-diffusion

By integrating equation 8 considering control volume, Equation 10 is produced.

$$(\rho\phi uA)e-(\rho\phi uA)w=\left(\Gamma A\frac{d\phi}{\partial x}\right)e-\left(\Gamma A\frac{d\phi}{\partial x}\right)w \tag{10}$$

Also integration of continuity provides Equation 11.

$$(\rho uA)e-(\rho uA)w=0 \tag{11}$$

In order to obtain a discretized equation it is helpful to define two variables, F and D, to represent the convective mass flux per unit area and diffusion conductance at cell faces respectively.

$$F = \rho u A \tag{12}$$

$$D = \frac{\Gamma A}{\partial x} \tag{13}$$

The integrated convection-diffusion equation is as follows:

$$F_e \phi_e - F_w \phi_w = D_e (\phi_e - \phi_p) - D_w (\phi_p - \phi_w) \tag{14}$$

With the integrated continuity equation as:

$$F_e - F_w = 0 \tag{15}$$

There are various schemes for modeling convection-diffusion between cell volumes. The diffusion term is always discretized by a central scheme. While the original code was implementing the upwind differencing scheme for discretization, the code was modified to work according to hybrid differencing scheme. The hybrid differencing scheme [65] works as a combination of central [61, 62] and upwind differencing schemes [64] .These schemes will be explained briefly in the following sections.

3.4.2 Central differencing scheme

The central differencing scheme implements linear interpolation to compute cell face values for the convective term on the left side of the equation. Cell face values for property ϕ can be written as [61]:

$$\phi_e = (\phi_P + \phi_E)/2 \tag{16}$$

$$\phi_w = (\phi_W + \phi_P)/2 \tag{17}$$

Substituting equations 16 and 17 into equation 14 yields:

$$\frac{Fe}{2}(\phi_P + \phi_E) - \frac{Fw}{2}(\phi_W + \phi_P) = D_e(\phi_E - \phi_P) - D_w(\phi_P - \phi_W) \quad (18)$$

By identifying the coefficients of ϕ_w and ϕ_e as, a_w and a_e, respectively, the central differencing expression for the convection-diffusion on a cell can be shown as:

$$a_p \phi_p = a_w \phi_w + a_E \phi_E \quad (19)$$

Table 3. The internal coefficient of discretized scalar transport equation

a_W	a_E	a_P
$D_w + \frac{Fw}{2}$	$De - \frac{Fe}{2}$	$a_w + a_e + (F_e - F_w)$

In the central differencing scheme to conserve the general property (enthalpy) for the solution, the flux of the property ϕ that parts the control volume must be the same as the flux introducing the neighbor control volume through the same face [62].

3.4.3 Upwind difference scheme

One of the main issues with the central difference scheme is its weakness in identifying the flow direction. In central differencing the property ϕ at the west node is always influenced by the ϕ_p and ϕ_w. If the flow is strongly convective from west to east, this approach will not be suitable because the west cell face should receive stronger influence from node w than from node p. To solve this issue the upwind difference scheme is established. In a sense, in the upwind scheme the cell boundary value is equal to the upstream value. Although the upwind scheme provides first order accuracy, this method will take the flow direction into account [64, 66].

When the flow is positive (west to east) the upwind scheme is as follows:

$$\phi_w = \phi_W \quad \text{and} \quad \phi_e = \phi_P \tag{20}$$

See Figure 14.

$$F_e \phi_p - F_w \phi_W = D_e (\phi_E - \phi_P) - D_W (\phi_P - \phi_W) \tag{21}$$

Equation 21 can be rearranged as

$$(Dw + De + Fe)\, \phi\, p = (Dw + Fw)\, \phi\, W + De\, \phi\, e \tag{22}$$

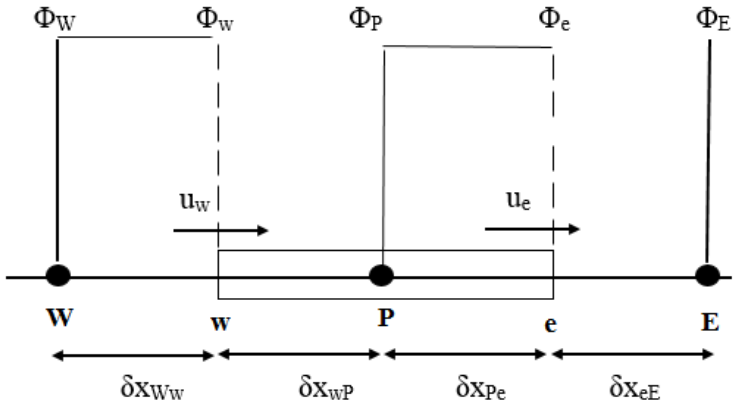

Figure 12.Nodal values used to calculate cell face values when the flow is in the positive direction[67].

By determining the coefficients of ϕ_W and ϕ_E as, a_w and a_e, respectively, the upwind differencing expression for the convection-diffusion on a cell can be shown as:

$$a_p \phi_p = a_w \phi_w + a_e \phi_e \tag{23}$$

The central coefficient can be written as:

$$a_p = a_w + a_e + (F_e - F_W) \tag{24}$$

Table 4 illustrates neighbor coefficients of the upwind differencing method that includes both flow directions. Figure 12 shows the discretization of the control volume in the upwind scheme.

Table 4. Neighbor coefficients of upwind differencing method for both directions

a_W	a_E
$D_w + \max(F_w, 0)$	$D_e + \max(0, -F_e)$

3.4.4 Hybrid differencing scheme

The hybrid differencing scheme was first introduced by Spalding (1972). This method is based on both the central difference and upwind schemes. In a convection-diffusion model, in order to determine whether the central or upwind differencing schemes should be used Peclet numbers should be taken into consideration. The Peclet number measures the relative strength between convection and diffusion. The formula for Peclet numbers is shown in Equation 25 [65, 67].

$$P_e = \frac{F}{D} = \frac{\rho u}{\Gamma/\delta x} \tag{25}$$

δx= Characteristic length

In the case of no convection and pure diffusion the Peclet number is equal to zero. In contrast, in the case of no diffusion and pure convection this number tends toward an infinite value. The central differencing scheme, which is accurate to second order, is employed when Pe < 2. The upwind differencing scheme, which is accurate to first order but accounts for transportiveness, is used when Pe ≥ 2. In the hybrid differencing scheme a local Peclet number is implemented to evaluate the net flux through each control volume [68].

Table 5. Neighbor coefficients of hybrid differencing method.

a_W	a_E
$\max[F_w, (D_w + \frac{Fw}{2}), 0]$	$\max[-F_e, (D_e - \frac{Fe}{2}), 0]$

3.4.5 Description of the MATLAB code

The 3-phase plasma reactor is modelled based on the convection-diffusion method using finite volume. The goal of the modelling is to provide insight on the effect of key variables such as reactor geometry, gas flow rate, and power. Therefore, these parameters are defined as the input variables in the code.

The general property ϕ, in this case enthalpy, was calculated by employing a hybrid convection scheme in each characteristic length. In order to avoid complication in modeling, the plasma was considered a volumetric heat source. This heat flux was considered to be in the small region beyond the gas injection point. The exact position of the heat source in the reactor length was set to be the segment between 0.10 to 0.15m from the gas injection point.

Physical properties of the argon including specific heat, thermal conductivity, density, and enthalpy were tabulated according to temperature. The table of properties was originally generated for helium [55]. Since the experiments were conducted in argon, the properties of argon was gathered from various references up to 24000 K [69-71]. The table of properties for argon is presented in Appendix 1.

To calculate the heat transfer between the walls and the heat source, the thermal resistance of the reactor wall was taken into consideration. In this case four components were regarded for thermal resistance:

1) Graphite, which is the material used to build the chamber.
2) Steel (outer wall).
3) Refractory (distance between graphite and steel wall).
4) Free convection.

Equation 26 was used to calculated thermal resistance of graphite, steel, and refractory. Also, Equation 27 was used for determining the free convection.

$$R = \frac{Ln^{r_o}/_{r_i}}{2k\pi dx} \tag{26}$$

Where r_o is the outer radius of the resistance and ri is the inner radius of the resistance and k is the thermal conductivity of the resistance.

$$R_f = \frac{1}{2\pi h_{air} r_{steel} dx} \tag{27}$$

Where h_{air} is the heat transfer coefficient of air and r_{steel} is radius of steel shell. Figure 13a illustrates the image of the reactor chamber and Figure 13b shows the same configuration translated the model where half the reactor is represented symmetrically along the reactor centerline. The thickness of each layer in Figure 13a is used to calculate the heat transfer between wall and the heat source.

In the quasi-2D model, the length of the reactor (0.55 m) is discretized to 195 cells. The initial temperature of all the nodes is set to 293 K. According to Table 5, each node is linked to the west and the east node therefore by introducing the boundary condition for the first (inlet) and the last node (symmetry) a tridiagonal matrix is generated.

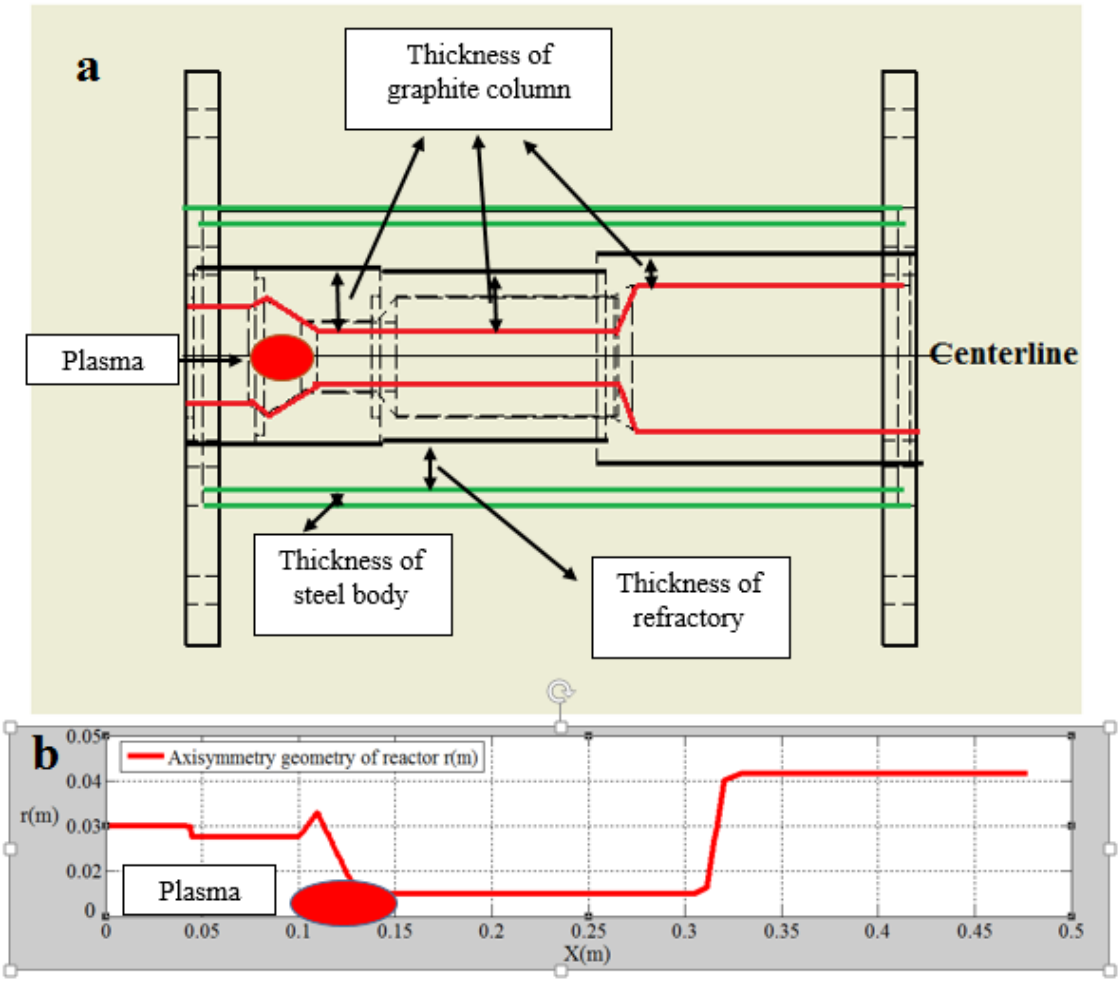

Figure 13. Plasma reactor body (a) the boundary generated by the model (b)

Finally, the Thomas algorithm was utilized to solve the unknown enthalpy for each control volume at each time step. The process is repeated to the point of conversion (steady state). The flow chart of the code is presented in Figure 14.

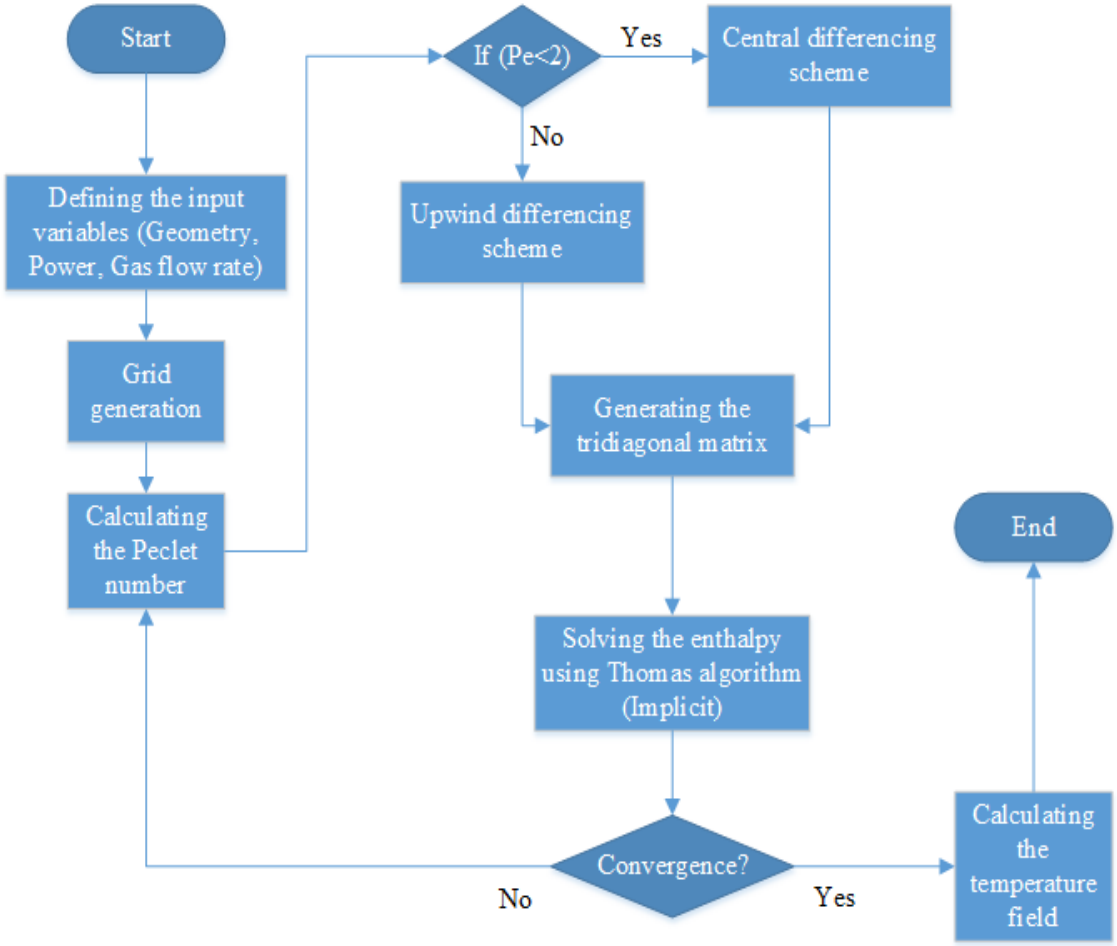

Figure 14. Flow chart of the model.

3.4.6 Analysis of the important parameters in the design of the reactor via the quasi-2D model

The main objective of the quasi-2D model was to be a tool to identify variables of interest. Also, utilizing the model can save resources in production and it can be beneficial in realizing the effect of different variables such as geometry, gas flow rate, and power on the temperature profile and residence time.

Since the geometry of the OLC reactor has an important influence on the velocity of the gas and consequently the residence time of the material inside the

reactor, the model was used to monitor the effect of geometry on the velocity of the gas. In terms of the position of the heat source, the OLC reactor was divided into 2 sections pre-heat source and post-heat source.

The radius in section 1 (before the heat source) varies from 21.5mm to 35mm. By decreasing the radius the velocity of the gas slightly increases. However, since the heat source is positioned after section 1, the gas flow does not change substantially (see Figure 15). Figure 15 displays the change in the geometry in section 2 (post heat source) and its effect on gas velocity.

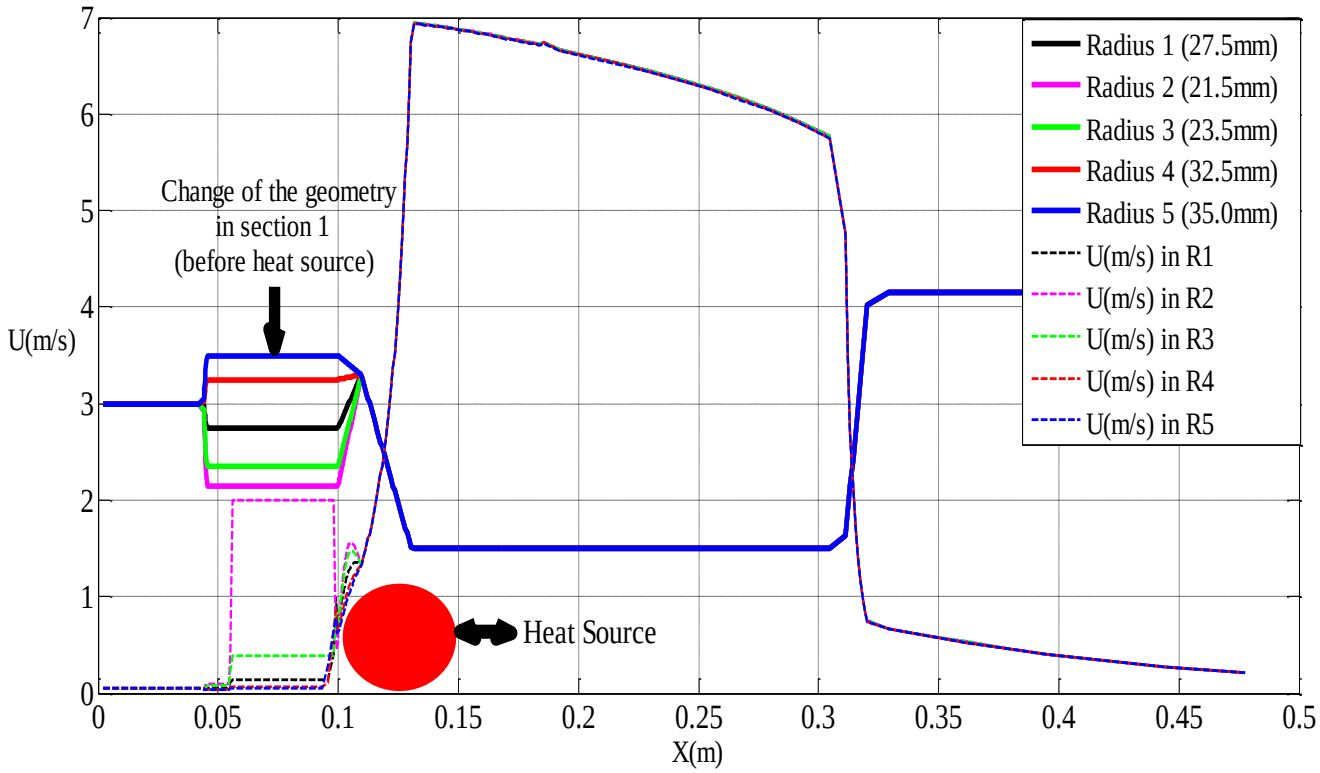

Figure 15. Change in the gas velocity when the radius of the OLC reactor is modified in section 1(before the heat source). W=5kW, P=1atm, Q=8 L/min.

In Figure 16, enlarging the radius can give longer residence time but the volume of the plasma has to be taken into consideration. The radius 1 (15.0 mm) was the boundary condition in the construction of the reactor. The larger radius could provide lower residence time however plasma and the process of the gas ionization act much differently than a heat source. The plasma volume and enthalpy maintenance is of high importance since in the Gen I reactor the large chamber nullified the effect of residence time due to small relative volume of the plasma.

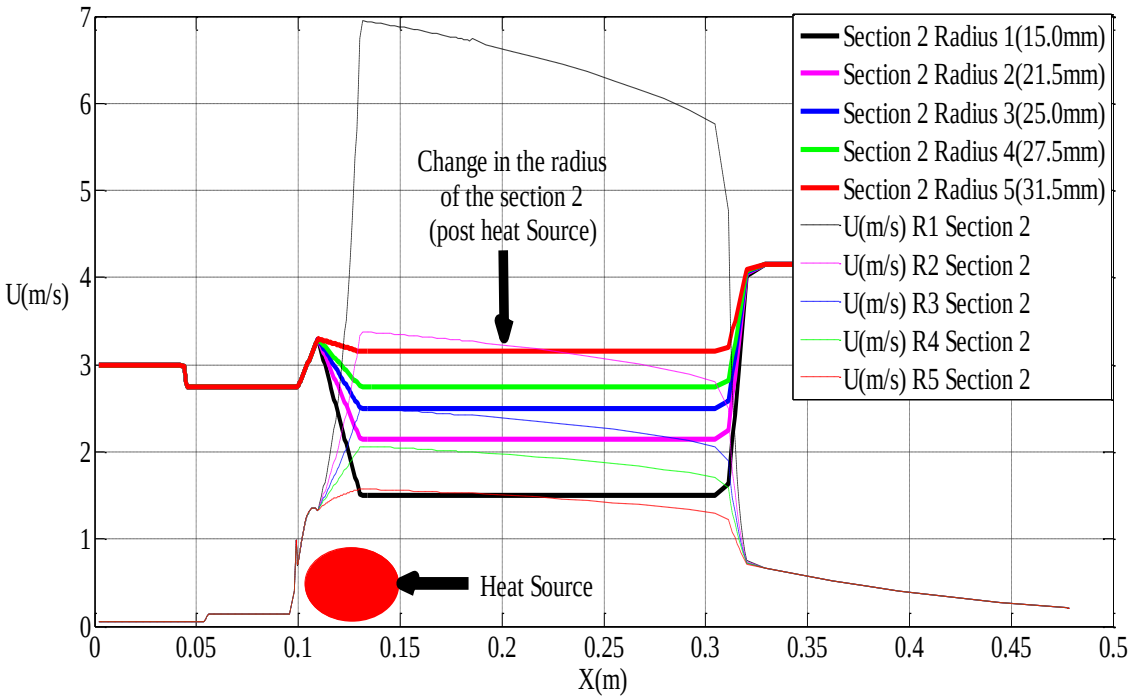

Figure 16. Change in the gas velocity when the radius of the OLC reactor is modified in section 2 (post the heat source). W=5kW, P=1atm, Q=8 L/min.

The change of the velocity in different gas flow rates was monitored in the selected boundary condition for the reactor (see Figure 17). As expected elevating the gas flow rate correlates with a significant raise in the velocity.

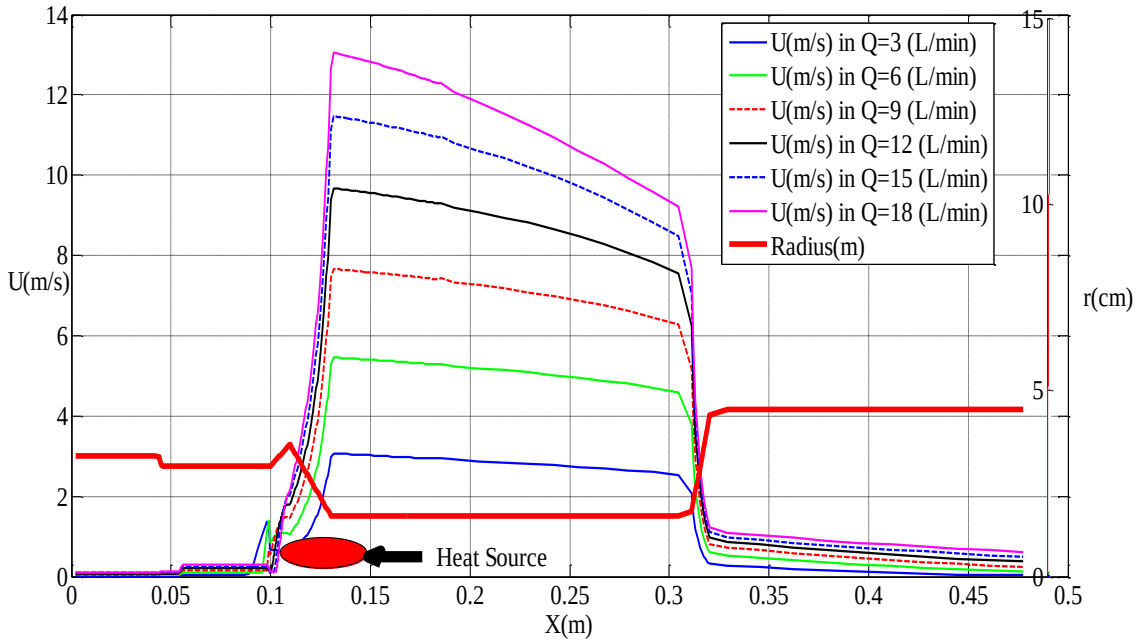

Figure 17. Change in the gas velocity by alternating the gas flow rate. W=5kW, P=1atm.

Figure 18 shows the change in the temperature profile when only the power of the plasma is modified.

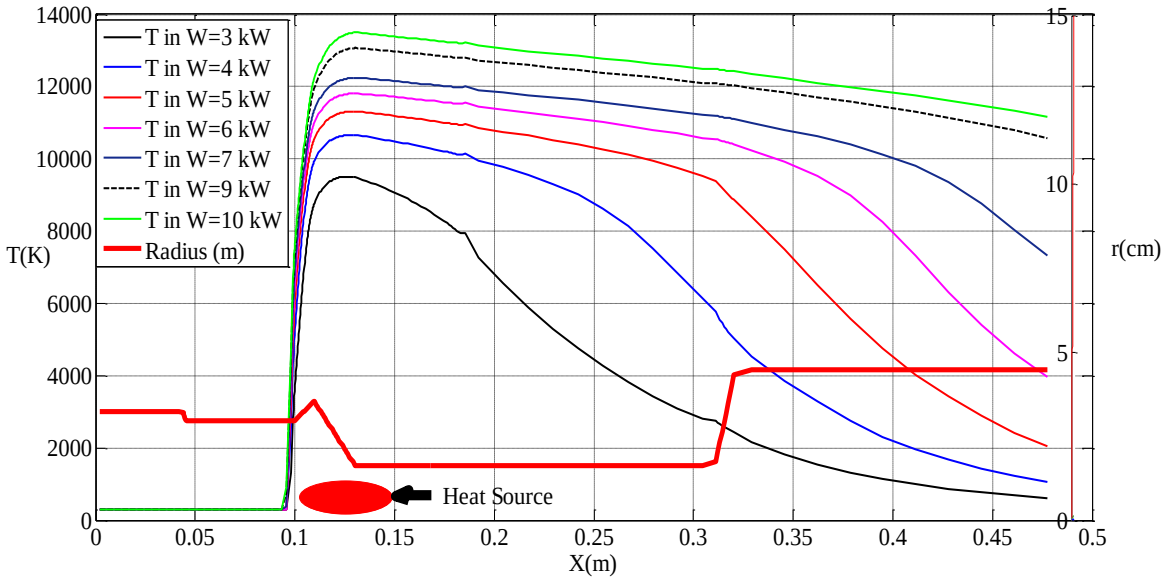

Figure 18.Temperature profile when the power is modified. P=1atm, Q=8 L/min.

As anticipated the power of the plasma has a positive impact on the temperature of the plasma. Since there is a source term in energy equation, by adding to the power the higher enthalpy is attained and, as a result, higher temperature is obtained and propagates further up the reactor. Additionally, at lower power the temperature gradient is considerably larger.

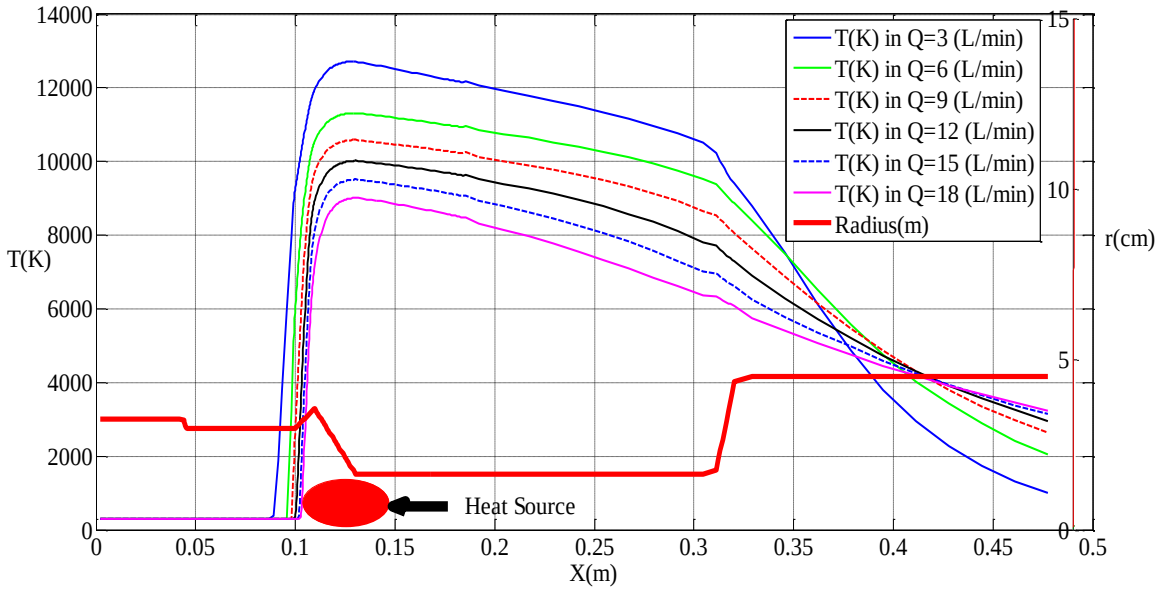

Figure 19.Temperature profile when the gas flow rate is modified. P=1atm, W=5kW.

Figure 19 depicts the change in the temperature of the plasma when only the gas flow rate is changed. Extending the gas flow rate to a higher value decreases the maximum peak of the temperature at the heat source (0.1 to 0.15 m). Furthermore, by moving away from the heat source to a position of 0.35 meters on the X axis shows a conversion in the temperature. This conversion is the result of the high gas flow rate and its impact on heat transfer. Moreover, at a lower gas flow rate diffusion is more dominant. While at high gas flow rate, the temperature behavior is mostly convective. The dominance of convection at high gas flow leads to the conversion of temperature after 0.35 m.

Chapter 4: Methodology

The initial design for the 3-phase plasma reactor was aimed at fullerene production. However, since the energy required for OLC synthesis is less than for fullerene and also the formation process for the fullerene and the OLCs is different, a specific approach for the OLC reactor design was taken by the nano group. The fullerene reactor required a quenching zone since the feedstock needed vaporization but the OLC reactor did not demand vaporization and only required heat treatment of the source material. Furthermore, fullerene is obtained through sublimation and requiree a more sensitive collection method. However, OLC does not require any post collection process. Moreover, the presence of impurities in the collection chamber can affect the final product in OLC formation. The next section elaborates on the construction of the OLC reactor and the design approach taken by the UNB Nano Team.

4.1 Reactor design

The plasma is powered by a 3-phase step down transformer. Each phase of the transformer is connected to an inductor which regulates the current. The reactor consists of a plasma torch, a heat treatment zone, and a collection zone as shown in Figure 20. The torch consists of three water cooled brass electrodes. The water cooling system is monitored by a flowmeter. A graphite electrode holder with graphite tips is screwed to the top of each brass electrode. The electrodes are co-planar. The electrodes are placed in a G10 (insulative glass-filled structural epoxy) flange with the angular displacement of 120 degrees (see Figure 21). A heat shield made of fire brick is located on the top of the G10 flange in order to protect the flange from thermal shock and heat produced by plasma.

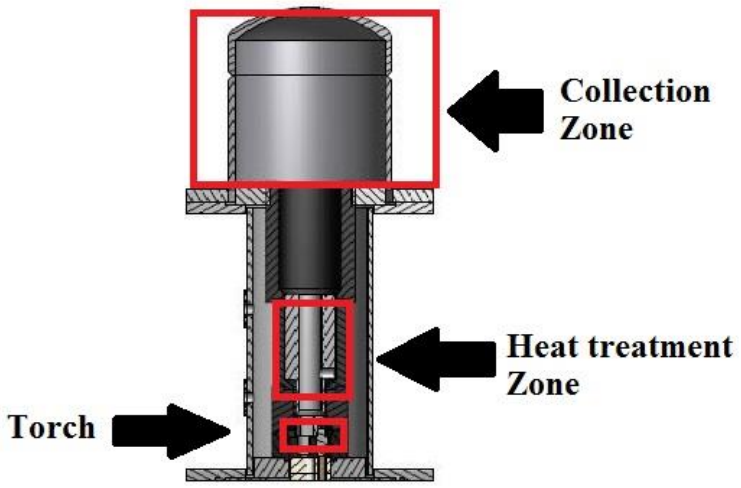

Figure 20. The three main sections of the plasma. Torch zone, heat treatment zone, and collection zone.

The details of the torch assembly are depicted in Figure 20. Each brass electrode is electrically insulated via the G10 flange and is connected to one of the inductors.

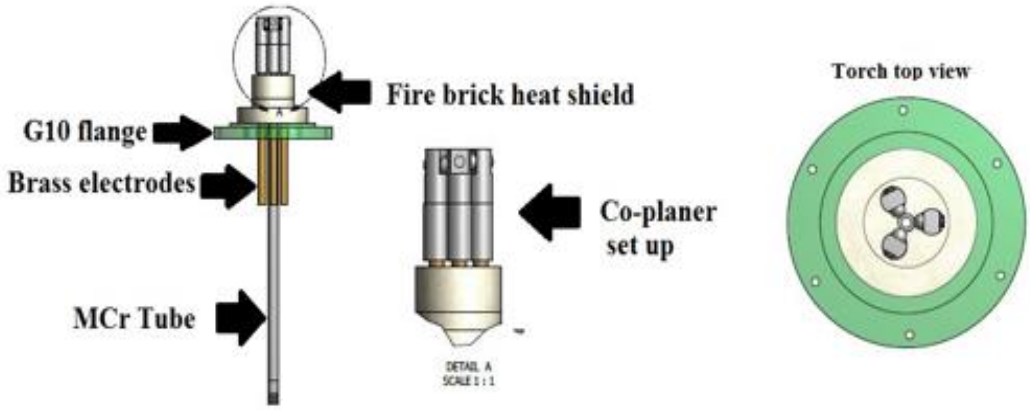

Figure 21. Torch assembly.

Furthermore, a tube constructed from machinable ceramic is inserted in the center of the G10 flange. The plasma gas is injected into the plasma zone through this MCr tube. The plasma zone is encompassed by a graphite cylinder. The graphite

cylinder column is placed in a steel chamber. Ceramic wools are used to provide thermal and electrical insulation between graphite and steel chamber (see Figure 22(green)). Also, the bottom flange, which is made out of steel, is water-cooled to protect the G10 flange against thermal shocks. The collection chamber is constructed in the shape of a dome from steel. Figure 22 illustrate the OLC reactor body. Furthermore, to monitor the plasma, allow visual supervision, and permit diagnosis of the plasma, 6 viewports are positioned along the plasma and the heat treatment zones. Also, the temperature of the graphite chamber is inspected by utilizing 3 K-type thermocouples.

Furthermore, a tube constructed from machinable ceramic is inserted in the center of the G10 flange. The plasma gas is injected into the plasma zone through this MCr tube. The plasma zone is encompassed by a graphite cylinder. The graphite cylinder column is placed in a steel chamber. Ceramic wools are used to provide thermal and electrical insulation between graphite and steel chamber (see Figure 21(green section)). Also, the bottom flange, which is made out of steel, is water-cooled to protect the G10 flange against thermal shocks. The collection chamber is constructed in the shape of a dome from carbon steel. Figure 22 illustrate the OLC reactor body. Furthermore, to monitor the plasma, allow visual supervision, and permit diagnosis of the plasma, 6 viewports are positioned along the plasma and the heat treatment zones. Also, the temperature of the graphite chamber is inspected by utilizing 3 K-type thermocouples.

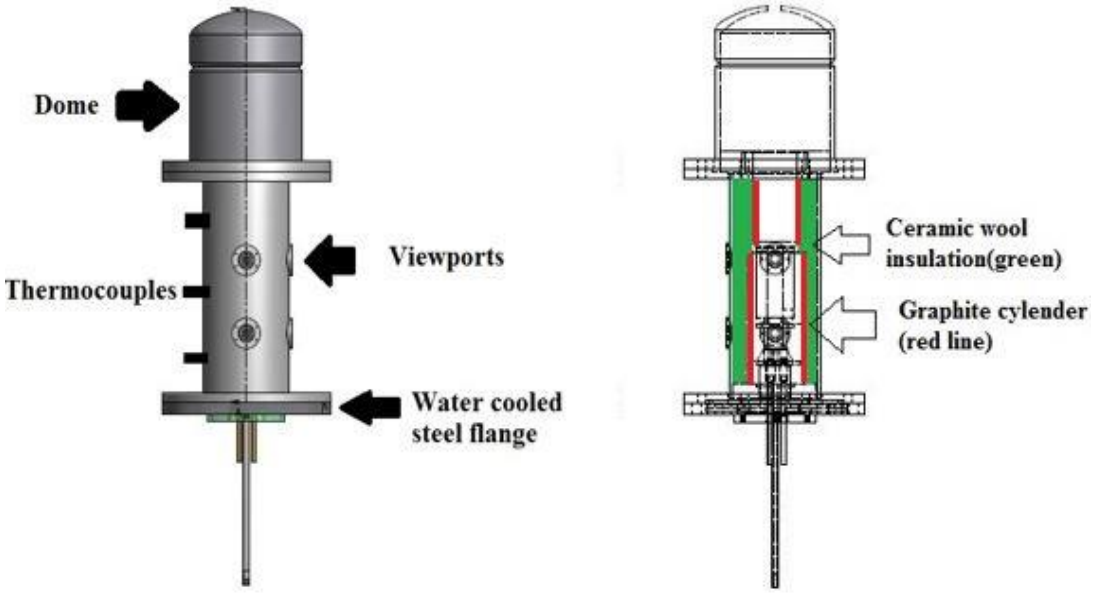

Figure 22. The OLC reactor.

The process can be briefly explained as follows: the plasma is ignited by the means of a fourth electrode, as an ignition electrode, from the top of the reactor. The plasma is generated when the plasma gas is ionized in the presence of the electromagnetic field provided by the power supply. As the arc length increases, its power consumption increases and the voltage is not enough to maintain the arc. The arc extinguishes and the cycle repeats with a new arc generating at the tip of the electrodes. The carbon feedstock is carried from a carbon powder feeder via the plasma gas. The carbon concentration carried into the plasma can be controlled by the carbon powder feeder. Since the plasma gas is argon in this experiment, the electrode erosion in this method is minimal and a continuous stable plasma with remarkably high enthalpy maintenance is generated. The samples are collected from the primary collection zone and the secondary collection zone collects the really small particles that could reach that height due to buoyant force. Figure 23 displays the schematic of the apparatus setup of the OLC reactor.

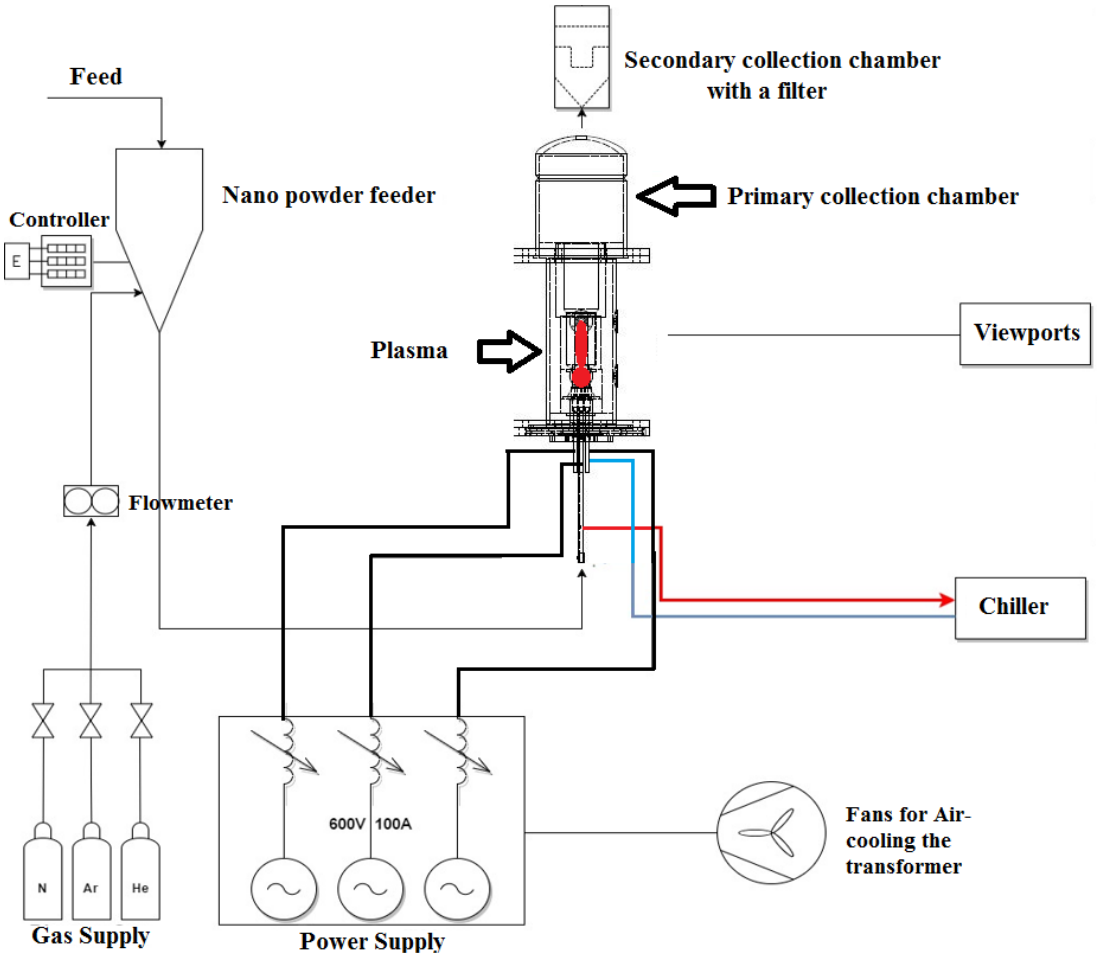

Figure 23. Schematic of the apparatus setup [72].

4.2 Instruments

4.2.1 Power Supply

The power supply electric diagram is presented in Figure 24. The step-down transformer 600/208 V with current-limiting inductors allows the power system to be controlled by varying the inductance of the power source, making possible a range from 110-250A. The inductance of current limiting reactors can vary in the operating systems

[73]. The inductance used in the experiments is 4.2 mH. Furthermore, the current and the voltage of each electrode is inspected by utilizing 3 oscilloscopes.

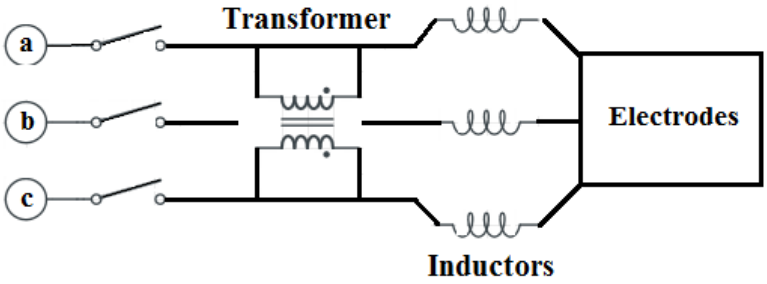

Figure 24. Circuit diagram of the power supply.

The working connector of each inductor is fixed to an electrode and the grounding terminals are connected together as a common floating ground. The power supply is wired from a primary 3-phase source to be 120˚ out of phase with each other in order to promote arcing between the electrodes. This setup is planned to provide reliable, continuous, and stable operation of the plasma, and is connected with arc movement along the co-planar electrodes. The connection of the inductors as a part of the power supply is shown in Figure 25.

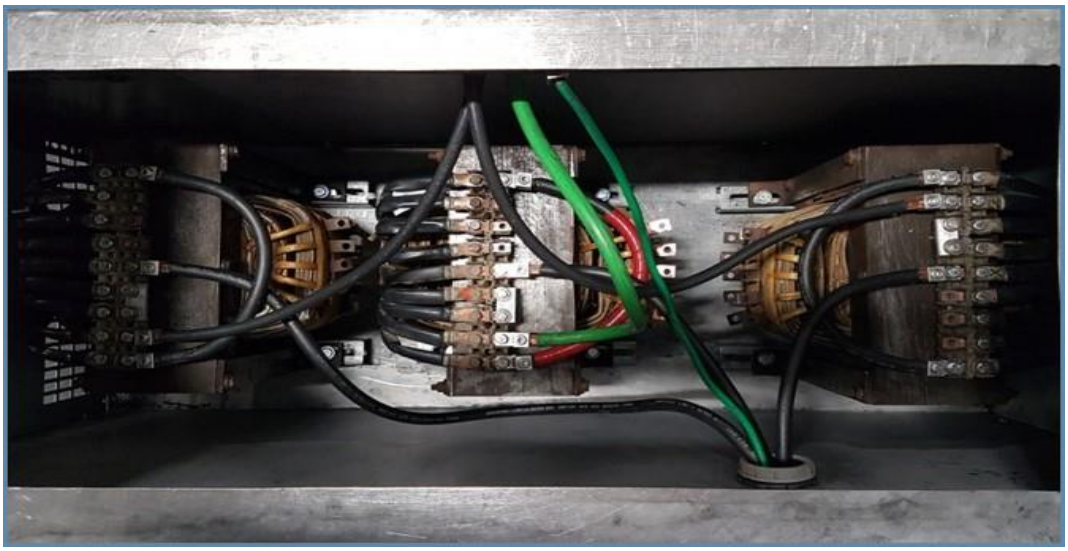

Figure 25. Inductors as a part of the power supply.

4.2.2 Carbon injection via Nano powder Feeder

The PFR400 is the latest model of powder feeders developed by Tekna Plasma Systems Inc. (see Figure 26). It is designed to feed fine and ultrafine types of powder with a constant controlled feed rate. The PFR400 can be used for powder size ranging from 8 nm to 5 µm. The ultra-sonic device provides the advantage of pasting powder feeding without any problems [74].

Figure 26. Tekna PFR 400 nano feeder [74].

Several mesh disks are utilized in determining the particle-size distribution of a powder material. When the brush is rotating over the disk (see Figure 27), pieces smaller than the mesh size pass through the mesh while larger particles are retained on the mesh. This type of feeding enables uniform feeding. Figure 27 displays several standardized mesh disks available for different particle sizes. The powder feeder provides control over carbon concentration in the OLC reactor.

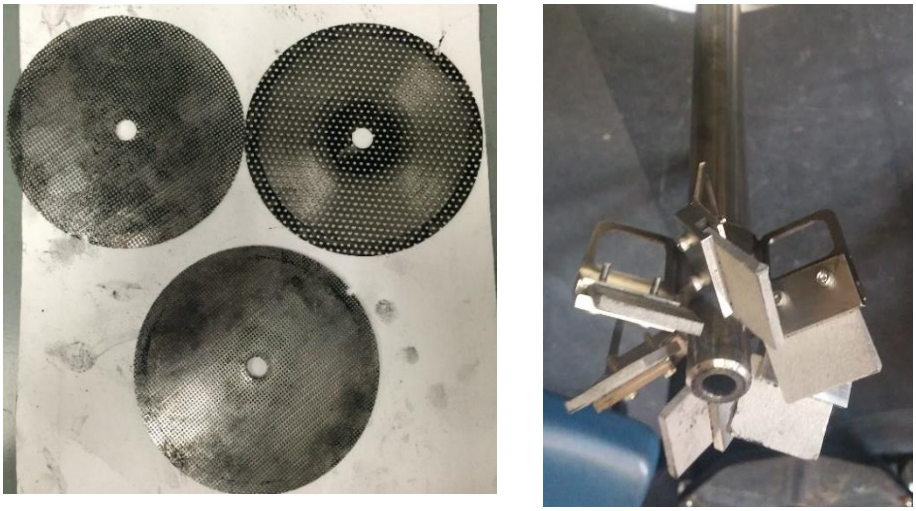

Figure 27. Mesh disk for nano powder feeder (left) and brushes (right).

An ultrasonic zone is located after the disks which prevents the agglomeration of the pasting powder. In order to ensure smooth transition of the powder and prevent clogging, the bottom of the feeder is machined in a conical shape. The conical exit is then followed by a quarter inch tube that carries the powder to be fed to the plasma. The powder feeder incorporates the following features [74]:

- Purge ports for inert gas purge
- Pressure port for back pressure reading
- Pressure relief valve
- Ultrasonic vibration system that ensures continuous feeding of the less-flowing fine powders
- highly polished SS inner surface
- Heating blanket
- Smooth transition of the feedstock

With the defined operating specifications [74]:

Powder size: 0.01-5 μm powder

Powder feed rate: 0.1-5 kg/h (depending on powder characteristics)

Maximum pressure: 200 kPa (15 psig)

Minimum pressure: 100 kPa (-15 psig)

Canister volume: 10-15 liters

Carbon feed rates are manually determined at different revolutions per minute (rpm) set points for carbon feedstock, and calibrated to the feedstock specification. Furthermore, a heat tape is wrapped around the outer shell of the feeder which is set to 100℃. The heat generated by the heat tape is helpful in transferring the feedstock through the system. Table 6 shows the specification of the feeder for the chosen carbon feedstock, N234.

Table 6. Carbon powder feeder calibration for the N234.

Brush Revolution (Rpm)	Carbon concentration (Gram per min)
0	0
0.2	1
0.3	1.45
0.4	1.8
0.5	2.25
0.6	2.75
0.8	3.5

4.3 Design of the experiment

The goal of the project is to establish the parameters that affect OLC synthesis with the 3-phase reactor. A design of experiments strategy was implemented. To assess the effect of residence time and carbon concentration on OLC conversion, a 2x3 set of experiments was designed. The 3 gas flow rates used in the experiments were 12, 15, and 18 SLM[5] (standard liter per min). Carbon concentration injected into the plasma

[5] According to the MKS flowmeter standard type 1479A 1 sccm = 1 standard cm^3/min; standard conditions: 1013.25 mbar and 0℃. 1 slm = 1 standard liter/min = 1000 sccm.

was controlled by the carbon powder feeder. The chosen three carbon concentrations were 1, 2.25, and 3.5 grams per minute which were obtained by adjusting the rpm of the nano powder feeder to 0.2, 0.5, and 0.8 rpm respectively.

The operating plasma gas was argon. The inductance of the inductors after the step-down transformer were 3.9 - 4.2 mH which led to plasma current and voltage of 135 A±5 and 25 V±5 respectively. This resulted in the plasma power of about 5 kW. Table 6 shows the operating conditions of the experiments. The volume of the heat treatment zone was constant and the temperature of the graphite chamber wall were monitored by 3 K-type thermocouples. Also, all the experiments were conducted at atmospheric pressure. The feedstock chosen for the experiment was N234. N234 is an amorphous carbon with low degree of graphitization which will allow easier comparison upon heat treatment. Each carbon concentration was tested on 3 different gas flow rates. According to the data gathered from the quasi-2D model, changing the gas flow rate affects the residence time (see Figure 16). Thus, the residence time of the carbon exposure could be investigated by changing gas flow rate.

Table 7. Operating conditions of the experiments.

Plasma Gas	Argon
Gas flow rate	12,15,18 (SLM)
Carbon concentration	1.2, 2.25, 3.5 (gpm)
Power(rms)	5kW±20% I=135 A±5, V=25 V±5
Carbon feedstock	N234 carbon black
Pressure	1atm

For each experiment the collection zone was washed clean by ethanol. The reactor was preheated to a minimum of 400℃ at bottom chamber. The current and voltage of the lines were monitored to assure consistency.

In order to investigate the conversion of the feedstock to the OLC, characterization of the heat-treated feedstock was required. Hence, each sample was characterized by TGA (thermogravimetric analysis), Raman spectroscopy, and TEM (transmission electron microscopy). Then, the results were compared to the N234 before plasma treatment and a commercial highly graphitized carbon black (LiTX50, Cabot Corporation). LiTX50 was chosen as a reference OLC to represent full conversion. Moreover, the characterization was only conducted on the samples gathered from the collector. Table 7 illustrates the operating conditions of the samples. The next section elaborates on the characterization methods utilized in this study.

Table 8. The operating conditions of each sample.

Run	Gas flow rate (SLM)	Carbon concentration (gram per minute)
0403A	12	1
0403B	15	1
0403C	18	1
0404A	12	2.25
0404B	15	2.25
0404C	18	2.25
0405A	12	3.5
0405B	15	3.5
0405C	18	3.5

4.4 Characterization

4.4.1 TGA

Thermogravimetric analyses were performed by QA 600 TA instrument. The 3-10 mg samples were heated up to 900 ℃ in air from room temperature at the rate of 20 ℃/min. The changes in the mass of the sample while temperature increased were monitored. TGA is a quantitative analysis [75]; by comparing the mass loss as a function of temperature, the oxidation profiles can be defined. In this case, TGA depicts initial oxidation temperature, the final temperature, and the residual mass percent [76]. Specifically, $T_{5\%}$ represents the temperature at which the 5% of the original mass was lost. All data are normalized to initial sample weight and the weight percent loss vs temperature is shown for each sample, the feedstock, and the reference OLC which aims to investigate the effect of the residence time and carbon concentration on the conversion of the carbon to reference OLC. Figure 28 shows the weight percent loss vs temperature diagram of the LiTX50 and the N234.

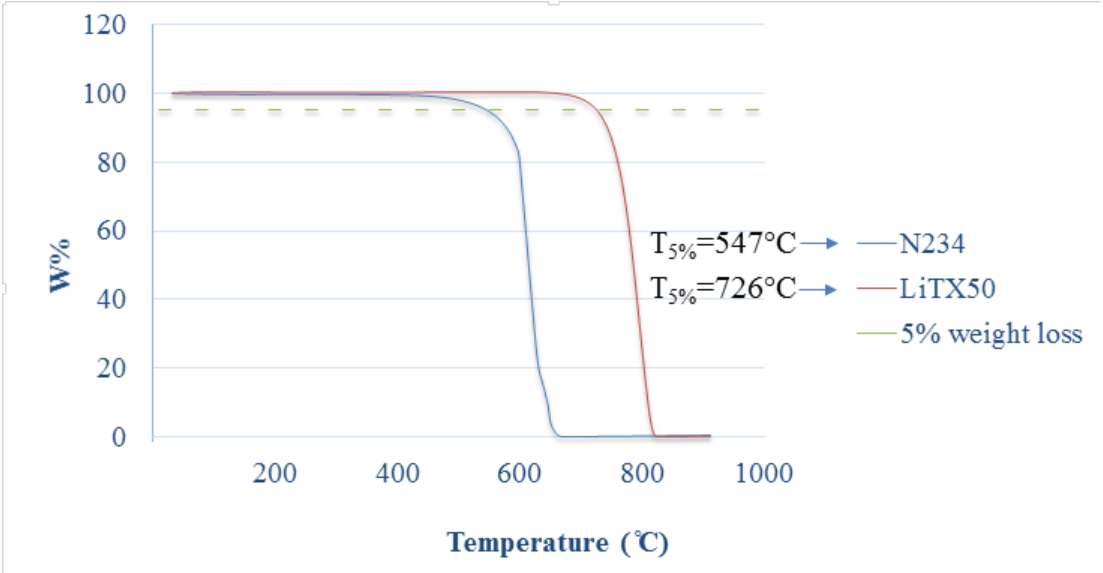

Figure 28. TGA of the source material and OLC.

As Figure 28 displays, N234 initiates 5% burning at 547℃ while LiTX50 only starts to burn at 726℃. This phenomenon can be explained by high degree of graphitization and the absence of defects in OLC structure.

4.4.2 TEM

TEM uses electrons as a light source with a low wavelength to get a resolution which remarkably exceeds an optical microscope's resolution. Transmission Electron Microscope JEOL 2011 was used to obtain an atomic scale resolution of the samples and investigate planar and line defects, grain boundaries, interfaces, etc. The transmission electron microscope is generally used to characterize the microstructure of materials with very high resolution to reveal information about the morphology, crystal structure, and defects [7, 15, 23, 26]. TEM can provide comprehensive analysis since it grants nano-scale visualization of the samples which is beneficial in identifying the structure of the nano materials. Figure 29 compares the TEM image of the N234 carbon black and the LiTX50.

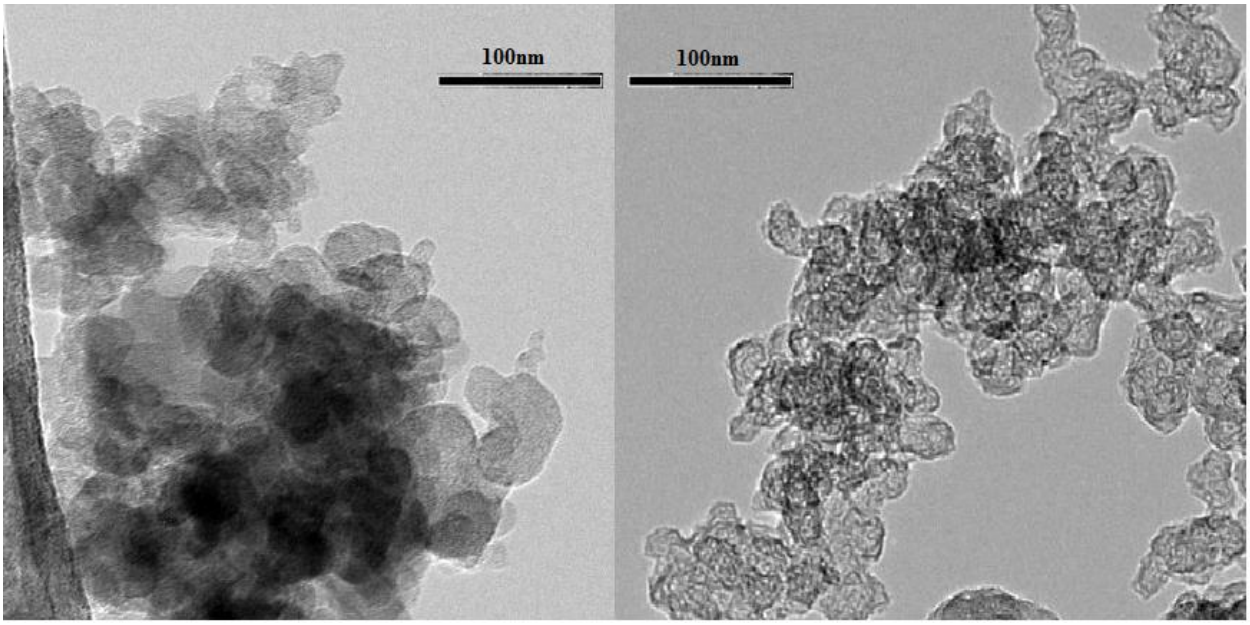

Figure 29. TEM image of the N234 (left) vs LiTX50 (right).

The N234 displays agglomeration of the amorphous structure of the carbon black. However, the OLC image reveals the quasi spherical structure with layers in the shape of onions [77].

4.4.3 Raman Spectroscopy

Raman spectroscopy measures the light emitted by an experimental sample under laser illumination. After striking a very small portion of the sample, the laser beam is scattered at a different frequency than the excitation laser; which as a result a Raman shift is created. Raman shift presents vibrational, rotational, and other low frequency transitions in molecules.

The Raman spectra were conducted at room-temperature by utilizing a Renishaw 1000 micro-Raman system equipped with a Leica microscope. The excitation wavelength used was 514 nm from a helium Neon laser. Measurements were performed from 1000 cm^{-1} to 2000 cm^{-1} on each heat-treated sample.

Since Raman spectroscopy provides a non-destructive and preparation-free estimate of carbon content, it is considered an effective tool in characterizing the carbon. In general Raman spectra of the carbon molecules shows two peaks between 1000 cm^{-1} and 2000 cm^{-1}. These peaks approximately appear on 1380 cm^{-1} and 1580 cm^{-1} which are known as D band and G band [20, 25, 78]. The D or defect band contributes to the vibrations of the carbon atoms with dangling bonds. The presence of the D band is due to disruptions in the sp^2 bonding such as dangling bonds, heptagons and pentagons carbon rings, foreign atoms, vacancies, and amorphous carbon [46]. On the other hand, the G band corresponds to the stretching mode of the -CC- bond in the graphite plane. The ratio of G to D which is indicated by I_G/I_D implies the degree of crystalline perfection [75]. Figure 30 illustrates the atomic bonds in D and G bands.

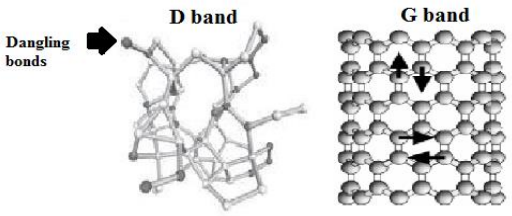

Figure 30. Schematic picture showing the atomic bonds in D band (left) and G band (right)[79]

Figure 31 displays the Raman spectroscopy of N234 and OLC and their respective D and G bands. The ratio of I_G/I_D for N234 and OLC are 1.225 and 1.404 respectively. Furthermore, to investigate the Raman shift the half width at half maximum (HWHM) for each sample was measured. I_G/I_D presents the ratio of sp^2 bonds to defective sp^3 bonds while measuring HWHM indicates the structural distribution [80]. The HWHM for OLC and N234 are 32 cm^{-1} and 79 cm^{-1} respectively. N234 exhibits a wider HWHM than the OLC which indicates more intense distribution of the defects and the dangling bonds in the structure.

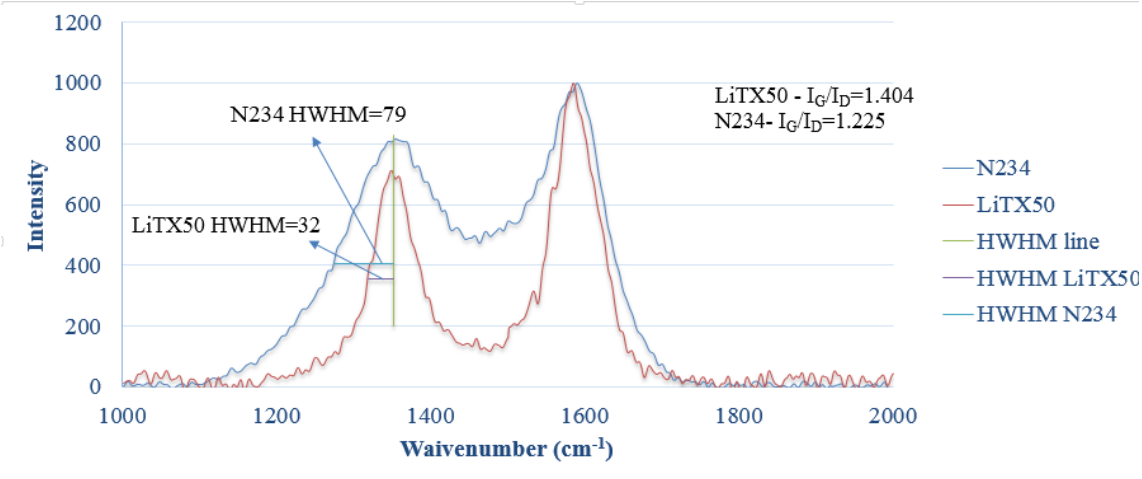

Figure 31. The Raman spectroscopy of N234 and LiTX50.

Chapter 5: Results and discussion

5.1 TGA

The TGA of the samples depicts a meaningful delay in the initiation of the mass loss. The cause for this delay can be found in the heat treatment of the feedstock and its duration.

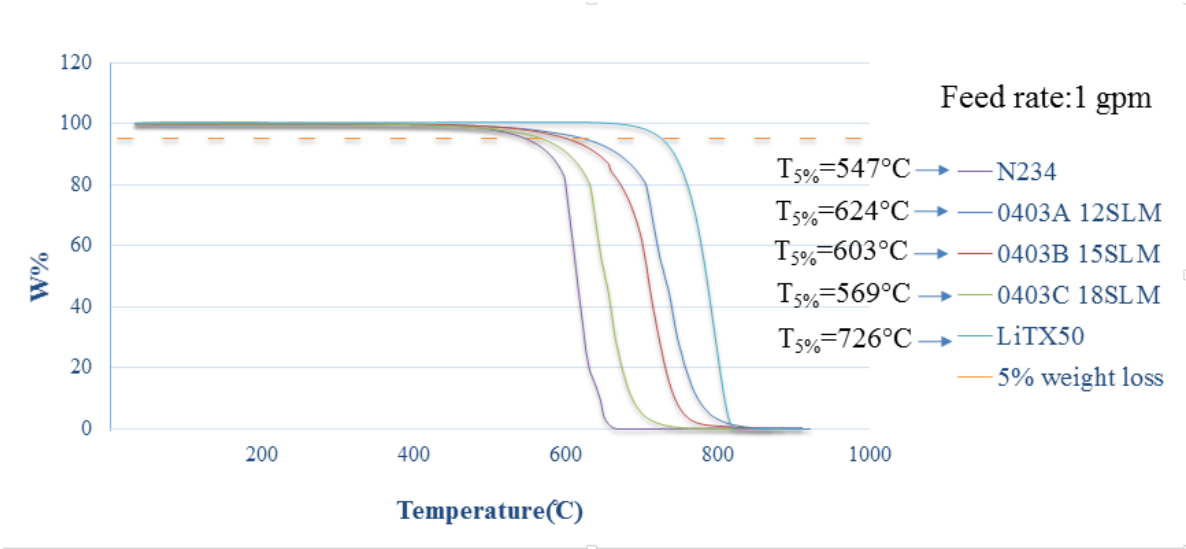

Figure 32. TGA of the 0403 series (1 gpm).

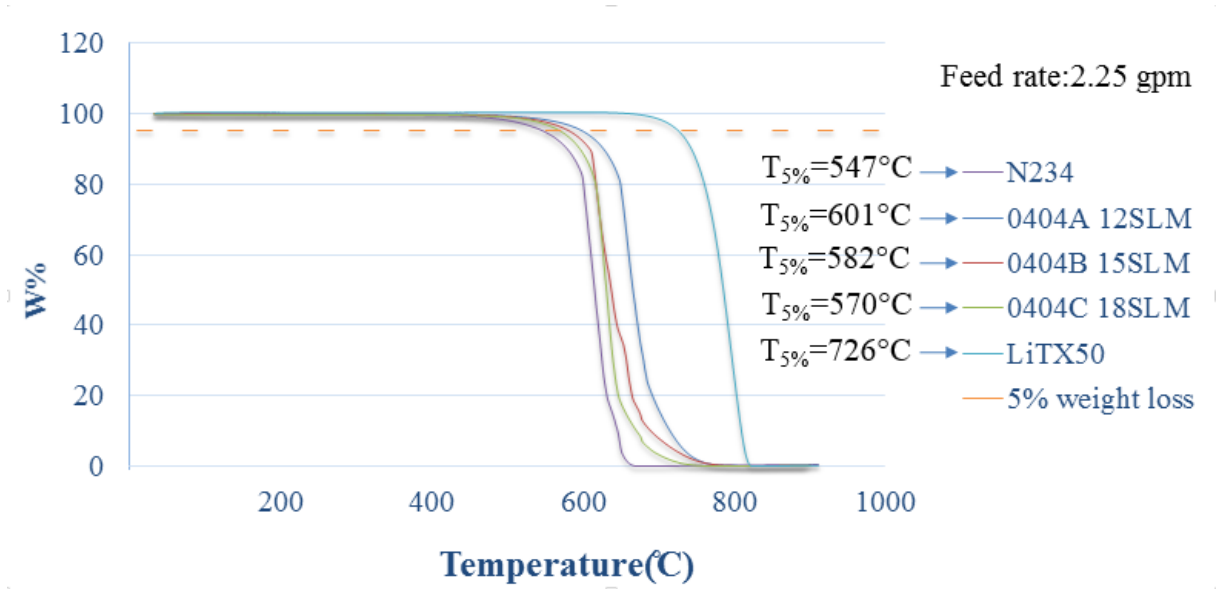

Figure 33. TGA of the 0403 series (2.25 gpm).

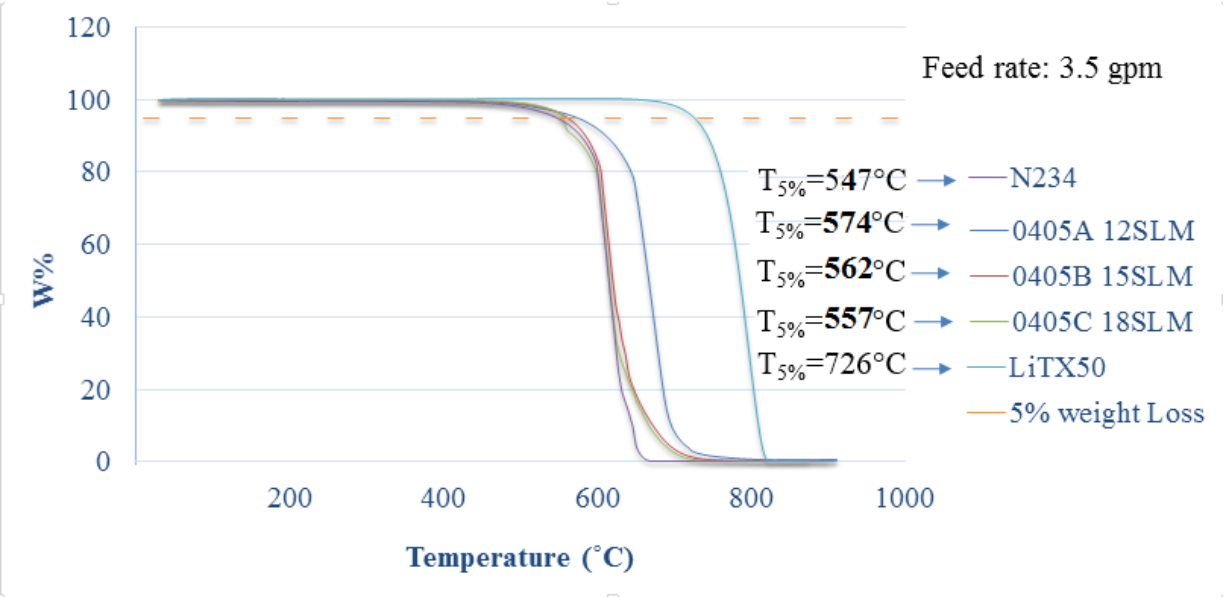

Figure 34. TGA of the 0403 series (3.5 gpm).

Figure 32, 33, 34 illustrates the TGA diagram of the samples in 0403, 0404, and 0405 series respectively. As Table 7 displays, the carbon concentration is changed in each series. Furthermore, at each series the gas flow rate is maintained at different levels: 12, 15, and 18 SLM. The other parameters of the runs are shown in Table 6. Figure 35 presents the TGA diagram of the samples in different concentration when the gas flow rate was at 12 SLM.

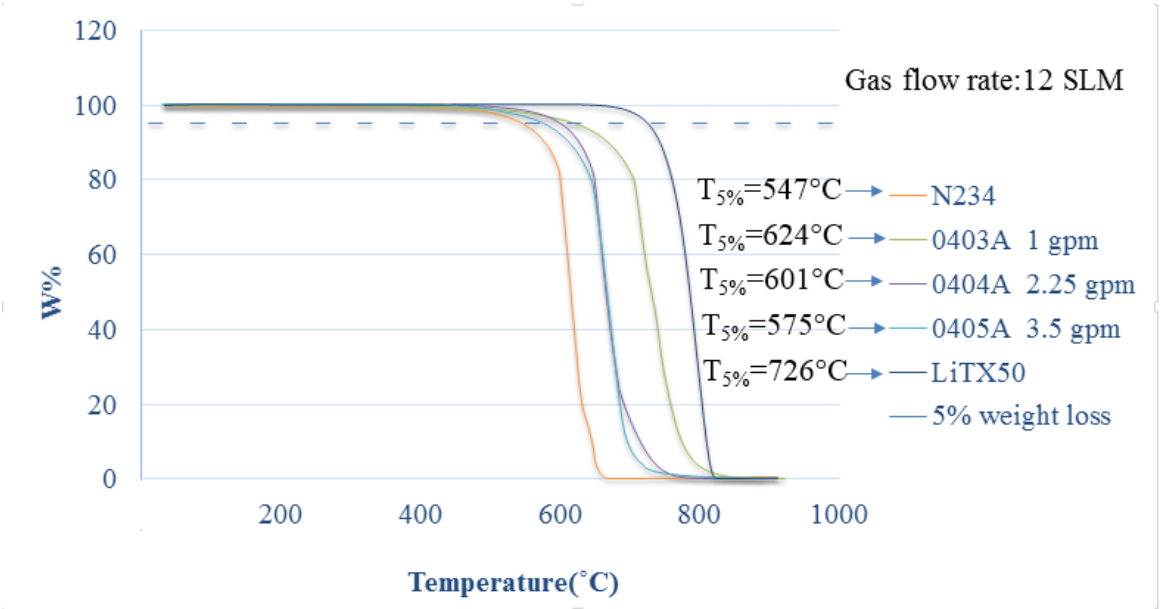

Figure 35. The TGA of the samples in different carbon concentration.

5.1.1 TGA Analysis

The TGA diagrams shows a delay in the temperature of $T_{5\%}$. The mass loss in N234 carbon black starts at 547˚C while in the reference OLC the mass loss does not begin until approximately 726˚C. The $\Delta T_5\%$ between the LiTX50 and the N234 carbon black is 179˚C, will define 100% conversion of N234 to OLC. Therefore, dividing the ΔT% of the plasma samples with N234 over the reference $\Delta T_{5\%}$ the ratio of the conversion (see Equation 28). These results vs the gas flow rate and carbon concentration are depicted in Figure 36.

$$\text{TGA conversion ratio} = \frac{Sample\Delta T5\% - N234ample\Delta T5\%}{LiTX\Delta T5\% - N234\Delta T5\%} \quad (28)$$

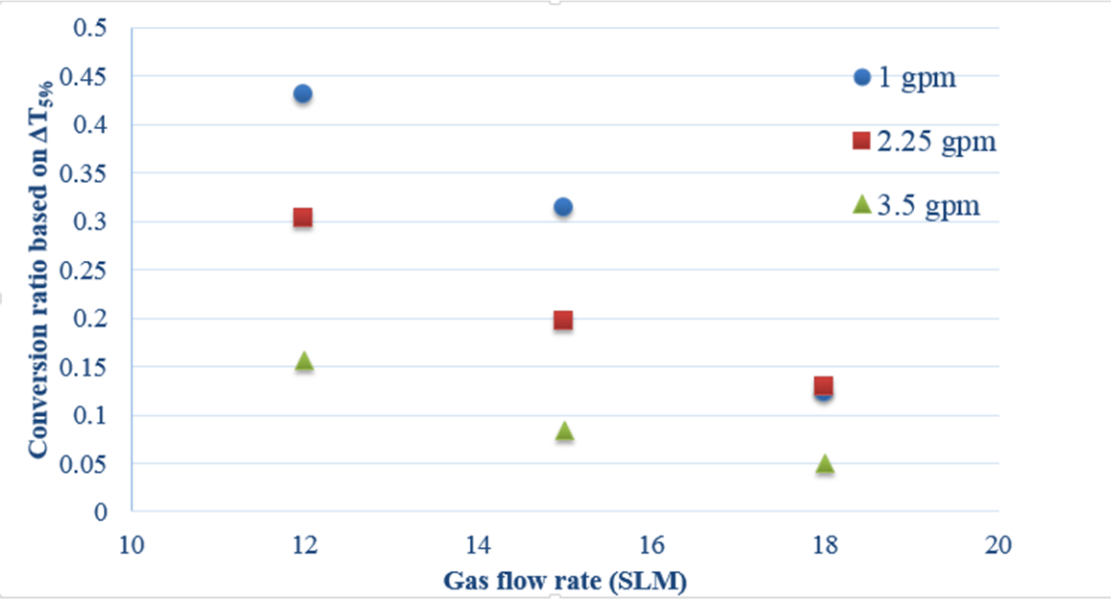

Figure 36. The conversion ratio vs gas flow rate.

In Figure 36, it is observed that by increasing the gas flow rate, which consequently reduces the residence time, conversion decreases for all carbon concentrations. As well, overall the conversion decreases with increased carbon loading. Since the plasma power is constant, introducing more feedstock to the chamber requires more energy to heat treat the source carbon and as a result, conversion declines

remarkably which is in agreement with literature. Furthermore, the rate of residence time effect is more pronounced with decreasing carbon loading. The highest ratio of the conversion as determined by this TGA method is almost 43%, obtained at the lowest gas flow rate and carbon concentration. This signifies that conversion rate favors longer residence time and lower carbon concentration.

5.2 TEM

The TEM results of the samples before and after the plasma exposure, as shown in Figure 37, reveals significant change in the structure of the feedstock. The N234 carbon black presents amorphous structure with general spherical shape and no specific formation in the interlayer of the clusters and particle size of approximately 120 nm (Figure 37a). However, the carbon black after the heat treatment (Figure 37 b, c, and d) shows the quasi graphitic structure formed by the 3-phase plasma process. The operating conditions for Figures 37b, 37c, and 37d were 12, 15, 18 SLM respectively, attained at a carbon feed rate of 2.25 gpm. Comparing Figures 37b to the N234 TEM image reveals significant change in the structure of amorphous carbon as a result of the heat treatment. In Figure 37b the graphitic shells are smaller (20-30nm) and quasi-spherical shell structure is conspicuous. While Figures 37c and 37d also depict conversion to the onion structure, the onion shape only occurred in a fraction of the samples and is not as significant as in Figure 37b. In Figure 37c there are some graphitic shells; however, a portion of the sample reveals no conversion and particle sizes are slightly larger than shown in Figure 37b. In Figure 37d a wider range of the samples appears to be untreated. The reason for less conversion in 37b and 37c could be related to the lower residence time which is in agreement with TGA results. Moreover, Figure 37d is the visual proof for this conclusion since only a small portion of the sample is converted to the onion structure due to high gas flow rate.

The TEM images also imply that conversion starts from the outer layer of the amorphous carbon and move towards the interlayers of the particles. Moreover, the graphitic interlayer spacing can be observed in Figure 37b.

Due to the small sample size (less than 0.1mg) it is not possible to obtain conversion ratios that are representative of bulk samples. In order to further investigate the samples and the effect of the plasma on their conversion to the OLC, the Raman spectroscopy of the samples is monitored in the next section.

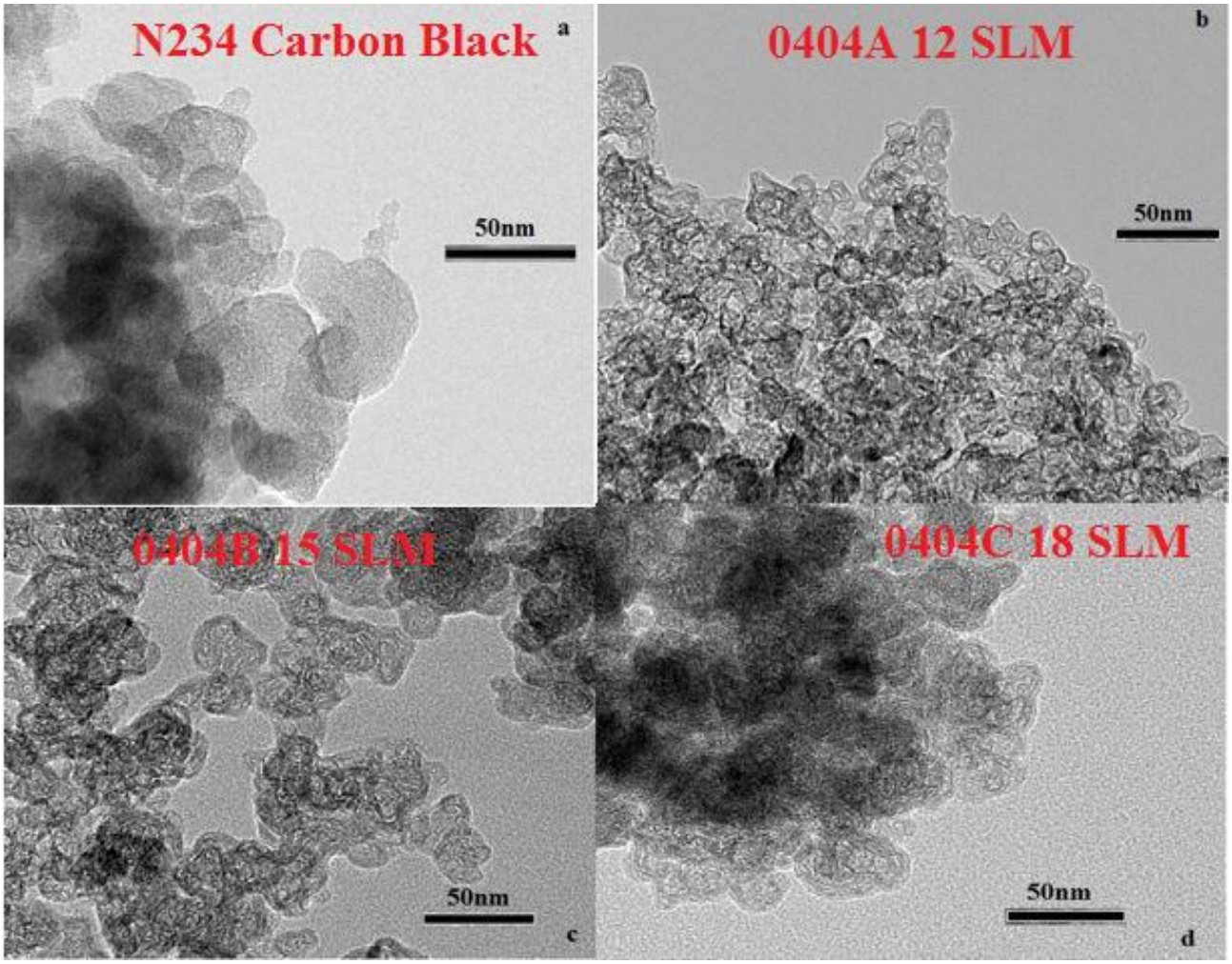

Figure 37. The TEM image of the N234 carbon black before (a) and after plasma treatment (b) 12 SLM, (c) 15 SLM, and (d) 18slm at 2.25 gpm.

5.3 Raman Spectroscopy

Raman spectroscopy of the samples is presented in Figure 38, 39, and 40 which show the result for samples 0403, 0404, and 0405 respectively. As mentioned before in each series of the experiments carbon concentration is alternated while the gas flow rate is set to 3 different levels 12, 15, and 18 SLM. Each Figure illustrates the HWHM of the D band for the specific run at different gas flow rates. Decreasing the gas flow rate shows a positive effect on HWHM since the values of the HWHM of the D bands is declining. Furthermore, the presented Raman shifts show the ratio of the G to D band, I_G/I_D , which is the indicator of the proportional relation between perfect and defective structure.

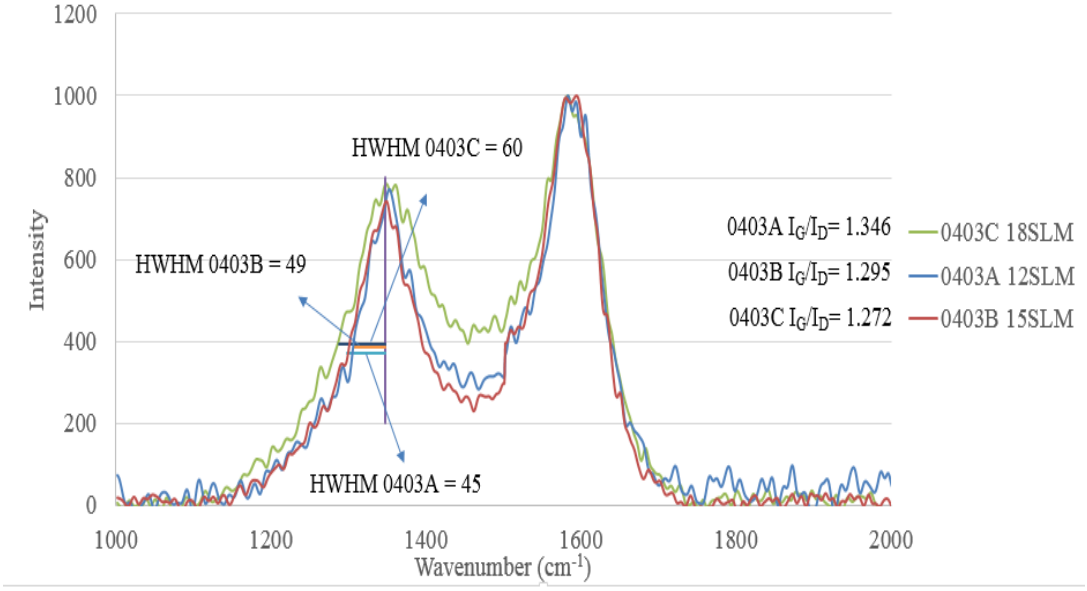

Figure 38. Raman shift of the 0403 series (carbon concentration 1 gpm).

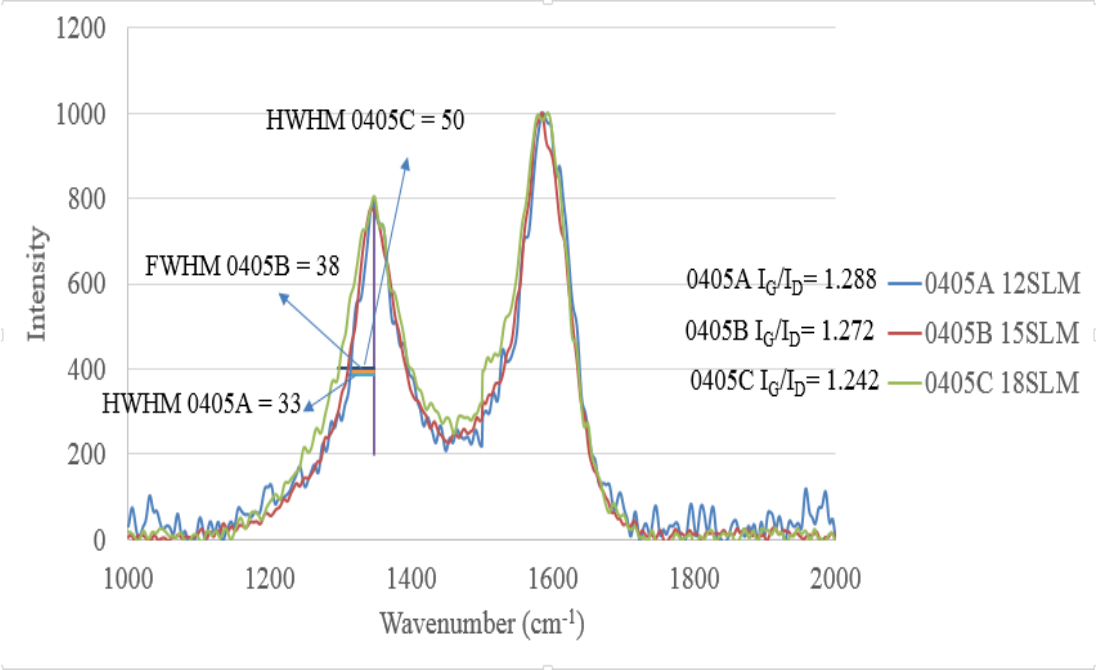

Figure 39. Raman shift of the 0404 series (carbon concentration 2.25 gpm).

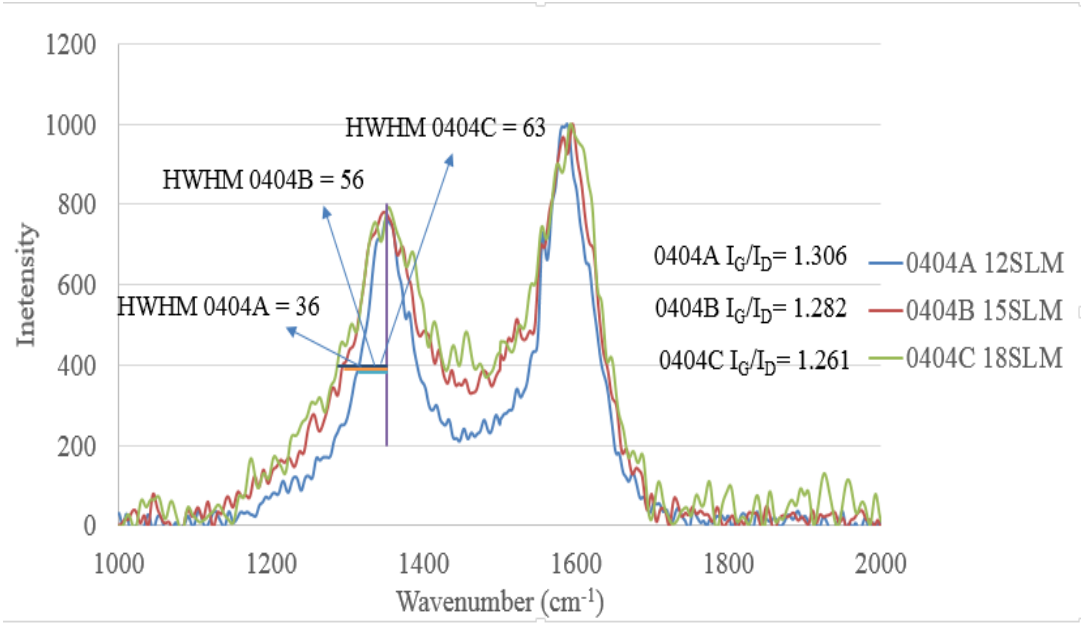

Figure 40. Raman shift of the 0404 series (carbon concentration 3.5 gpm).

5.3.1 Raman analysis

Measuring the HWHM and the I_G/I_D ratio can aid in the investigation of chemical structure of the heat treated amorphous carbon. The HWHM at D band shows the distribution of the defects and the I_G/I_D ratio depicts the proportion of the perfect structure, in this case graphitization, to the defects. In pure graphite, the D band is

almost nonexistent expected since there are very few sp^2 defects. However, the OLC does not appear to generate the same characteristics. In the LiTX50 the graphite sheet is curved to form a quasi-sphere which generate the D band type defects.

The I_G/I_D of the OLC seems to be approximately 1.404 while the I_G/I_D ratio of the N234 carbon black is 1.225 (see Figure 31). The conversion ratio based on the I_G/I_D with LITX50 representing 100% conversion was calculated in similar manner (see Equation 29) as TGA results (see Figure 41). Furthermore, the HWHM at the given gas flow rate and carbon feed rate is presented in Figure 42.

$$\text{Raman } (I_g/I_d) \text{ Conversion ratio} = \frac{Sample\left(\frac{Ig}{Id}\right) - N234\left(\frac{Ig}{Id}\right)}{LiTX\left(\frac{Ig}{Id}\right) - N234\left(\frac{Ig}{Id}\right)} \tag{29}$$

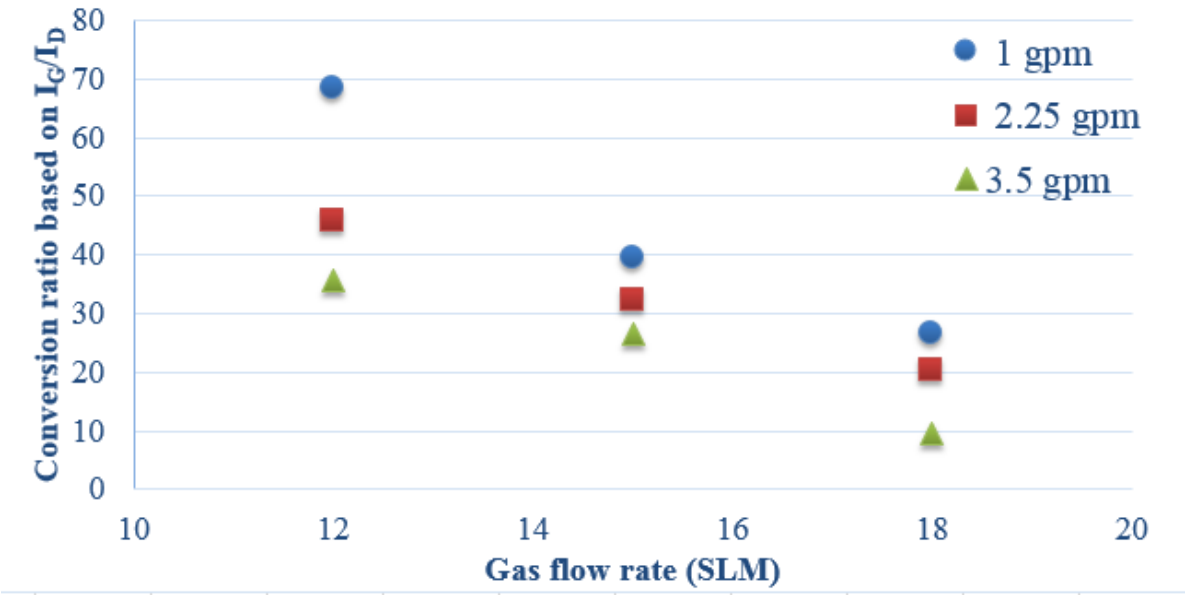

Figure 41. Conversion ratio according to I_G/I_D.

As Figure 41 shows, the conversion ratio is higher at low flow rates, and thus longer residence time. Similarly increased carbon loading decreased the conversion efficiency at all gas flow rate. Compared to the TGA conversion ratio, higher values are attained by the Raman spectroscopy characterization method. The highest

conversion was obtained at the flow rate of 12 SLM and feed rate of 1 gpm which was approximately 68%.

The conversion ratio based on Raman spectroscopy and TGA display almost similar trends. This supports the hypothesis about the residence time which indicates that higher residence time leads to better conversion. The same trend can also be found in the HWHM diagram. Since the HWHM only concentrates on the distribution of the defects, no deduction can be made regarding conversion ratio.

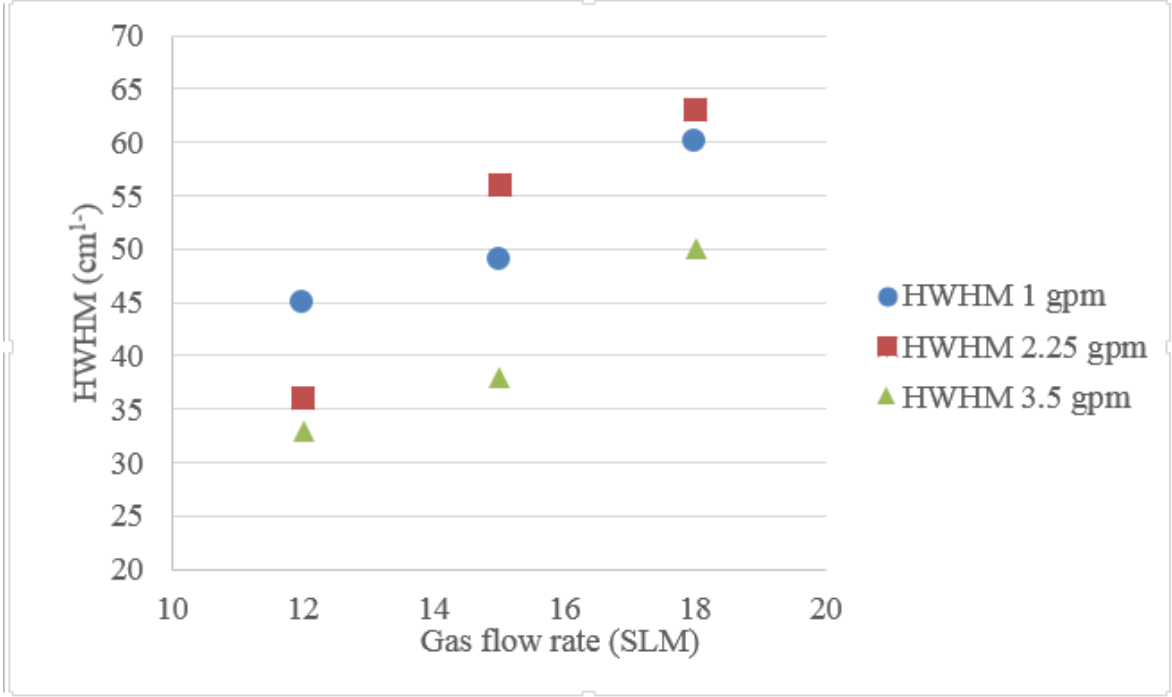

Figure 42. The HWHM vs Gas flow rate.

5.4 Discussion

The main objective of the project is to prove the use of 3-phase plasma reactor as a viable method for producing OLC. Additionally, the effect of two important parameters, the flow rate and carbon concentration, on the conversion efficiency was studied. Furthermore, calculating the residence time of the gas in the reactor is of importance. Since the quasi-2D model delivers the velocity by taking density, temperature, and geometry into account, the residence time of the experiments is calculated by using data attained by the model. As shown in Figure 19, depending on the operating conditions the gas temperature inside the reactor varies in the range of 2000 to 14000 K. Also, according to the ideal gas law the temperature of the gas directly affects the density which as a result reduces the gas velocity. Therefore, the length of the designated section of the reactor (see Figure 43) was divided over the average velocity to calculate the residence time attained by Figure 44. The selected section is

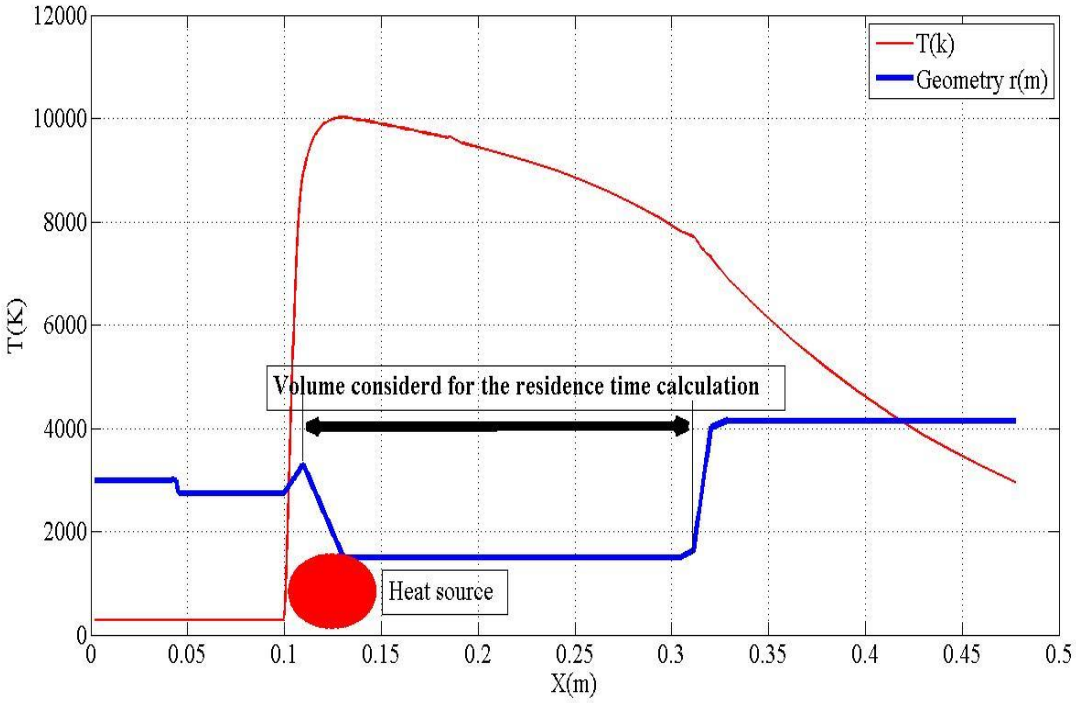

Figure 43. The selected section of the reactor for the calculation of the residence time

chosen since according to the literature the required temperature for the vaporization of the carbon is above 4000 K. Moreover, the visual observation through the viewports exhibited slightly green plasma which indicates carbon vaporization.

The estimated values for the residence time indicate the exposure time in the range of milliseconds. Although the exposure rate of the feedstock is drastically low, the data gathered by the characterization methods show promising results in terms of the conversion of the feedstock to the OLC. The values of the residence time implies that the rise in the gas flow rate increases the residence time as supported by the quasi-2D model.

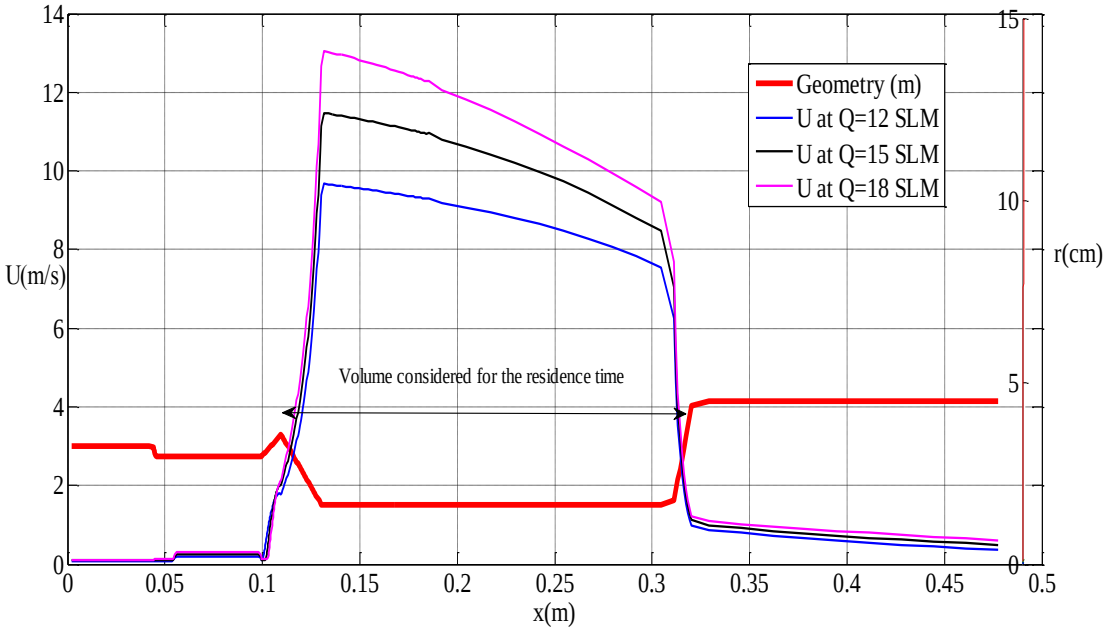

Figure 44.The velocity in 12, 15, and 18 SLM.

Table 9. The residence time in the selected section of the reactor.

Gas flow rate(SLM))	Residence time (millisecond)
12	23
15	20
18	18

The characterization data by the TGA suggests the conversion of the carbon black to the OLC by the 3-phase plasma with approximately 43% conversion at the longest residence time (23ms). Also, at the same conditions the conversion, according to the Raman spectroscopy in terms of I_G/I_D, was roughly 68%. Furthermore, the TEM images displayed a significant change in structure from amorphous carbon to the OLC. Although the product of the 3-phase plasma is not an ideal OLC, the conversion of the carbon observed in the TGA, Raman, and TEM provide useful information to optimize the 3-phase reactor design.

5.4.1 Plasma vs thermal annealing

In order to compare the efficiency of the plasma reactor design in terms of the utilized energy and the conversion of the carbon, an annealing test was performed on the N234 feedstock. The carbon was annealed in a furnace for one hour at 800℃. To furnace process at similar scale as the plasma units (1 to 3 gpm), the estimated power consumption was 200 watts. The TGA of this sample was taken in the same conditions as the samples heat by the 3-phase plasma (see Figure 45).

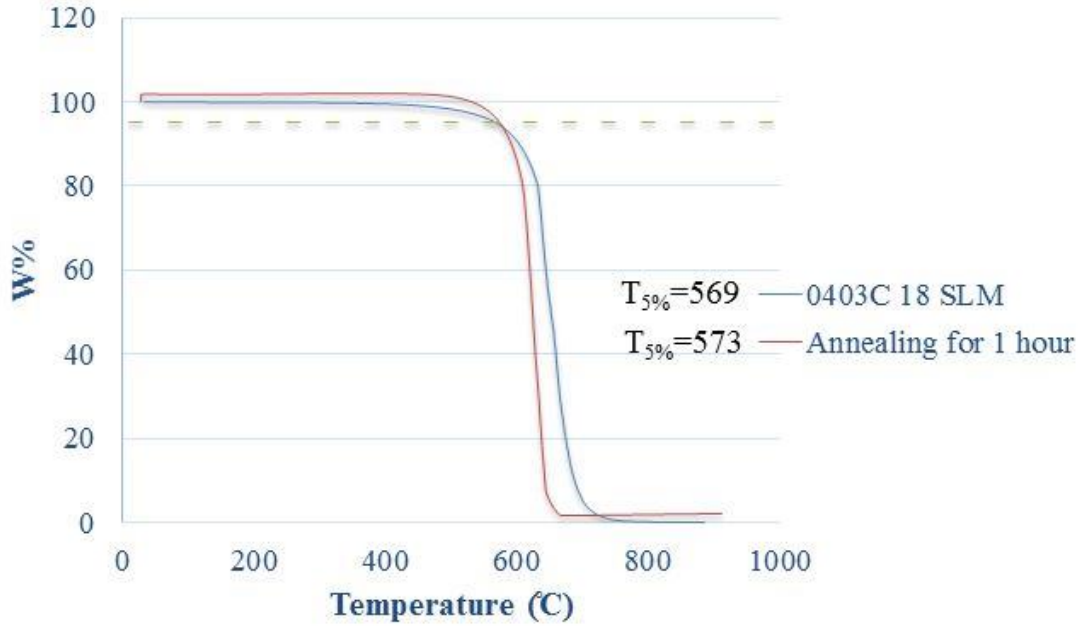

Figure 45. TGA of the annealing vs 18 SLM at 1 gpm.

The result were particularly interesting. The $\Delta T_{5\%}$ of the annealed samples was approximately 26℃ which is almost equivalent of the $\Delta T_{5\%}$ obtained from the lowest residence time (18ms) and 1 gpm carbon concentration. Although the conditions of both methods are significantly different, it appears the product carbons are similar according to the TGA. It should be noted that the OLC content of the furnace material may not be equivalent. Moreover, the amount of energy consumed for treating at similar feedstock rate is remarkably different. The estimated power consumption for furnace annealing is 720 kJ (200 W * 3600 s) verses plasma annealing 300 kJ (5000W * 60s), which represents >50% reduction in energy consumption. Additionally, the furnace method is a batch process which is poorly scalable wherein the plasma method operates in a continuous mode and can be scaled.

Chapter 6: Conclusion and Recommendations

In this study a new method of onion-like carbon production was developed and two relevant parameters were investigated. A 3-phase plasma reactor was modeled, designed, and constructed. Over 100 hours operating time confirmed the concept of the electrode design and operational stability. The range of the key design parameters and their effect on the temperature and the velocity of the gas were monitored by the quasi-2D model. The geometry of the reactor proved to be a key element in controlling the volume of the plasma and the residence time of the feedstock in the reactor.

The gas flow rate and carbon concentration were the variables of interest in the design of the experiment. Thermogravimetric analysis (TGA) and Raman spectroscopy were used to characterize feedstock, plasma carbon, and a reference OLC. A conversion ratio was determined by comparing results with the reference OLC. TGA testing indicates that at the lowest gas flow rate (12 SLM) and feed rate of 1 gpm, the conversion rate was 43%. Based on Raman spectroscopy under the same conditions the conversion ratio was measured at 68%. In addition, the TEM images revealed a considerable change in the structure of the amorphous carbon to OLC following the same trend as observed in TGA and Raman spectroscopy.

The result revealed that in the longer residence time the conversion rate was considerably increased. Also, changing the carbon concentration in the experiments showed that low carbon concentration is more favorable to the conversion of amorphous carbon to OLC. Furthermore, by applying certain assumptions the energy consumption of the 3-phase plasma was compared to a furnace annealing method. Although the nature of the furnace annealing and the plasma method are significantly

different, the resultant carbon were comparable. Remarkably however, the plasma method consumed 50% less energy compared to the annealing method. The requirement to lower manufacturing cost of OLC can be achieved by the scalable and efficient 3-phase plasma process.

6.1 Recommendations and Future work

According to the result presented in the previous chapter, the conversion rate at the highest residence time is approximately 43% (TGA) and 68% (Raman). Hence, in the next phase of the project it is worthwhile to investigate on optimizing the parameters, residence time and carbon concentration, to find the optimum range. The optimization can increase the conversion rate and lead the design to the final goal which is synthesis of OLC by using the 3-phase plasma. It is suggested that the future work focus on optimizing the parameters such as gas flow rate, carbon concentration, geometry, and power. Optimization can aid the project in gaining 100% conversion.

Changing the plasma gas from argon to helium can be beneficial since helium has better conductivity and provides higher temperature. Furthermore, the conversion of the different types of feedstocks by plasma treatment can be useful. Investigating the possibility of re-injecting the carbon feedstock and recycling the plasma gas can help lower cost. Although, it appears already that the plasma process is energy efficient, a more extensive study on the energy consumption is needed to validate overall production efficiency.

It may be useful to conduct OLC application research to relate properties such as morphology, particle size, purity, and cost as it effects performance. For example, how would the properties effect friction reduction and wear resistance in tribological applications.

References

[1] H. W. Kroto, J. R. Heath, S. C. O'Brien, R. F. Curl, and R. E. Smalley, "C60: Buckminsterfullerene," *Nature,* vol. 318, pp. 162-163, 1985.

[2] J. Gonzalez-Aguilar, M. Moreno, and L. Fulcheri, "Carbon nanostructures production by gas-phase plasma processes at atmospheric pressure," *Journal of Physics D: Applied Physics,* vol. 40, p. 2361, 2007.

[3] R. Haufler, J. Conceicao, L. Chibante, Y. Chai, N. Byrne, S. Flanagan, *et al.*, "Efficient production of C60 (buckminsterfullerene), C60H36, and the solvated buckide ion," *Journal of Physical Chemistry,* vol. 94, pp. 8634-8636, 1990.

[4] J. Bartelmess and S. Giordani, "Carbon nano-onions (multi-layer fullerenes): chemistry and applications," *Beilstein journal of nanotechnology,* vol. 5, pp. 1980-1998, 2014.

[5] N. Matsumoto, L. Joly-Pottuz, H. Kinoshita, and N. Ohmae, "Application of onion-like carbon to micro and nanotribology," *Diamond and related materials,* vol. 16, pp. 1227-1230, 2007.

[6] J. K. McDonough, A. I. Frolov, V. Presser, J. Niu, C. H. Miller, T. Ubieto, *et al.*, "Influence of the structure of carbon onions on their electrochemical performance in supercapacitor electrodes," *Carbon,* vol. 50, pp. 3298-3309, 2012.

[7] B.-s. Xu, "Prospects and research progress in nano onion-like fullerenes," *New carbon materials,* vol. 23, pp. 289-301, 2008.

[8] D. Ugarte, "Curling and closure of graphitic networks under electron-beam irradiation," *Nature,* vol. 359, p. 707, 1992.

[9] B. Yadav and R. Kumar, "Structure, properties and applications of fullerenes," *International Journal of Nanotechnology and Applications,* vol. 2, pp. 15-24, 2008.

[10] L. Joly-Pottuz, N. Matsumoto, H. Kinoshita, B. Vacher, M. Belin, G. Montagnac, *et al.,* "Diamond-derived carbon onions as lubricant additives," *Tribology International,* vol. 41, pp. 69-78, 2008.

[11] G. Lee, S. Huh, J. Jeong, and H.-C. Ri, "Excellent magnetic properties of fullerene encapsulated ferromagnetic nanoclusters," *Journal of magnetism and magnetic materials,* vol. 246, pp. 404-411, 2002.

[12] A.-y. Ge, B.-s. Xu, X.-m. Wang, T.-b. Li, P. Han, and X.-g. Liu, "Study on electromagnetic property of nano onion-like fullerenes," *ACTA PHYSICOCHIMICA SINICA,* vol. 22, p. 203, 2006.

[13] C. Portet, G. Yushin, and Y. Gogotsi, "Electrochemical performance of carbon onions, nanodiamonds, carbon black and multiwalled nanotubes in electrical double layer capacitors," *Carbon,* vol. 45, pp. 2511-2518, 2007.

[14] M. Bystrzejewski, M. Rummeli, T. Gemming, H. Lange, and A. Huczko, "Catalyst-free synthesis of onion-like carbon nanoparticles," *New carbon materials,* vol. 25, pp. 1-8, 2010.

[15] M. K. Sreeramoju, "Preparation, characterization and applications of functionalized carbon nano-onions," 2013.

[16] Q. Zou, M. Wang, Y. Li, Y. Zhao, and L. Zou, "Fabrication of onion-like carbon from nanodiamond by annealing," *Science in China Series E: Technological Sciences,* vol. 52, pp. 3683-3689, 2009.

[17] B. Xu and S. Tanaka, "Pt cluster bonding and fullerene formation in HRTEM," in *Proc Int Conf*, 1995.

[18] B. Xu and S.-I. Tanaka, "Multiple-nuclei onion-like fullerenes cultivated by electron beam irradiation," *BOOK-INSTITUTE OF MATERIALS*, vol. 687, pp. 619-624, 1998.

[19] B. Xu and S.-I. Tanaka, "Formation of giant onion-like fullerenes under Al nanoparticles by electron irradiation," *Acta Materialia*, vol. 46, pp. 5249-5257, 1998.

[20] Z. Sun, J. Shi, B. Tay, and S. Lau, "UV Raman characteristics of nanocrystalline diamond films with different grain size," *Diamond and related materials*, vol. 9, pp. 1979-1983, 2000.

[21] Y. Saito, T. Yoshikawa, M. Inagaki, M. Tomita, and T. Hayashi, "Growth and structure of graphitic tubules and polyhedral particles in arc-discharge," *Chemical Physics Letters*, vol. 204, pp. 277-282, 1993.

[22] D. Ugarte, "Onion-like graphitic particles," *Carbon*, vol. 33, pp. 989-993, 1995.

[23] C. Ruan and Y. Lian, "Purification of carbon nano-onions fabricated by arc discharge," *Fullerenes, Nanotubes and Carbon Nanostructures*, vol. 23, pp. 488-493, 2015.

[24] T. Oku, I. Narita, and A. Nishiwaki, "Formation, atomic structural optimization and electronic structures of tetrahedral carbon onion," *Diamond and related materials*, vol. 13, pp. 1337-1341, 2004.

[25] T. W. Zerda and T. Gruber, "Raman study of kinetics of graphitization of carbon blacks," *Rubber chemistry and technology*, vol. 73, pp. 284-292, 2000.

[26] J. P. Selegue, M. K. Sreeramoju, R. Borgohain, and J. D. Craddock, "Carbon Nano-onions from arc discharge and nanodiamond graphitization: comparison of their properties and chemistry." 2010

[27] O. Shenderova, C. Jones, V. Borjanovic, S. Hens, G. Cunningham, S. Moseenkov, *et al.*, "Detonation nanodiamond and onion-like carbon: applications in composites," *physica status solidi (a),* vol. 205, pp. 2245-2251, 2008.

[28] L. Fulcheri, F. Fabry, and V. Rohani, "The influence of the carbon precursor, carbon feed rate and helium gas flow rate on the synthesis of fullerenes from carbon powder in an entrained flow 3-phase AC plasma reactor operating at atmospheric pressure," *Carbon,* vol. 50, pp. 4524-4533, 2012.

[29] M. Hamady, D. Sheppard, K. Seddighi, A. Sarawagi, B. Scott, K. Wilcox, *et al.*, "Synthesis of Nanocarbons Using a Large Volume AC Plasma Reactor," in *MRS Proceedings*, 2015, pp. mrsf14-1747-hh08-06.

[30] P. G. Rutberg, A. Safronov, A. Surov, and S. Popov, "Alternating Current Electric Arc Plasma Generators1," 2007.

[31] R. Fitzpatrick, "Introduction to Plasma Physics: A graduate level course," *Lulu. com,* 2006.

[32] B. Ravary, L. Fulcheri, J. A. Bakken, G. Flamant, and F. Fabry, "Influence of the electromagnetic forces on momentum and heat transfer in a 3-phase AC plasma reactor," *Plasma Chemistry and Plasma Processing,* vol. 19, pp. 69-89, 1999.

[33] M. Boulos, P. Fauchais, and E. Pfender, "Thermal plasmas: Fundamentals and Applications vol. 1 Plenum," *New York ISBN,* vol. 306446073, 1994.

[34] L. Fulcheri, F. Fabry, S. Takali, and V. Rohani, "Three-phase AC arc plasma systems: a review," *Plasma Chemistry and Plasma Processing*, vol. 35, pp. 565-585, 2015.

[35] O. P. Solonenko, *Thermal plasma torches and technologies* vol. 1: Cambridge Int Science Publishing, 2000.

[36] C. Rehmet, F. Fabry, V. Rohani, F. Cauneau, and L. Fulcheri, "A Comparison Between MHD Modeling and Experimental Results in a 3-Phase AC Arc Plasma Torch: Influence of the Electrode Tip Geometry," *Plasma Chemistry and Plasma Processing*, vol. 34, pp. 975-996, 2014.

[37] P. Rutberg, *Physics and technology of high current discharges in dense gas media and flows*: Nova Science Publ., 2009.

[38] J. L Marqués, G. Forster, and J. Schein, "Multi-electrode plasma torches: motivation for development and current state-of-the-art," *The Open Plasma Physics Journal*, vol. 2, 2009.

[39] S. Farhat and C. D. Scott, "Review of the arc process modeling for fullerene and nanotube production," *Journal of nanoscience and nanotechnology*, vol. 6, pp. 1189-1210, 2006.

[40] P. P. Kuzhir, A. G. Paddubskaya, S. A. Maksimenko, V. L. Kuznetsov, S. Moseenkov, A. I. Romanenko, *et al.*, "Carbon onion composites for EMC applications," *IEEE Transactions on Electromagnetic Compatibility*, vol. 54, pp. 6-16, 2012.

[41] F. Moreau, R. Langlet, P. Lambin, P. Kuzhir, D. Bychanok, and S. Maksimenko, "Onion-like-carbon-based composite films: Theoretical modeling of electromagnetic response," *Solid State Sciences*, vol. 11, pp. 1752-1756, 2009.

[42] G. Barbezat and K. Landes, "Plasma Torch-System Triplex: Increased Production and a More Stable Process. A new plasma-torch system with three cathodes produced very promising results during tests conducted in the industrial environment," *Sulzer Technical Review*, pp. 32-35, 1999.

[43] F. Fabry, G. Flamant, and L. Fulcheri, "Carbon black processing by thermal plasma. Analysis of the particle formation mechanism," *Chemical Engineering Science,* vol. 56, pp. 2123-2132, 2001.

[44] L. Fulcheri, Y. Schwob, F. Fabry, G. Flamant, L. Chibante, and D. Laplaze, "Fullerene production in a 3-phase AC plasma process," *Carbon,* vol. 38, pp. 797-803, 2000.

[45] L. Chibante, A. Thess, J. Alford, M. Diener, and R. Smalley, "Solar generation of the fullerenes," *The Journal of Physical Chemistry,* vol. 97, pp. 8696-8700, 1993.

[46] J.-B. Donnet, *Carbon black: science and technology*: CRC Press, 1993.

[47] C. Wang, T. Imahori, Y. Tanaka, T. Sakuta, H. Takikawa, and H. Matsuo, "Synthesis of fullerenes from carbon powder by using high power induction thermal plasma," *Thin Solid Films,* vol. 390, pp. 31-36, 2001.

[48] C. Wang, T. Imahori, Y. Tanaka, T. Sakuta, H. Takikawa, and H. Matsuo, "Silicon inclusion effect on fullerene formation under induction thermal plasma condition," *Thin Solid Films,* vol. 407, pp. 72-78, 2002.

[49] J.-F. Bilodeau, T. Alexakis, J.-L. Meunier, and P. G. Tzantrizos, "Model of the synthesis of fullerenes by the plasma torch dissociation of," *Journal of Physics D: Applied Physics,* vol. 30, p. 2403, 1997.

[50] M. Zhao, H. Song, X. Chen, and W. Lian, "Large-scale synthesis of onion-like carbon nanoparticles by carbonization of phenolic resin," *Acta Materialia,* vol. 55, pp. 6144-6150, 2007.

[51] Y. Schwob, F. Fischer, L. Fulcheri, and P. Willemez, "Conversion of carbon or carbonated compounds in a plasma," *Patent WO,* vol. 9, 1994.

[52] H. Murayama, S. Tomonoh, J. M. Alford, and M. E. Karpuk, "Fullerene production in tons and more: from science to industry," *Fullerenes, Nanotubes and Carbon Nanostructures,* vol. 12, pp. 1-9, 2005.

[53] T. Guo, P. Nikolaev, A. Thess, D. T. Colbert, and R. E. Smalley, "Catalytic growth of single-walled manotubes by laser vaporization," *Chemical physics letters,* vol. 243, pp. 49-54, 1995.

[54] M. Hamady, D. Sheppard, K. Seddighi, A. Sarawagi, B. Scott, K. Wilcox, *et al.*, "Synthesis of Nanocarbons Using a Large Volume AC Plasma Reactor," *MRS Online Proceedings Library Archive,* vol. 1747, 2015.

[55] A. G. Kevin Wilcox "Quasi 2D-Model for 3-phase Plasma Reactor," UNB, UNB2014.

[56] H. Beisswenger, G. Daradimos, M. Hirsch, L. Plass, and H. Serbent, "Method of producing fuel gas and process heat fron carbonaceous materials," ed: Google Patents, 1984.

[57] J. R. van Ommen, J. M. Valverde, and R. Pfeffer, "Fluidization of nanopowders: a review," *Journal of Nanoparticle Research,* vol. 14, p. 737, 2012.

[58] Y. Iwadate and M. Horio, "Prediction of agglomerate sizes in bubbling fluidized beds of group C powders," *Powder Technology,* vol. 100, pp. 223-236, 1998.

[59] X. Zhu, Q. Zhang, Y. Wang, and F. Wei, "Review on the nanoparticle fluidization science and technology," *Chinese Journal of Chemical Engineering*, vol. 24, pp. 9-22, 2016.

[60] G. Astarita, "Forces acting on particles in a fluidized bed," *Chemical engineering science*, vol. 48, pp. 3438-3440, 1993.

[61] H. K. Versteeg and W. Malalasekera, *An introduction to computational fluid dynamics: the finite volume method*: Pearson Education, 2007.

[62] J. Peiró and S. Sherwin, "Finite difference, finite element and finite volume methods for partial differential equations," *Handbook of materials modeling*, pp. 2415-2446, 2005.

[63] F. Ghirelli and B. Leckner, "Transport equation for the local residence time of a fluid," *Chemical engineering science*, vol. 59, pp. 513-523, 2004.

[64] A. N. Brooks and T. J. Hughes, "Streamline upwind/Petrov-Galerkin formulations for convection dominated flows with particular emphasis on the incompressible Navier-Stokes equations," *Computer methods in applied mechanics and engineering*, vol. 32, pp. 199-259, 1982.

[65] J. Droniou, "Discretizations of convection terms in Hybrid Mimetic Mixed methods."

[66] S. E. Rogers and D. Kwak, "Upwind differencing scheme for the time-accurate incompressible Navier-Stokes equations," *AIAA journal*, vol. 28, pp. 253-262, 1990.

[67] N. Ashgriz and J. Mostaghimi, "An introduction to computational fluid dynamics," *Fluid flow handbook. McGraw-Hill Professional*, 2002.

[68] M. Farhloul and A. S. Mounim, "A mixed-hybrid finite element method for convection–diffusion problems," *Applied mathematics and computation*, vol. 171, pp. 1037-1047, 2005.

[69] K. S. Drellishak, C. Knopp, and A. B. Cambel, "Partition functions and thermodynamic properties of argon plasma," *The Physics of fluids*, vol. 6, pp. 1280-1288, 1963.

[70] K. Eisazadeh-Far, H. Metghalchi, and J. C. Keck, "Thermodynamic Properties of Ionized Gases at High Temperatures," *Journal of Energy Resources Technology*, vol. 133, p. 022201, 2011.

[71] G. Dunn and T. Eagar, *Calculation of electrical and thermal conductivities of metallurgical plasmas*: Citeseer, 1990.

[72] J. H. Lee, "Recycling study for the production of fullerene," University of Newbrunswick, 2017.

[73] P. G. Rutberg, V. A. Kuznetsov, E. O. Serba, S. D. Popov, A. V. Surov, G. V. Nakonechny, *et al.*, "Novel three-phase steam–air plasma torch for gasification of high-caloric waste," *Applied energy*, vol. 108, pp. 505-514, 2013.

[74] *Tekna Nanopowder*. Available: Retrieved from http://tekna.com/equipment-spheroidization-nanosynthesis-deposition/related-products/precursor-feeders/pfr-nanopowder-feeder/. Update 2015.

[75] C. Zhang, J. Li, C. Shi, E. Liu, X. Du, W. Feng, *et al.*, "The efficient synthesis of carbon nano-onions using chemical vapor deposition on an unsupported Ni–Fe alloy catalyst," *Carbon*, vol. 49, pp. 1151-1158, 2011.

[76] L. S. Pang, J. D. Saxby, and S. P. Chatfield, "Thermogravimetric analysis of carbon nanotubes and nanoparticles," *The Journal of Physical Chemistry,* vol. 97, pp. 6941-6942, 1993.

[77] M. Szerencsi and G. Radnoczi, "The mechanism of growth and decay of carbon nano-onions formed by ordering of amorphous particles," *Vacuum,* vol. 84, pp. 197-201, 2009.

[78] T. Gruber, T. W. Zerda, and M. Gerspacher, "Raman studies of heat-treated carbon blacks," *Carbon,* vol. 32, pp. 1377-1382, 1994.

[79] A. Jorio, M. Pimenta, A. Souza Filho, R. Saito, G. Dresselhaus, and M. Dresselhaus, "Characterizing carbon nanotube samples with resonance Raman scattering," *New Journal of Physics,* vol. 5, p. 139, 2003.

[80] P. Mallet-Ladeira, P. Puech, C. Toulouse, M. Cazayous, N. Ratel-Ramond, P. Weisbecker, *et al.*, "A Raman study to obtain crystallite size of carbon materials: A better alternative to the Tuinstra–Koenig law," *Carbon,* vol. 80, pp. 629-639, 2014.

Appendix 1: Table of properties of argon for the quasi-2D model up to 24000 K

Temperature	Density	Enthalpy	Cp	K
10	5.0161	55400	542.9	0.0044691
15	3.2727	82200	529.61	0.00468865
20	2.4401	109000	525.08	0.0049082
25	1.9481	135000	522.95	0.00512775
30	1.6221	161000	521.78	0.0053473
35	1.3901	187000	521.08	0.00556685
40	1.2162	213000	520.62	0.0057864
45	1.0812	239000	520.31	0.00600595
50	0.97316	265000	520.1	0.0062255
55	0.88479	291000	519.94	0.00644505
60	0.81116	317000	519.82	0.0066646
65	0.74885	343000	519.72	0.00688415
70	0.69544	369000	519.65	0.0071037
75	0.64915	395000	519.6	0.00732325
80	0.60864	421000	519.55	0.0075428
85	0.57289	447000	519.51	0.00776235
90	0.5411	473000	519.48	0.0079819
95	0.51267	499000	519.46	0.00820145
100	0.48707	525000	519.44	0.008421
105	0.4639	551000	519.42	0.00864055
110	0.44285	577000	519.4	0.0088601
115	0.42362	603000	519.39	0.00907965
120	0.40599	629000	519.38	0.0092992
125	0.38977	655000	519.37	0.00951875
130	0.37479	681000	519.36	0.0097383
135	0.36093	707000	519.35	0.00995785
140	0.34805	733000	519.35	0.0101774
145	0.33606	759000	519.34	0.01039695
150	0.32487	784000	519.34	0.0106165
155	0.3144	810000	519.33	0.01083605
160	0.30459	836000	519.33	0.0110556
165	0.29537	862000	519.33	0.01127515
170	0.28669	888000	519.32	0.0114947
175	0.2785	914000	519.32	0.01171425
180	0.27077	940000	519.32	0.0119338
185	0.26346	966000	519.32	0.01215335
190	0.25653	992000	519.31	0.0123729
195	0.24996	1020000	519.31	0.01259245
200	0.24372	1040000	519.31	0.012812
205	0.23778	1070000	519.31	0.01303155
210	0.23212	1100000	519.31	0.0132511
215	0.22673	1120000	519.31	0.01347065

220	0.22158	1150000	519.31	0.0136902
225	0.21666	1170000	519.31	0.01390975
230	0.21195	1200000	519.31	0.0141293
235	0.20744	1230000	519.3	0.01434885
240	0.20312	1250000	519.3	0.0145684
245	0.19898	1280000	519.3	0.01478795
250	0.19501	1300000	519.3	0.0150075
255	0.19118	1330000	519.3	0.01522705
260	0.18751	1360000	519.3	0.0154466
265	0.18397	1380000	519.3	0.01566615
270	0.18057	1410000	519.3	0.0158857
275	0.17729	1430000	519.3	0.01610525
280	0.17412	1460000	519.3	0.0163248
285	0.17107	1490000	519.3	0.01654435
290	0.16812	1510000	519.3	0.0167639
295	0.16527	1540000	519.3	0.01698345
300	0.16252	1560000	519.3	0.017203
305	0.15986	1590000	519.3	0.01742255
310	0.15728	1620000	519.3	0.0176421
315	0.15479	1640000	519.3	0.01786165
320	0.15237	1670000	519.3	0.0180812
325	0.15003	1690000	519.3	0.01830075
330	0.14775	1720000	519.3	0.0185203
335	0.14555	1750000	519.3	0.01873985
340	0.14341	1770000	519.3	0.0189594
345	0.14133	1800000	519.3	0.01917895
350	0.13931	1820000	519.3	0.0193985
355	0.13735	1850000	519.3	0.01961805
360	0.13545	1880000	519.3	0.0198376
365	0.13359	1900000	519.3	0.02005715
370	0.13179	1930000	519.3	0.0202767
375	0.13003	1950000	519.3	0.02049625
380	0.12832	1980000	519.3	0.0207158
385	0.12665	2000000	519.3	0.02093535
390	0.12503	2030000	519.3	0.0211549
395	0.12345	2060000	519.3	0.02137445
400	0.12191	2080000	519.3	0.021594
405	0.1204	2110000	519.3	0.02181355
410	0.11893	2130000	519.3	0.0220331
415	0.1175	2160000	519.3	0.02225265
420	0.1161	2190000	519.3	0.0224722
425	0.11474	2210000	519.3	0.02269175
430	0.1134	2240000	519.3	0.0229113
435	0.1121	2260000	519.3	0.02313085
440	0.11083	2290000	519.3	0.0233504
445	0.10958	2320000	519.3	0.02356995

450	0.10837	2340000	519.3	0.0237895
455	0.10718	2370000	519.3	0.02400905
460	0.10601	2390000	519.3	0.0242286
465	0.10487	2420000	519.3	0.02444815
470	0.10376	2450000	519.3	0.0246677
475	0.10266	2470000	519.3	0.02488725
480	0.1016	2500000	519.3	0.0251068
485	0.10055	2520000	519.3	0.02532635
490	0.099523	2550000	519.3	0.0255459
495	0.098518	2580000	519.3	0.02576545
500	0.097533	2600000	519.3	0.025985
600	0.081297	3120000	519.31	0.030376
700	0.069683	3640000	519.31	0.034767
800	0.060973	4160000	519.31	0.039158
900	0.054198	4680000	519.31	0.043549
1000	0.048778	5200000	519.31	0.04794
1100	0.044344	5720000	519.31	0.052331
1200	0.040649	6240000	519.31	0.056722
1300	0.037522	6760000	519.31	0.061113
1400	0.034842	7280000	519.31	0.065504
1500	0.032519	7800000	519.31	0.069895
1600	0.030486	8310000	519.31	0.074286
1700	0.028693	8830000	519.31	0.078677
1800	0.027099	9350000	519.31	0.083068
1900	0.025673	9870000	519.31	0.087459
2000	0.024389	10400000	519.31	0.09185
2100	0.023228	10900000	519.31	0.096241
2200	0.022172	11400000	519.31	0.100632
2300	0.021208	12000000	519.31	0.105023
2400	0.020324	12500000	519.31	0.109414
2500	0.019511	13000000	519.31	0.113805
2600	0.018761	13500000	519.31	0.118196
2700	0.018066	14000000	519.31	0.122587
2800	0.017421	14500000	519.31	0.126978
2900	0.01682	15100000	519.31	0.131369
3000	0.016259	15600000	519.31	0.13576
3100	0.015735	16100000	519.31	0.140151
3200	0.015243	16600000	519.31	0.144542
3300	0.014781	17100000	519.31	0.148933
3400	0.014347	17700000	519.31	0.153324
3500	0.013937	18200000	519.31	0.157715
3600	0.01355	18700000	519.31	0.162106
3700	0.013183	19200000	519.31	0.166497
3800	0.012836	19700000	519.31	0.170888
3900	0.012507	20300000	519.31	0.175279
4000	0.012195	20800000	519.31	0.17967

4100	0.011897	21300000	519.31	0.184061
4200	0.011614	21800000	519.31	0.188452
4300	0.011344	22300000	519.31	0.192843
4400	0.011086	22900000	519.31	0.197234
4500	0.01084	23400000	519.31	0.201625
4600	0.010604	23900000	519.31	0.206016
4700	0.010378	24400000	519.31	0.210407
4800	0.010162	24900000	519.31	0.214798
4900	0.009955	25500000	519.31	0.219189
5000	0.009756	25900000	519.31	0.22358
5100	0.009564	26500000	519.31	0.227971
5200	0.009381	27100000	519.31	0.232362
5300	0.009204	27600000	519.31	0.236753
5400	0.009033	28200000	519.31	0.241144
5500	0.008869	28700000	519.31	0.245535
5600	0.00871	29200000	519.31	0.249926
5700	0.008558	29800000	519.31	0.254317
5800	0.00841	30300000	519.31	0.258708
5900	0.008268	30800000	519.31	0.263099
6000	0.00813	31300000	519.31	0.26749
6100	0.007997	31800000	519.31	0.271881
6200	0.007868	32300000	519.31	0.276272
6300	0.007743	32900000	519.31	0.280663
6400	0.007622	33400000	519.31	0.285054
6500	0.007504	33900000	519.31	0.289445
6600	0.007391	34400000	535.55	0.293836
6700	0.00728	35000000	543.91	0.298227
6800	0.007173	35500000	556.47	0.302618
6900	0.007069	36100000	569.02	0.307009
7000	0.006968	36600000	585.75	0.3114
7100	0.00687	37200000	606.67	0.315791
7200	0.006775	37900000	627.59	0.324249571
7300	0.006682	38500000	652.7	0.336591267
7400	0.006592	39200000	677.807	0.34930725
7500	0.006504	39800000	652.807	0.362404578
7600	0.006418	40500000	677.807	0.37589026
7700	0.006335	41200000	715.46	0.389771239
7800	0.006254	41900000	757.3	0.404054389
7900	0.006175	42700000	803.32	0.418746498
8000	0.006052	43600000	857.71	0.433854263
8100	0.006022	44400000	916.29	0.449384274
8200	0.005949	45400000	983.23	0.465343008
8300	0.005877	46400000	1050.18	0.481736814
8400	0.005807	47400000	1129.67	0.498571902
8500	0.005739	48600000	1133.86	0.515854335
8600	0.005672	49800000	1221.76	0.533590011

8700	0.005607	51100000	1322.14	0.551784653
8800	0.005543	52500000	1430.92	0.570443801
8900	0.005481	53900000	1548.07	0.589572792
9000	0.00542	55600000	1677.782	0.609176755
9100	0.00536	57300000	1820.03	0.62926059
9200	0.005302	59200000	1970.66	0.649828964
9300	0.005245	61300000	2133.83	0.670886289
9400	0.005189	63500000	2305.38	0.692436718
9500	0.004936	65900000	2485.29	0.714484124
9600	0.004863	68500000	2681.94	0.737032091
9700	0.00479	71300000	2891.14	0.7600839
9800	0.004717	74300000	3112.89	0.783642516
9900	0.004643	77500000	3347.19	0.807710573
10000	0.004569	81000000	3594.05	0.832290363
10100	0.004494	84700000	3857.64	0.857383823
10200	0.004418	88700000	4129.6	0.882992521
10300	0.004342	93000000	4418.29	0.909117643
10400	0.004265	97600000	4723.73	0.935759981
10500	0.004188	1.03E+08	5439.19	0.96291992
10600	0.00411	1.08E+08	5773.91	0.990597425
10700	0.004031	1.14E+08	6066.79	1.018792031
10800	0.003952	1.21E+08	6401.51	1.047502829
10900	0.003872	1.27E+08	6736.23	1.076728456
11000	0.003792	1.34E+08	7070.95	1.106467083
11100	0.004712	1.41E+08	7405.67	1.136716401
11200	0.003631	1.49E+08	7740.39	1.167473618
11300	0.003551	1.57E+11	8075.11	1.19873544
11400	0.00347	1.65E+08	8409.83	1.230498068
11500	0.00339	1.74E+08	9455.82	1.262757183
11600	0.00331	1.83E+08	9790.54	1.295507943
11700	0.003232	1.93E+08	10125.26	1.328744971
11800	0.003153	2.04E+08	10376.3	1.362462344
11900	0.003076	2.14E+08	10627.34	1.396653594
12000	0.003	2.25E+08	10878.38	1.431311694
12100	0.002926	2.36E+08	11087.58	1.466429053
12200	0.002853	2.47E+08	11254.94	1.501997516
12300	0.002782	2.58E+08	11380.46	1.538008349
12400	0.002713	2.7E+08	11505.98	1.574452246
12500	0.002646	2.81E+08	11589.66	1.611319316
12600	0.002582	2.92E+08	11631.5	1.648599087
12700	0.00252	3.04E+08	11631.5	1.686280497
12800	0.002461	3.16E+08	11631.5	1.724351902
12900	0.002403	3.27E+08	11589.66	1.762801067
13000	0.002348	3.39E+08	11505.98	1.801615168
13100	0.002297	3.5E+08	11380.46	1.840780799
13200	0.002247	3.61E+08	11254.94	1.880283965

13300	0.002201	3.73E+08	11045.74	1.920110091
13400	0.002115	3.84E+08	10836.54	1.960244025
13500	0.002076	3.94E+08	9623.18	2.000670038
13600	0.002039	4.04E+08	9330.3	2.041371835
13700	0.002004	4.13E+08	8995.59	2.082332559
13800	0.001971	4.21E+08	8702.71	2.123534797
13900	0.00194	4.3E+08	8409.83	2.16496059
14000	0.00191	4.38E+08	8075.11	2.206591439
14100	0.001883	4.46E+08	7740.39	2.248408321
14200	0.001809	4.54E+08	7447.51	2.290391691
14300	0.001788	4.61E+08	7112.79	2.332521503
14400	0.001767	4.68E+08	6778.07	2.374777216
14500	0.001747	4.75E+08	5815.75	2.417137811
14600	0.001728	4.8E+08	5481.03	2.459581803
14700	0.00171	4.86E+08	5146.31	2.502087259
14800	0.001693	4.91E+08	4853.43	2.544631813
14900	0.001676	4.95E+08	4560.55	2.587192684
15000	0.00166	5E+08	4280.22	2.629746691
15100	0.001645	5.04E+08	4016.63	2.672270276
15200	0.00163	5.08E+08	3765.59	2.714739523
15300	0.001616	5.12E+08	3514.55	2.757130174
15400	0.001602	5.15E+08	3305.35	2.799417657
15500	0.001576	5.18E+08	3221.67	2.841577105
15600	0.001563	5.21E+08	3054.31	2.883583375
15700	0.001553	5.24E+08	2886.95	2.925411081
15800	0.001541	5.27E+08	2719.59	2.967034608
15900	0.001529	5.3E+08	2594.07	3.008428144
16000	0.001518	5.33E+08	2468.55	3.049565703
16100	0.001507	5.35E+08	2384.87	3.09042115
16200	0.001503	5.37E+08	2301.19	3.13096823
16300	0.001501	5.4E+08	2217.51	3.171180595
16400	0.0015	5.42E+08	2175.67	3.21103183
16500	0.001498	5.44E+08	2292.82	3.250495482
16600	0.001496	5.46E+08	2271.9	3.289545091
16700	0.001485	5.49E+08	2259.35	3.328154216
16800	0.001474	5.51E+08	2255.17	3.366296463
16900	0.001464	5.53E+08	2267.72	3.403945519
17000	0.001454	5.55E+08	2292.82	3.44107518
17100	0.001444	5.58E+08	2330.48	3.47765938
17200	0.001434	5.6E+08	2380.69	3.513672221
17300	0.001424	5.62E+08	2447.63	3.549088005
17400	0.001414	5.65E+08	2522.94	3.583881262
17500	0.001406	5.67E+08	2640.1	3.618026785
17600	0.001396	5.7E+08	2744.7	3.651499653
17700	0.001387	5.73E+08	2861.85	3.684275267
17800	0.001377	5.76E+08	2995.74	3.716329377

17900	0.001368	5.79E+08	3305.35	3.747638113
18000	0.001358	5.82E+08	3481.08	3.778178015
18100	0.001349	5.85E+08	3669.36	3.807926061
18200	0.001339	5.89E+08	3874.37	3.836859695
18300	0.00133	5.93E+08	4096.13	3.864956859
18400	0.00132	5.97E+08	4464.32	3.892196015
18500	0.001311	6.01E+08	4715.36	3.918556181
18600	0.001301	6.05E+08	4937.11	3.944016949
18700	0.001292	6.1E+08	5271.83	3.968558517
18800	0.001282	6.15E+08	5522.87	3.992161712
18900	0.001272	6.21E+08	5815.75	4.014808016
19000	0.001262	6.27E+08	5819.64	4.036479592
19100	0.001252	6.33E+08	6154.59	4.057159303
19200	0.001242	6.39E+08	6489.53	4.076830737
19300	0.001232	6.46E+08	6824.48	4.095478231
19400	0.001222	6.53E+08	7159.42	4.113086887
19500	0.001211	6.6E+08	7954.91	4.129642595
19600	0.001201	6.68E+08	8331.72	4.145132053
19700	0.00119	6.77E+08	8666.67	4.15954278
19800	0.001179	6.85E+08	9043.48	4.172863137
19900	0.001168	6.95E+08	9420.29	4.185082343
20000	0.001158	7.04E+08	9755.23	4.275743157
20100	0.001146	7.14E+08	10132.05	4.291981253
20200	0.001135	7.25E+08	10508.86	4.308199971
20300	0.001124	7.35E+08	10843.8	4.324399431
20400	0.001113	7.46E+08	11220.61	4.340579749
20500	0.001101	7.58E+08	12057.97	4.356741044
20600	0.00109	7.7E+08	12392.92	4.372883428
20700	0.001079	7.82E+08	12727.86	4.389007017
20800	0.001067	7.95E+08	13020.94	4.405111923
20900	0.001056	8.08E+08	13314.01	4.421198257
21000	0.001044	8.22E+08	13565.22	4.437266129
21100	0.001033	8.36E+08	13816.43	4.453315648
21200	0.001022	8.49E+08	14025.77	4.469346922
21300	0.00101	8.64E+08	14235.11	4.485360057
21400	0.000999	8.78E+08	14402.58	4.50135516
21500	0.000988	8.92E+08	14653.79	4.517332334
21600	0.000977	9.07E+08	14779.39	4.533291683
21700	0.000966	9.22E+08	14863.13	4.54923331
21800	0.000955	9.37E+08	15030.6	4.565157314
21900	0.000945	9.51E+08	15072.47	4.581063797
22000	0.000934	9.67E+08	15072.47	4.596952858
22100	0.000924	9.82E+08	15030.6	4.612824595
22200	0.000914	9.97E+08	15030.6	4.628679105
22300	0.000904	1.01E+09	14988.73	4.644516484
22400	0.000894	1.03E+09	14905	4.660336827

22500	0.000885	1.04E+09	14360.71	4.676140229
22600	0.000876	1.06E+09	14235.11	4.691926783
22700	0.000867	1.07E+09	14067.64	4.707696582
22800	0.000858	1.08E+09	13942.03	4.723449716
22900	0.000849	1.1E+09	13732.69	4.739186277
23000	0.000841	1.11E+09	13565.22	4.754906353
23100	0.000833	1.12E+09	13355.88	4.770610035
23200	0.000825	1.14E+09	13146.54	4.78629741
23300	0.000817	1.15E+09	12937.2	4.801968564
23400	0.000809	1.16E+09	12685.99	4.817623585
23500	0.000802	1.18E+09	11974.24	4.833262558
23600	0.000795	1.19E+09	11681.16	4.848885567
23700	0.000788	1.2E+09	11429.95	4.864492696
23800	0.000781	1.21E+09	11178.75	4.880084028
23900	0.000775	1.22E+09	10885.67	4.895659646
24000	0.000768	1.23E+09	10634.46	4.911219632

Appendix 2: Machine drawings

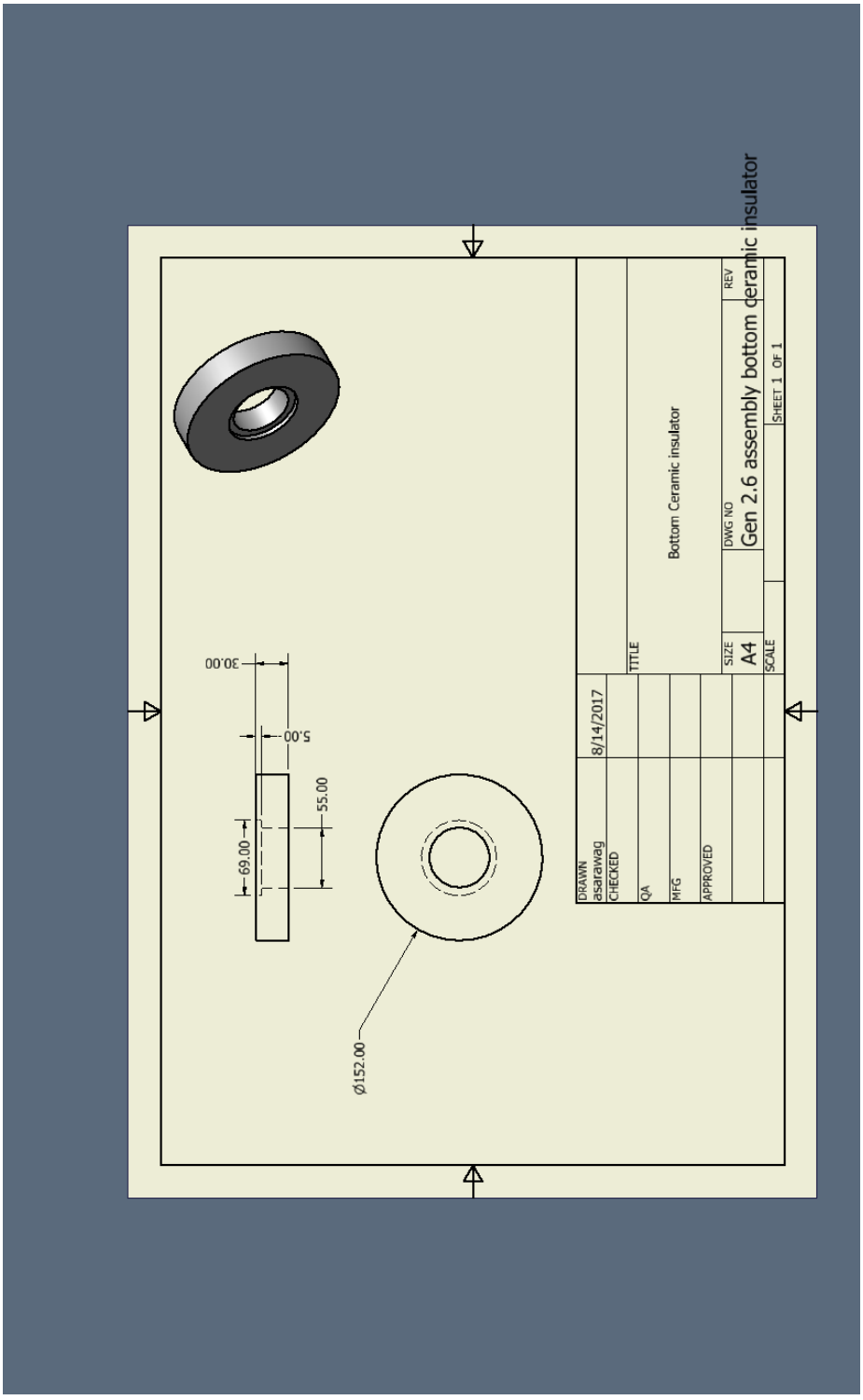

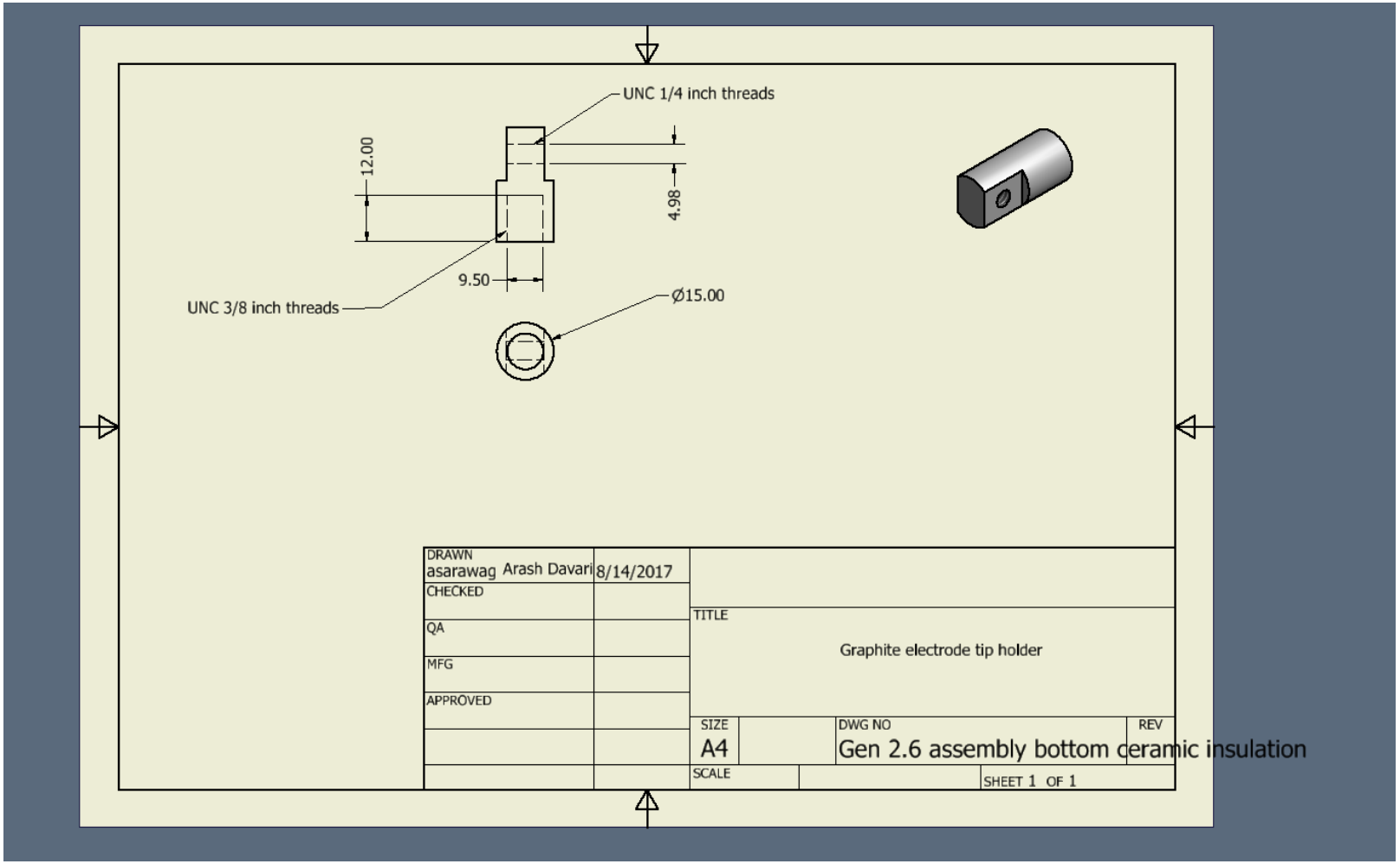
UNC 1/4 inch threads
12.00
4.98
9.50
UNC 3/8 inch threads
Ø15.00
DRAWN
asarawag Arash Davari
8/14/2017
CHECKED
QA
MFG
APPROVED
TITLE
Graphite electrode tip holder
SIZE
A4
DWG NO
Gen 2.6 assembly bottom ceramic insulation
REV
SCALE
SHEET 1 OF 1

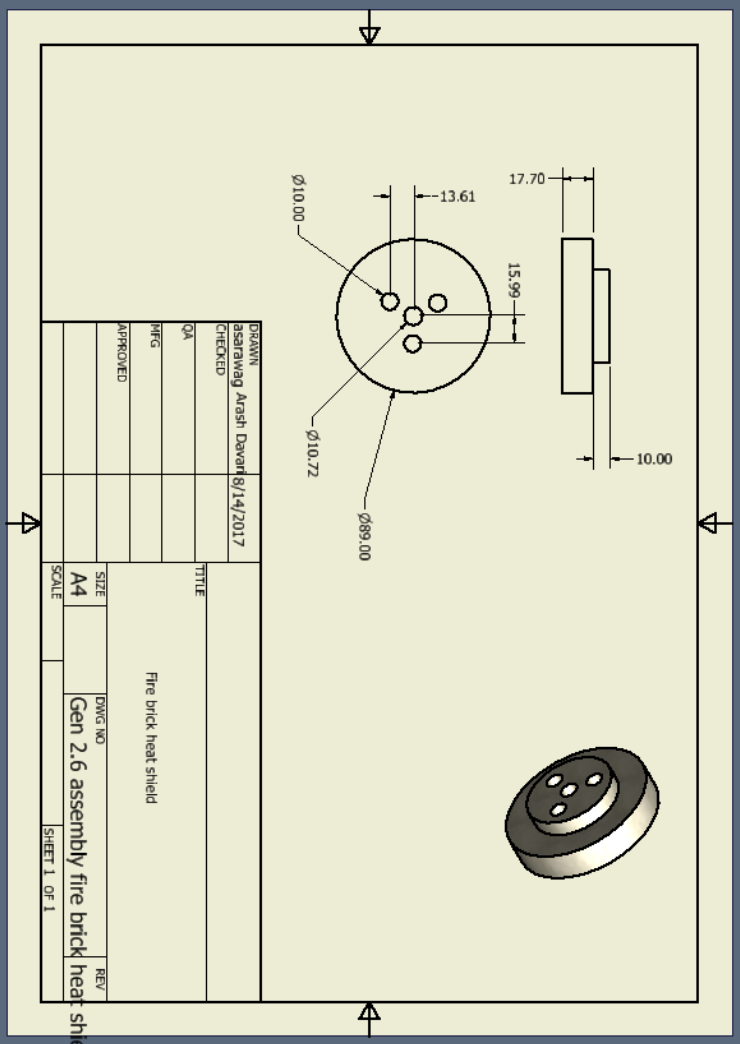
Ø10.00
13.61
17.70
15.99
Ø10.72
Ø89.00
10.00
DRAWN
asarawag Arash Dewan 8/14/2017
CHECKED
QA
MFG
APPROVED
SIZE
A4
SCALE
DWG NO
Gen 2.6 assembly fire brick heat shield
REV
SHEET 1 OF 1
TITLE
Fire brick heat shield

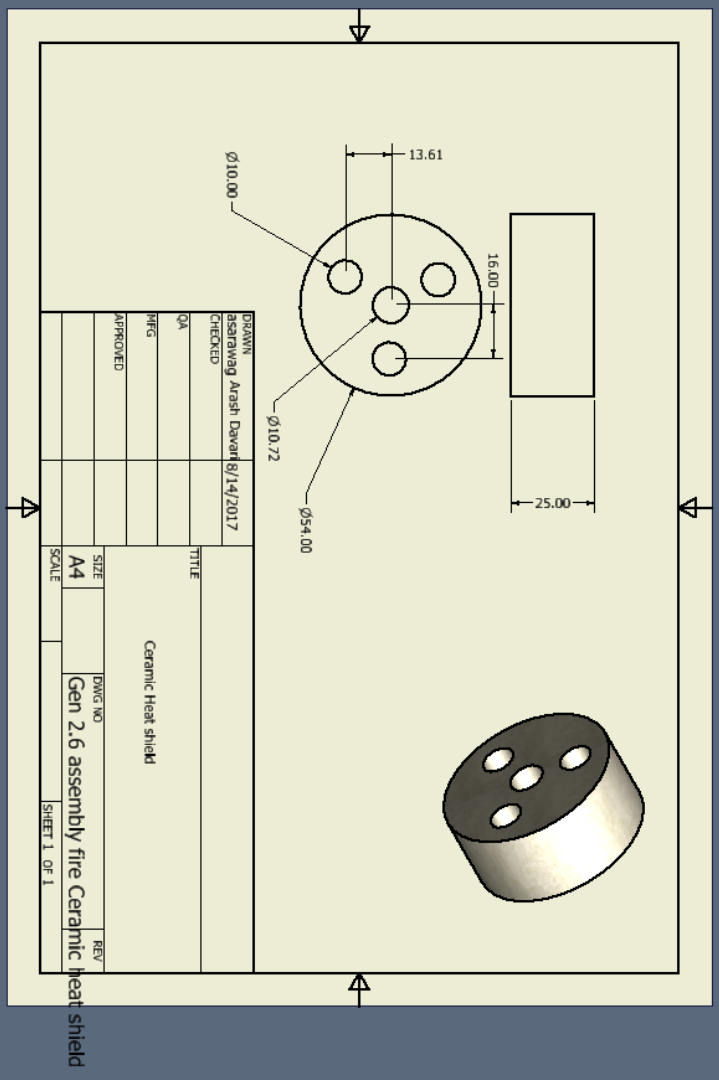
13.61
Ø10.00
16.00
Ø10.72
Ø54.00
25.00
DRAWN
asarawag Arash Davari 8/14/2017
CHECKED
QA
MFG
APPROVED
TITLE
Ceramic Heat shield
SIZE
A4
DWG NO
Gen 2.6 assembly fire Ceramic heat shield
REV
SCALE
SHEET 1 OF 1

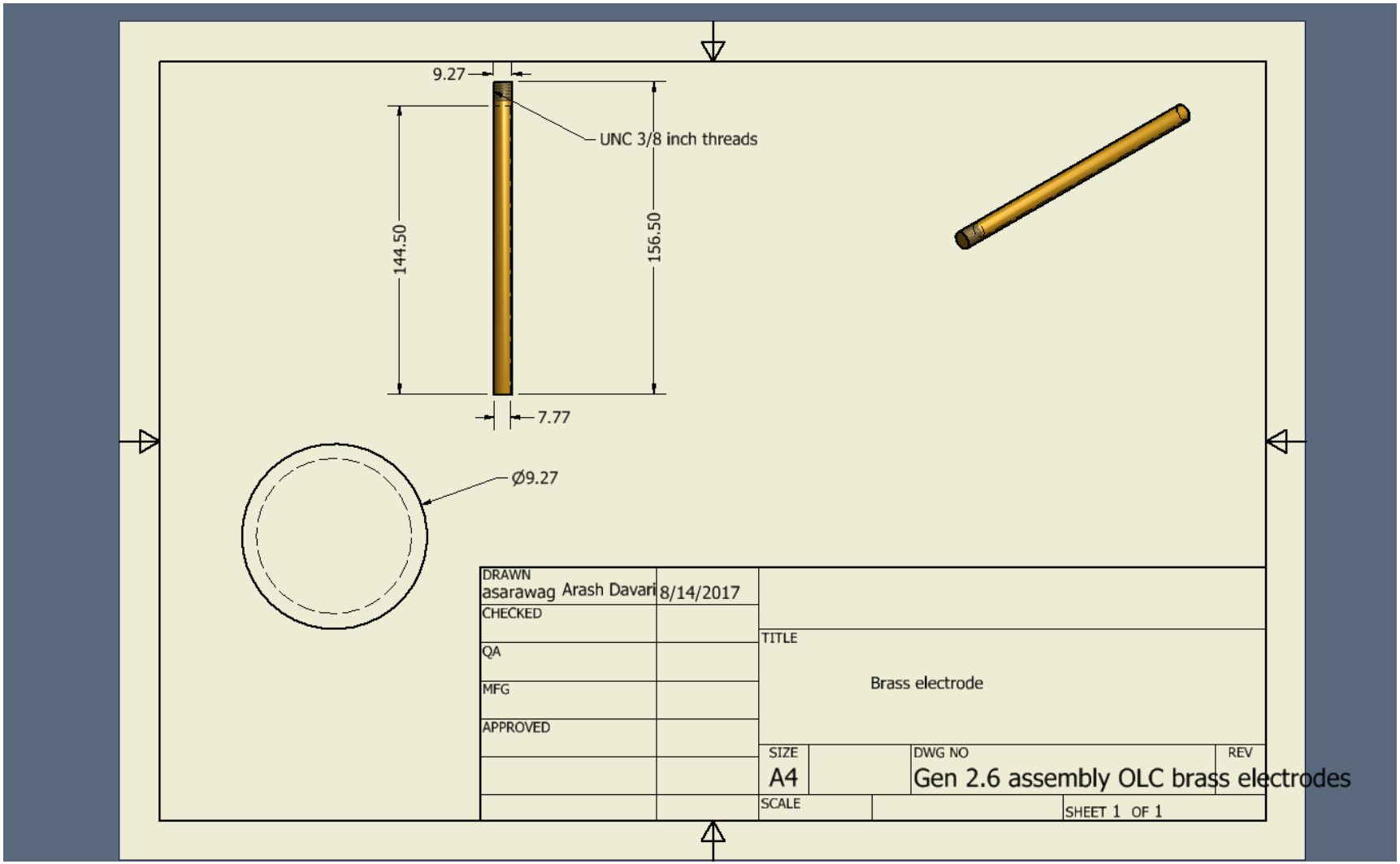
9.27
UNC 3/8 inch threads
144.50
156.50
7.77
Ø9.27
DRAWN
asarawag Arash Davari 8/14/2017
CHECKED
QA
MFG
APPROVED
TITLE
Brass electrode
SIZE
A4
DWG NO
Gen 2.6 assembly OLC brass electrodes
REV
SCALE
SHEET 1 OF 1

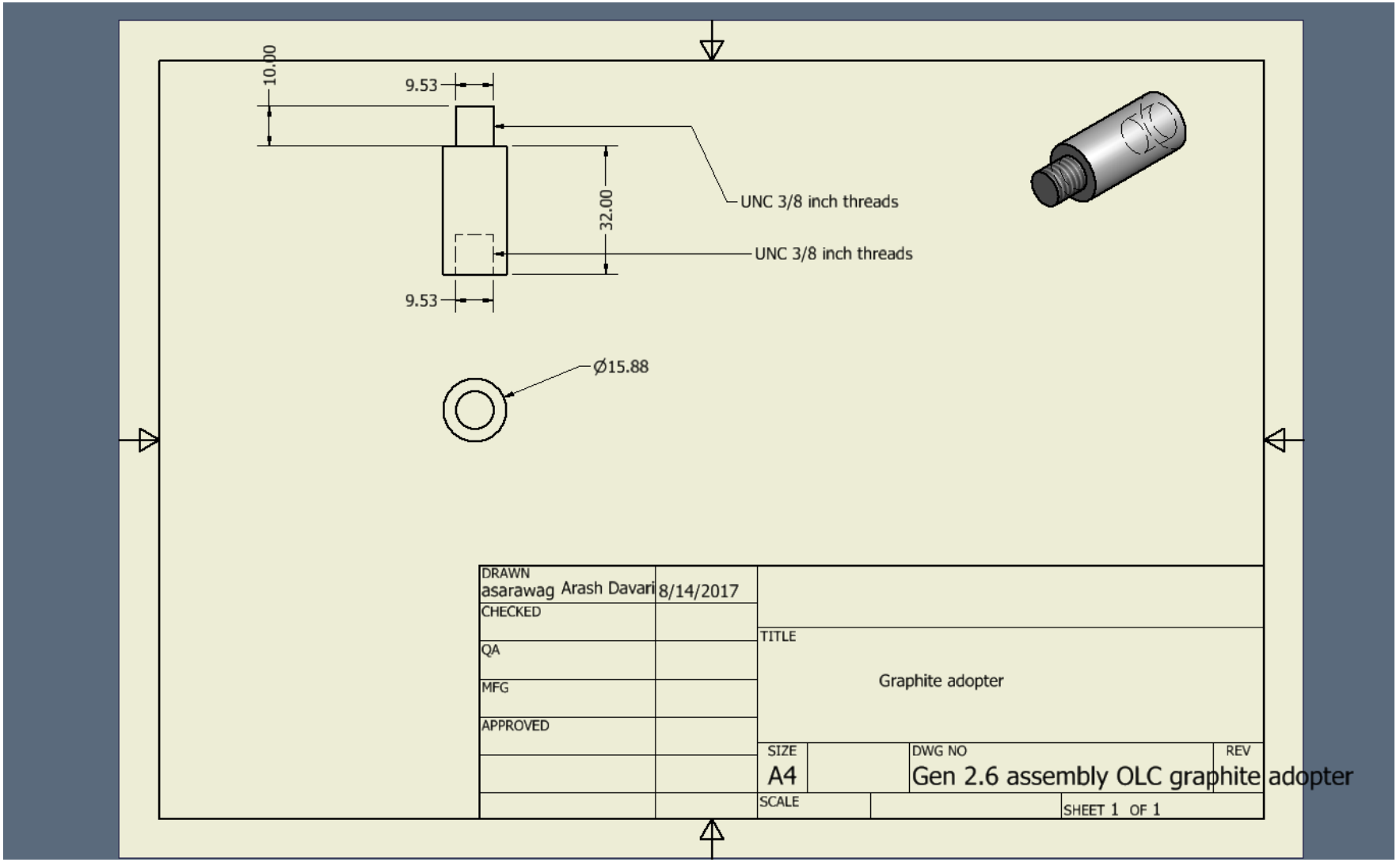
10.00
9.53
32.00
UNC 3/8 inch threads
UNC 3/8 inch threads
9.53
Ø15.88
DRAWN
asarawag Arash Davari 8/14/2017
CHECKED
QA
MFG
APPROVED
TITLE
Graphite adopter
SIZE
A4
DWG NO
Gen 2.6 assembly OLC graphite adopter
REV
SCALE
SHEET 1 OF 1

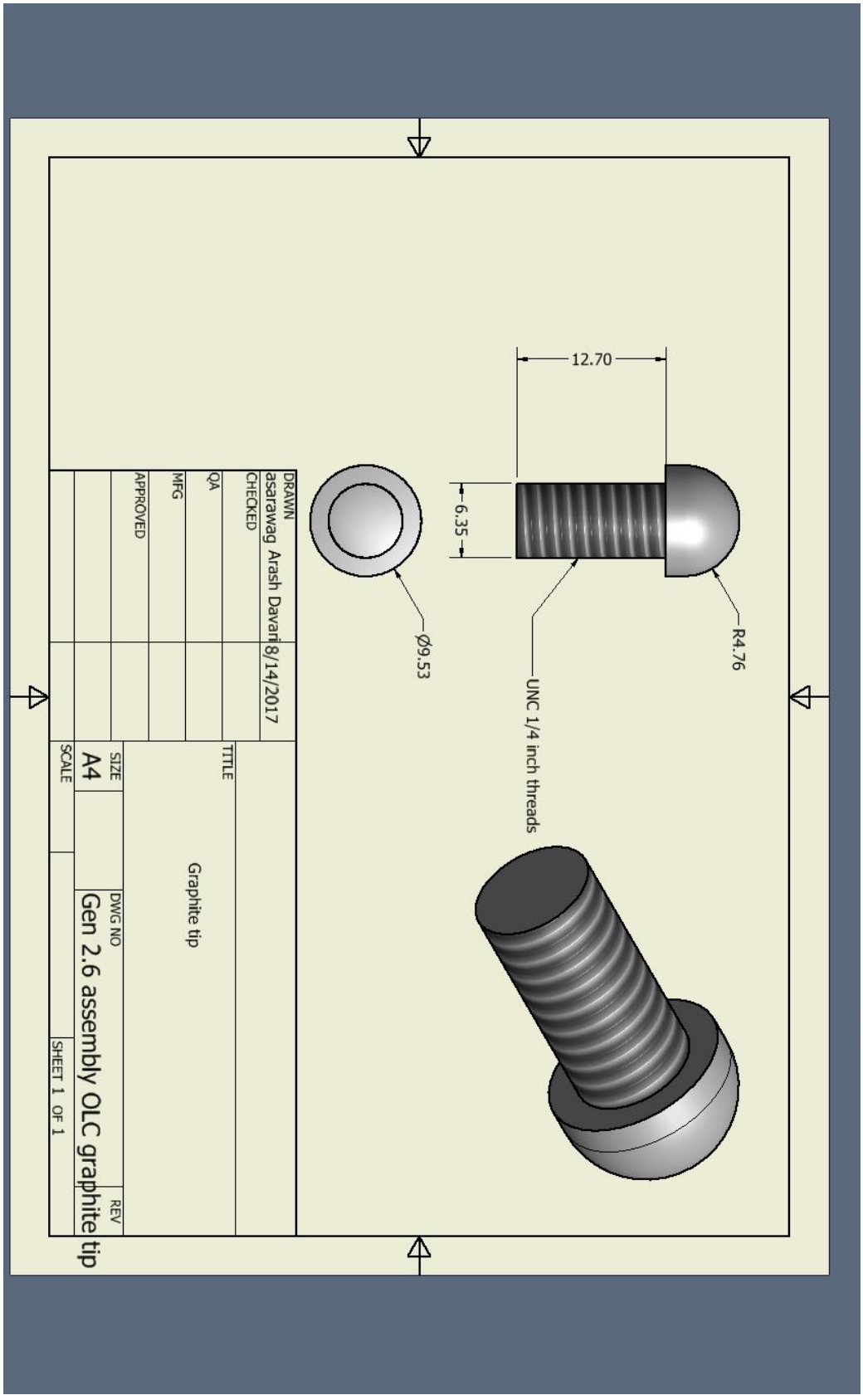
12.70
6.35
Ø9.53
UNC 1/4 inch threads
R4.76
DRAWN
asarawag Arash Davari 8/14/2017
CHECKED
QA
MFG
APPROVED
TITLE
Graphite tip
SIZE
A4
DWG NO
Gen 2.6 assembly OLC graphite tip
REV
SCALE
SHEET 1 OF 1

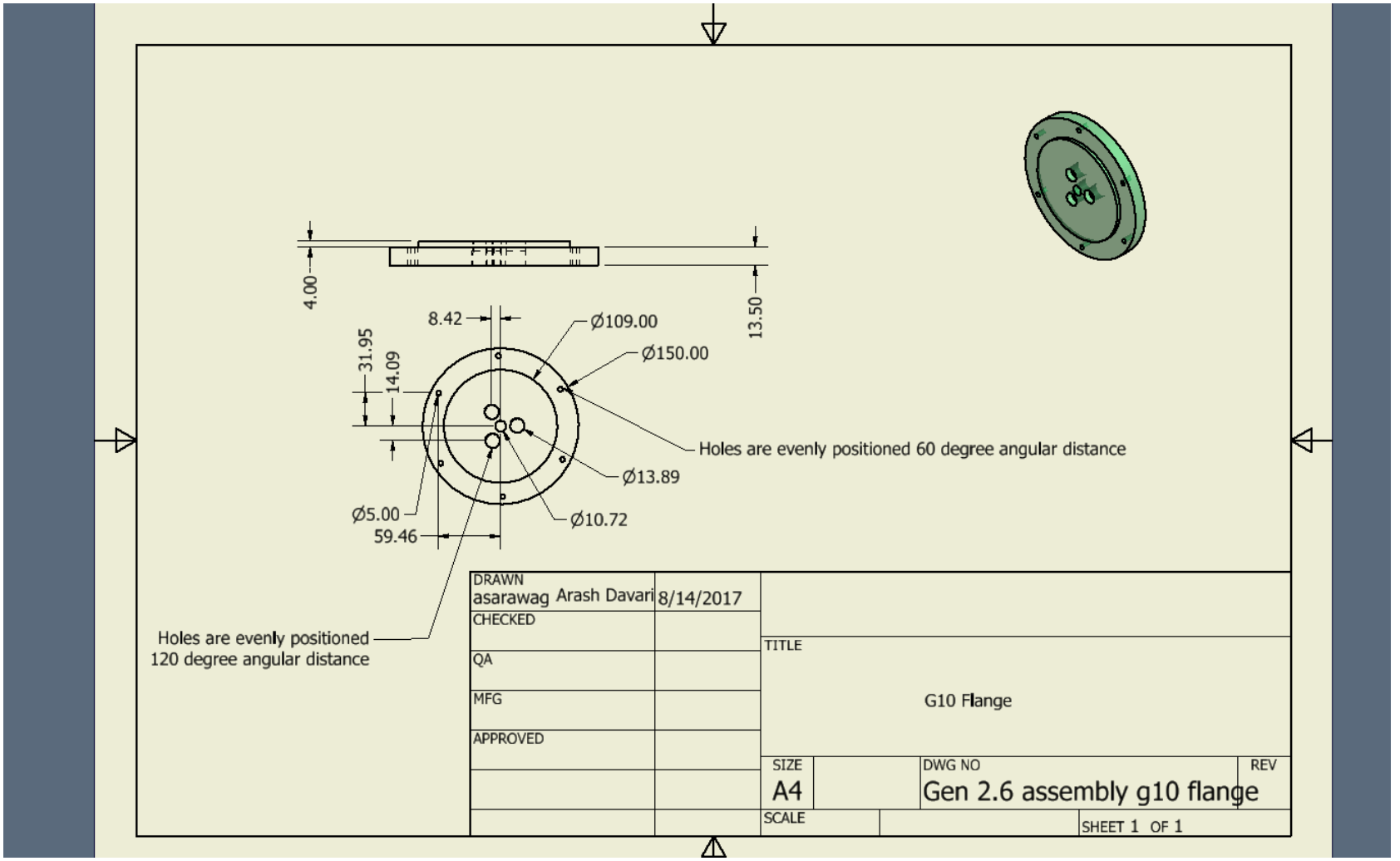
4.00
13.50
8.42
Ø109.00
Ø150.00
31.95
14.09
Holes are evenly positioned 60 degree angular distance
Ø13.89
Ø5.00
Ø10.72
59.46
Holes are evenly positioned
120 degree angular distance
DRAWN
asarawag Arash Davari 8/14/2017
CHECKED
QA
MFG
APPROVED
TITLE
G10 Flange
SIZE
A4
DWG NO
Gen 2.6 assembly g10 flange
REV
SCALE
SHEET 1 OF 1

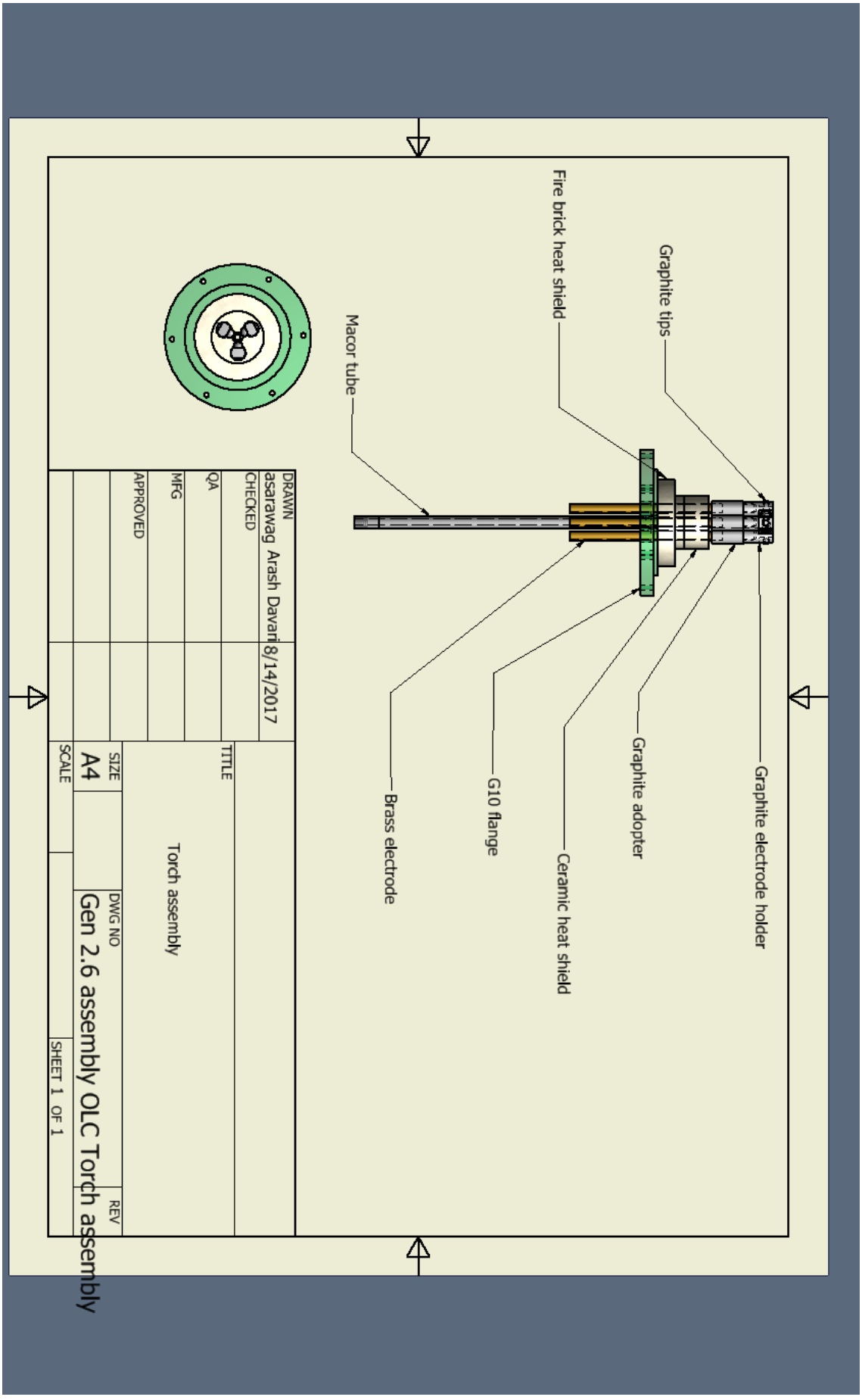
Graphite electrode holder
Graphite adopter
Ceramic heat shield
G10 flange
Brass electrode
Macor tube
Fire brick heat shield
Graphite tips
DRAWN asarawag Arash Davari 8/14/2017
CHECKED
QA
MFG
APPROVED
TITLE
Torch assembly
SIZE A4
DWG NO Gen 2.6 assembly OLC Torch assembly
REV
SCALE
SHEET 1 OF 1

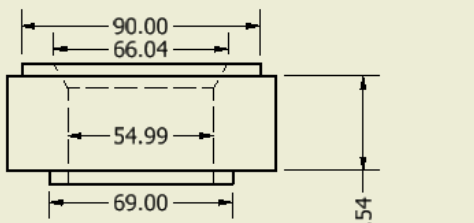

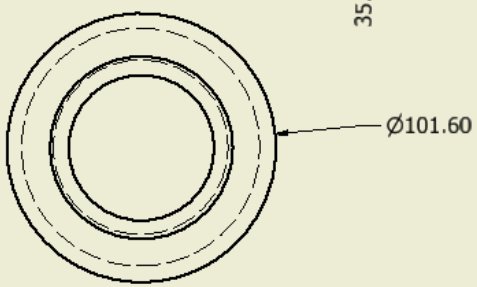

DRAWN asarawag Arash Davari	8/14/2017		
CHECKED		TITLE	Graphite column part 1
QA			
MFG			
APPROVED			
		SIZE A4	DWG NO Gen 2.6 assembly OLC graphite column part 1 REV
		SCALE	SHEET 1 OF 1

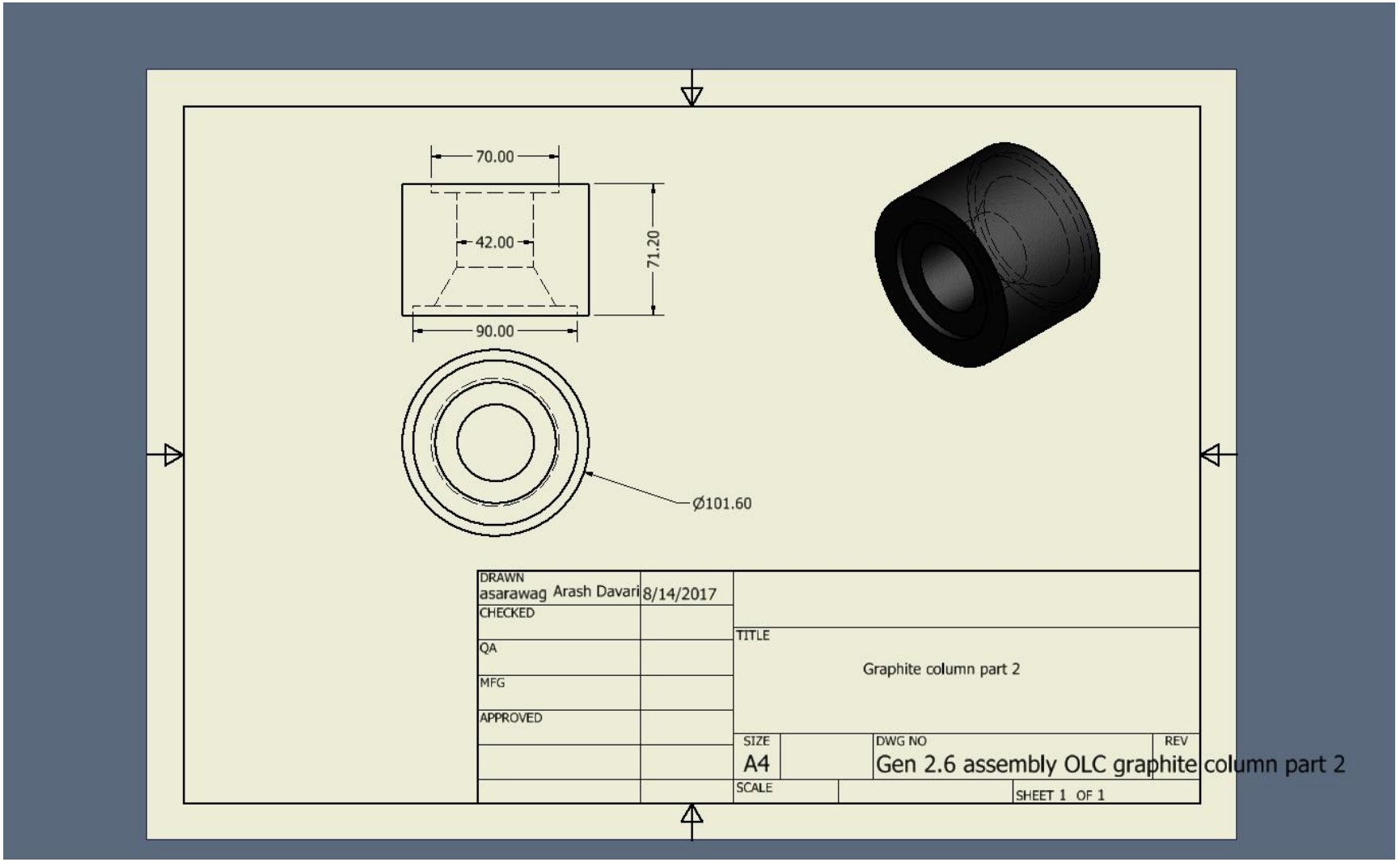
70.00
42.00
71.20
90.00
Ø101.60
DRAWN
asarawag Arash Davari 8/14/2017
CHECKED
QA
MFG
APPROVED
TITLE
Graphite column part 2
SIZE
A4
DWG NO
Gen 2.6 assembly OLC graphite column part 2
REV
SCALE
SHEET 1 OF 1

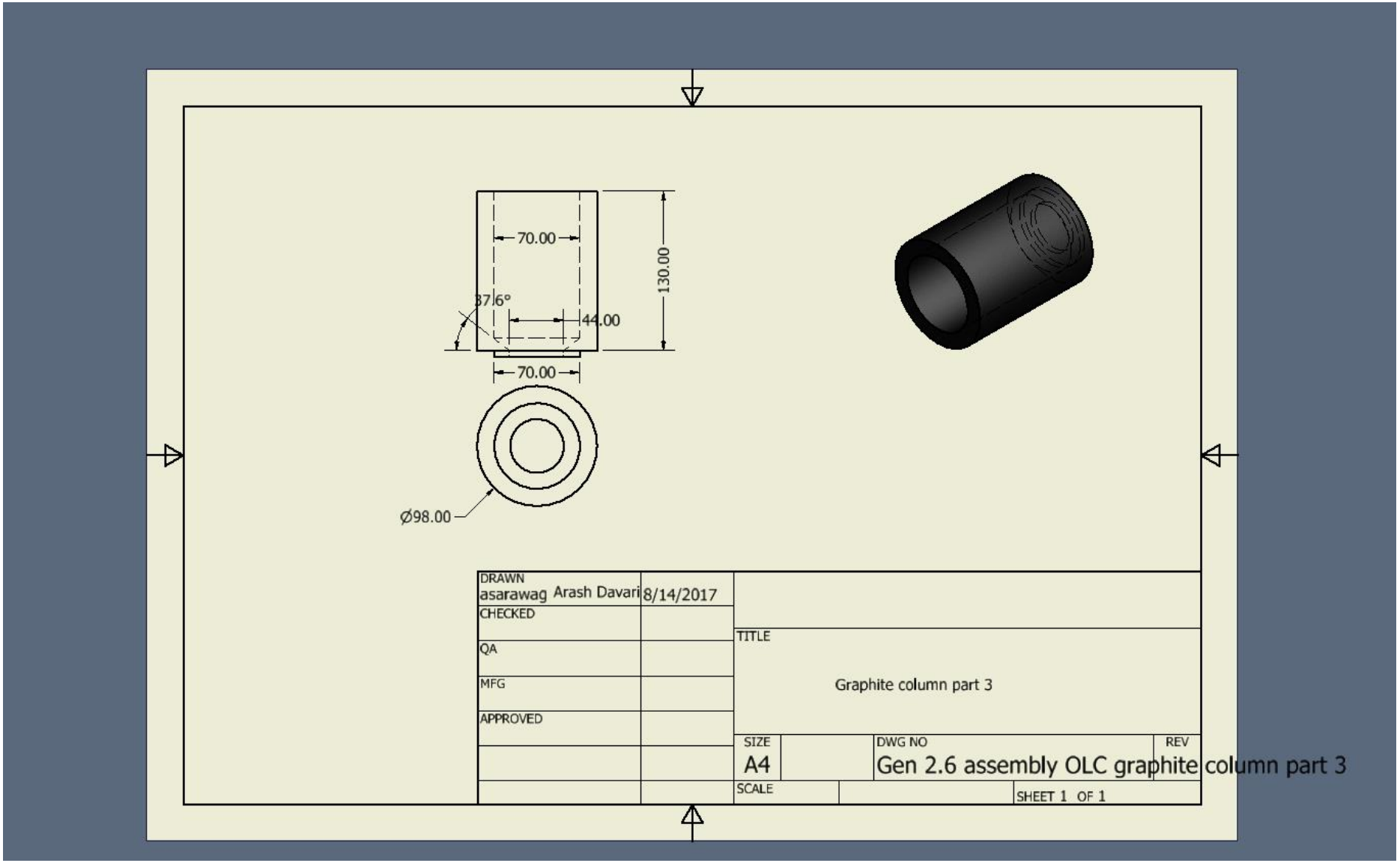
70.00
130.00
37.6°
44.00
70.00
Ø98.00
DRAWN
asarawag Arash Davari
8/14/2017
CHECKED
QA
MFG
APPROVED
TITLE
Graphite column part 3
SIZE
A4
DWG NO
Gen 2.6 assembly OLC graphite column part 3
REV
SCALE
SHEET 1 OF 1

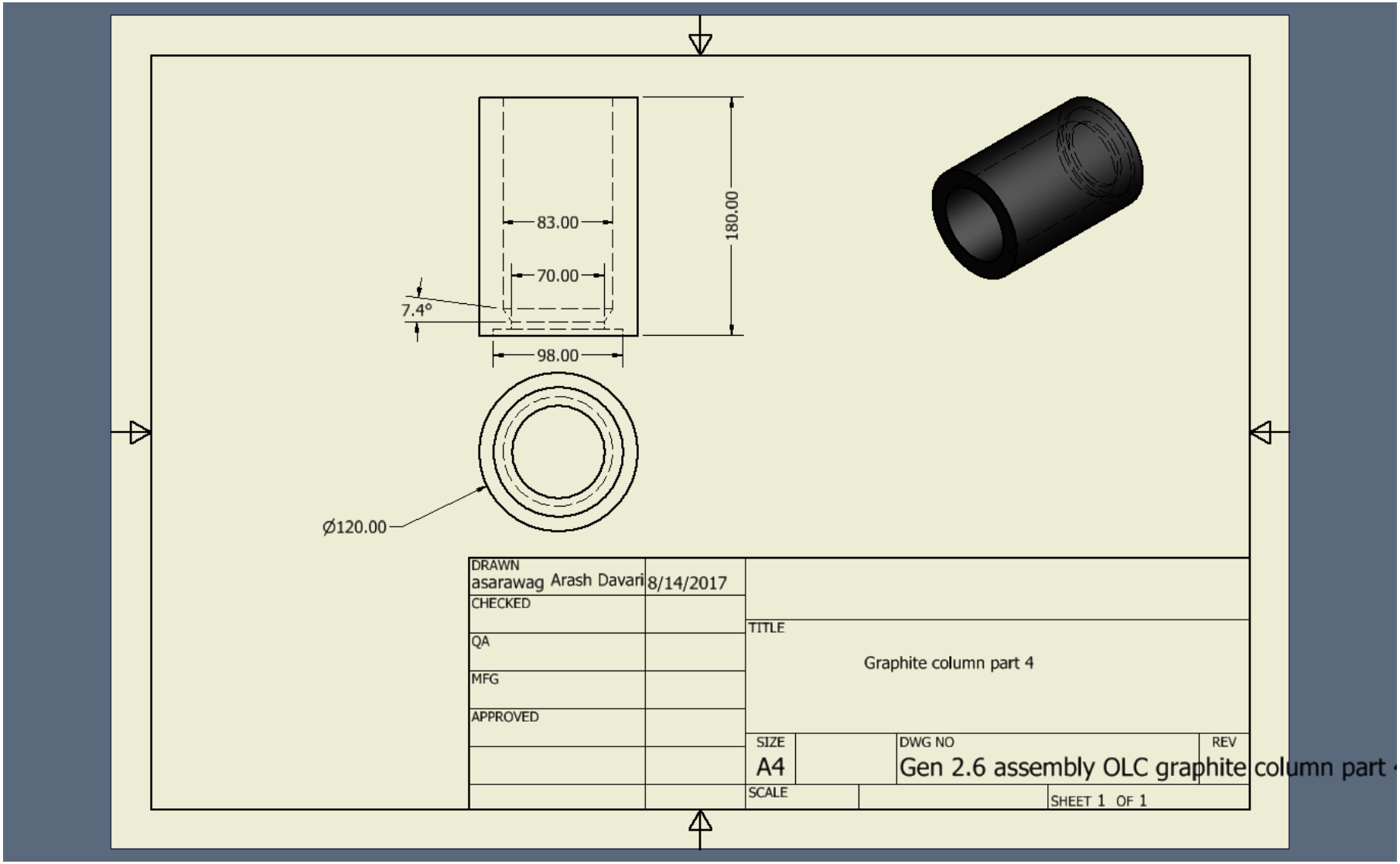
83.00
70.00
7.4°
98.00
180.00
Ø120.00
DRAWN
asarawag Arash Davari
8/14/2017
CHECKED
QA
MFG
APPROVED
TITLE
Graphite column part 4
SIZE
A4
DWG NO
Gen 2.6 assembly OLC graphite column part
REV
SCALE
SHEET 1 OF 1

Ø68.00
127.30
40.00
30.00
8.57
7.50
15.00
DRAWN
asarawag Arash Davari
8/14/2017
CHECKED
QA
MFG
APPROVED
TITLE
Graphite insert
SIZE
DWG NO
REV

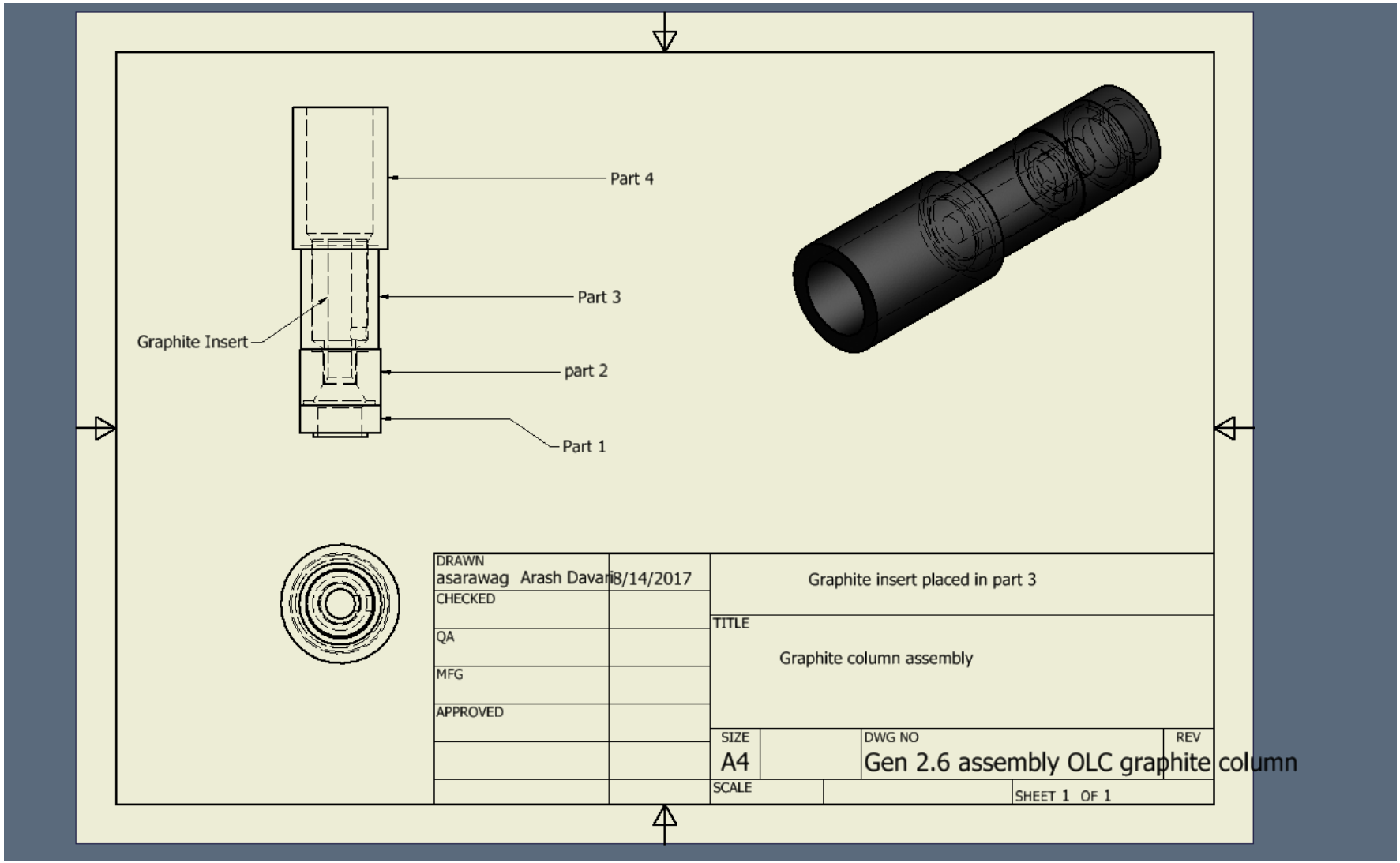
Part 4
Part 3
Graphite Insert
part 2
Part 1
DRAWN
asarawag Arash Davari 8/14/2017
CHECKED
QA
MFG
APPROVED
Graphite insert placed in part 3
TITLE
Graphite column assembly
SIZE
A4
DWG NO
Gen 2.6 assembly OLC graphite column
REV
SCALE
SHEET 1 OF 1

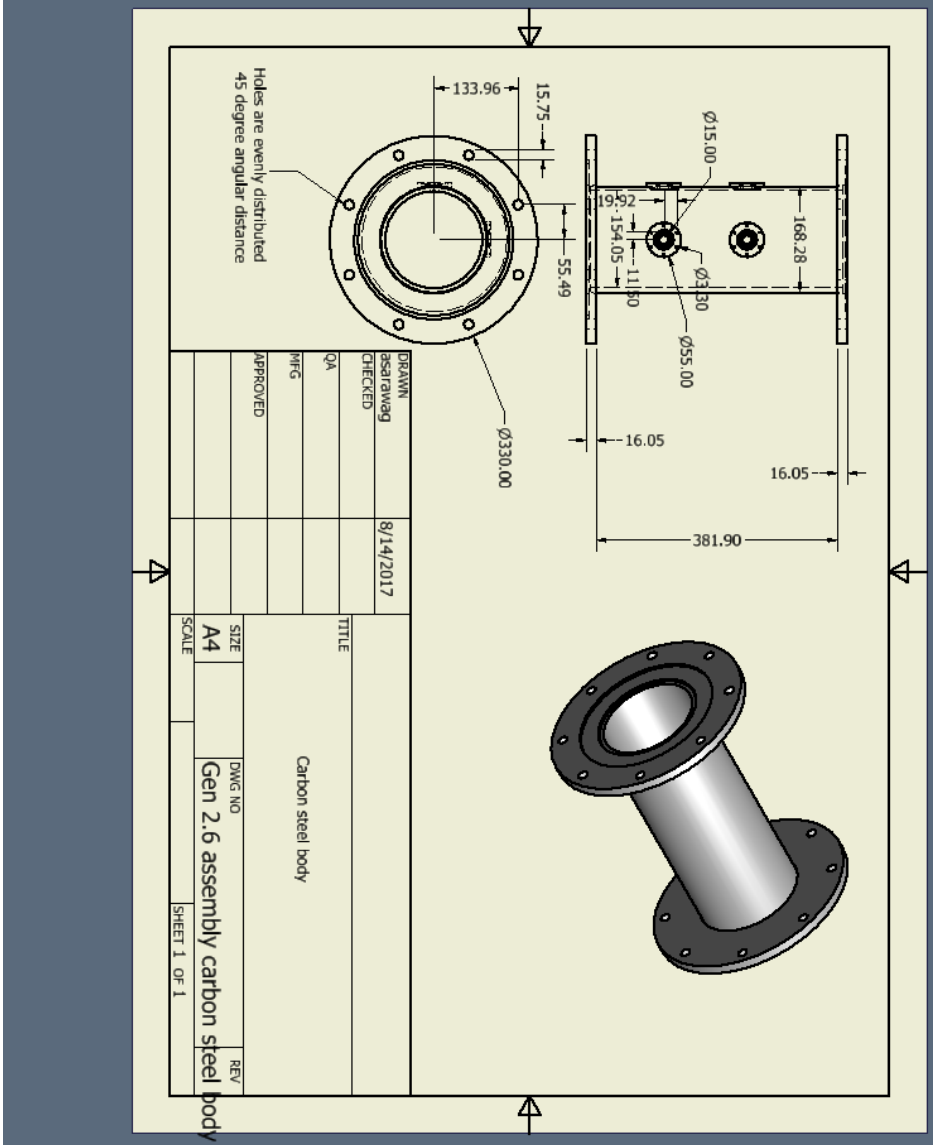
Holes are evenly distributed
45 degree angular distance
133.96
15.75
55.49
Ø330.00
Ø15.00
19.92
154.05
11.50
Ø3.30
Ø55.00
168.28
16.05
16.05
381.90
DRAWN
asarawag
8/14/2017
CHECKED
QA
MFG
APPROVED
TITLE
Carbon steel body
SIZE
A4
DWG NO
Gen 2.6 assembly carbon steel body
REV
SCALE
SHEET 1 OF 1

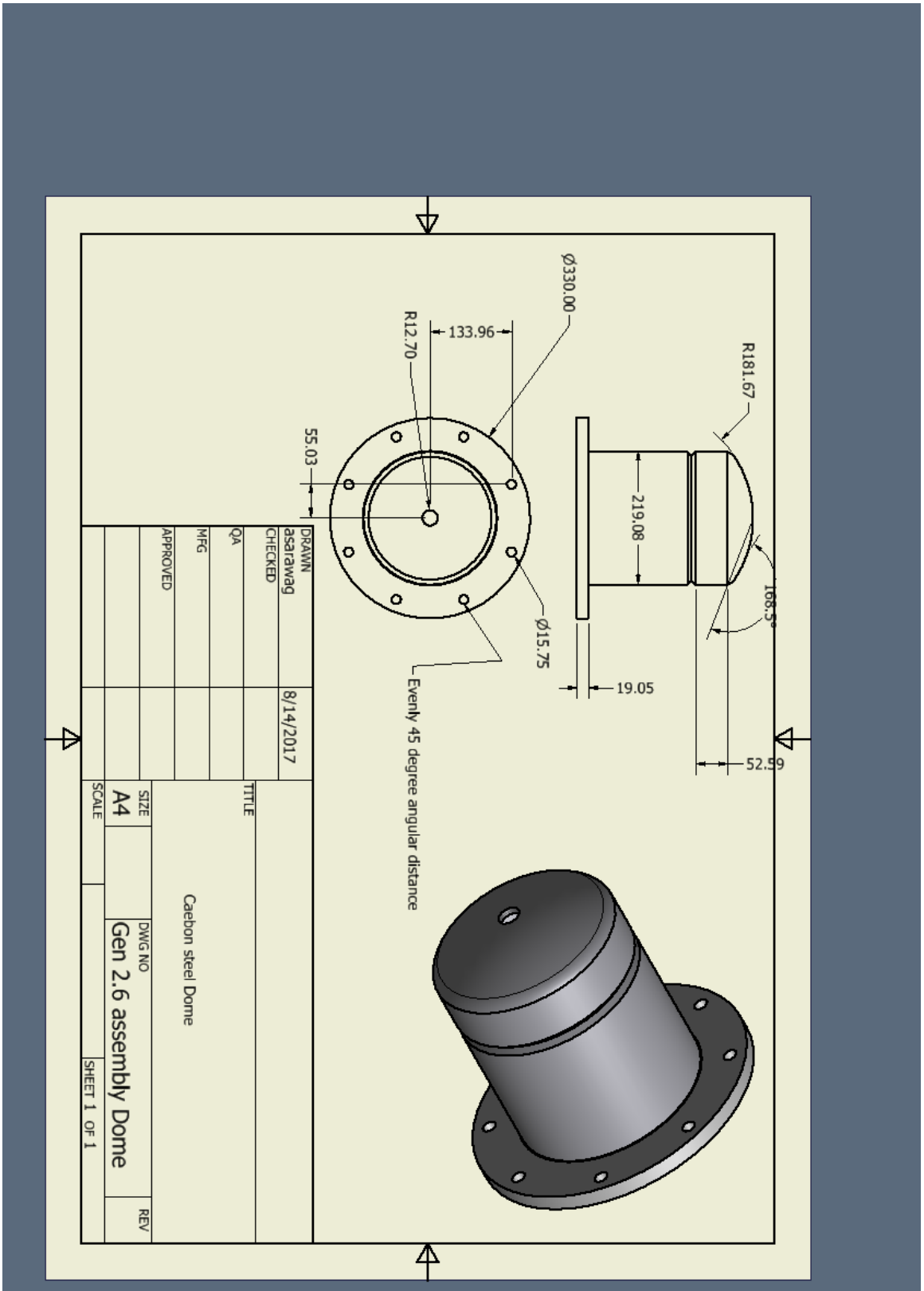
Ø330.00
R12.70
133.96
R181.67
55.03
219.08
168.5°
Ø15.75
19.05
52.59
Evenly 45 degree angular distance
DRAWN asarawag
CHECKED
QA
MFG
APPROVED
8/14/2017
TITLE
Caebon steel Dome
SIZE A4
DWG NO Gen 2.6 assembly Dome
REV
SCALE
SHEET 1 OF 1

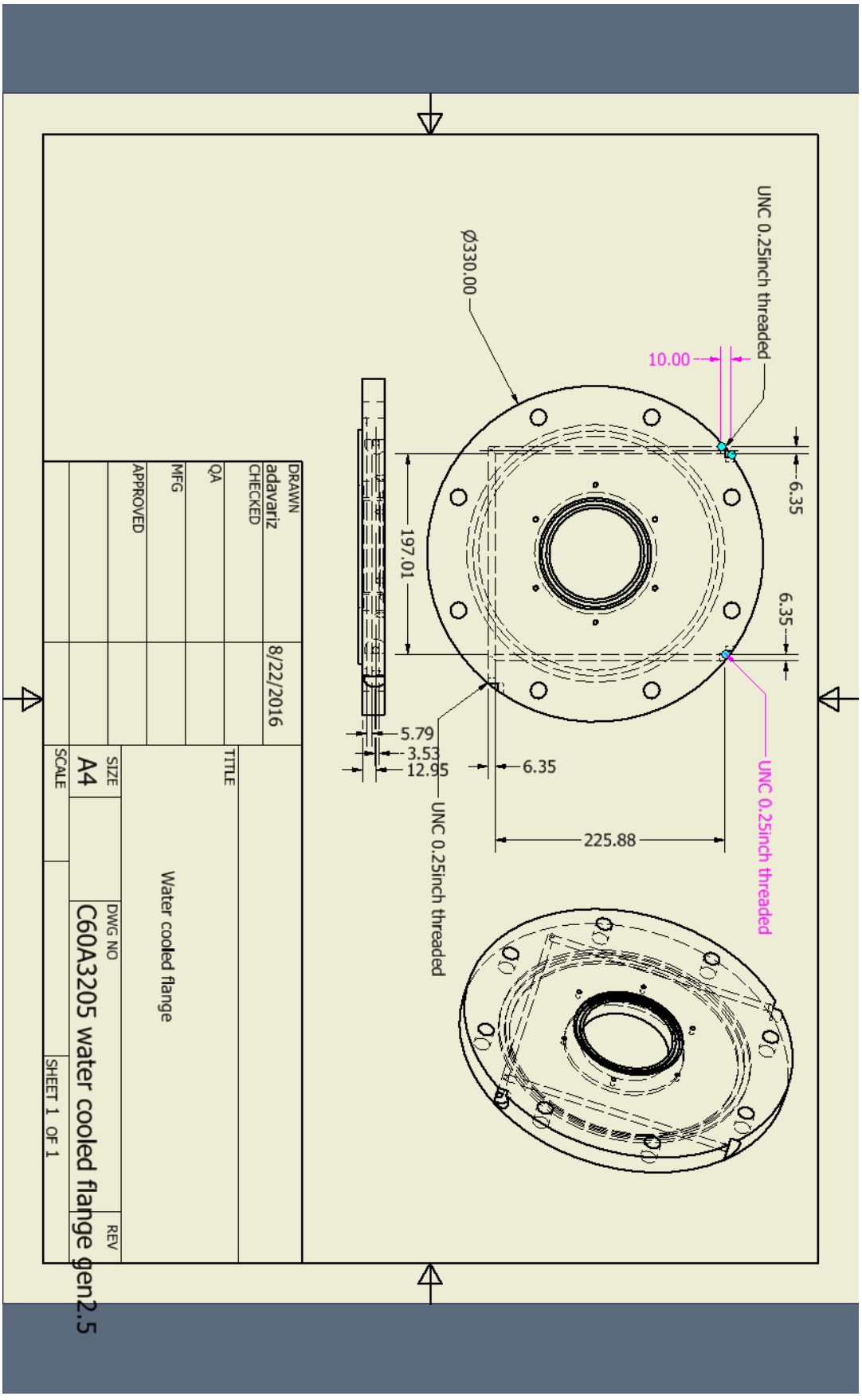
Ø330.00
UNC 0.25inch threaded
10.00
6.35
197.01
6.35
5.79
3.53
12.95
6.35
225.88
UNC 0.25inch threaded
UNC 0.25inch threaded
DRAWN
adavariz
CHECKED
8/22/2016
QA
MFG
APPROVED
SIZE
A4
DWG NO
C60A3205 water cooled flange gen2.5
REV
SCALE
SHEET 1 OF 1
TITLE
Water cooled flange

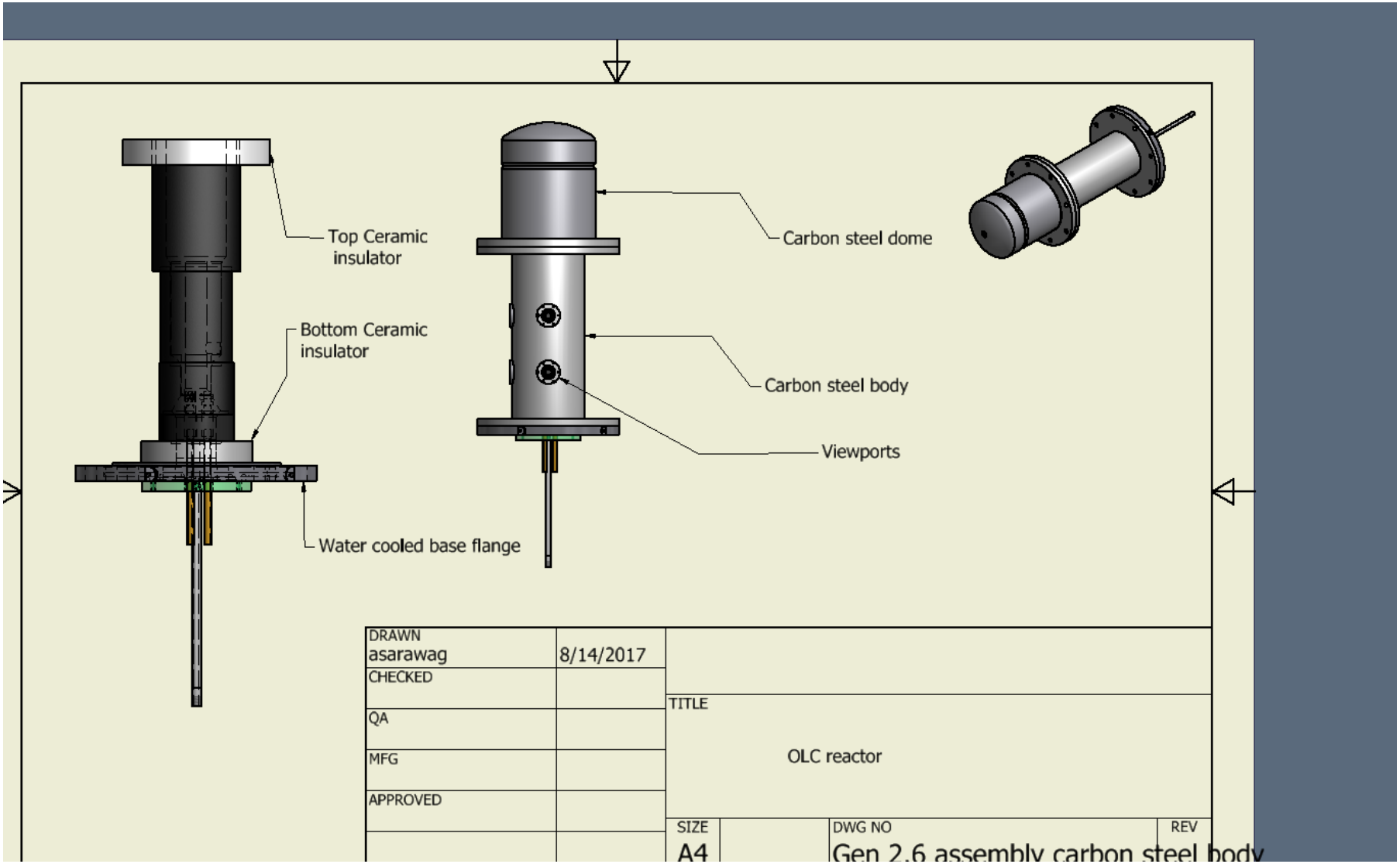
Top Ceramic insulator
Bottom Ceramic insulator
Water cooled base flange
Carbon steel dome
Carbon steel body
Viewports
DRAWN
asarawag
8/14/2017
CHECKED
QA
MFG
APPROVED
TITLE
OLC reactor
SIZE
A4
DWG NO
Gen 2.6 assembly carbon steel body
REV

Curriculum vitae

Arash Davari Zanjani

Islamic Azad University of Takestan, 2009, Bachelor of Science in Mechanical Engineering.

Publication:

Conference Presentation:

Quasi-2D Model Developed for the 3-Phase Plasma Reactor, Mechanical Engineering graduate Students Conference (MEGSC) 2017.

Synthesis of Onion-Like Carbon by 3-phase plasma Reactor, Mechanical Engineering graduate Students Conference (MEGSC) 2016.